TECHNISCHE
UNIVERSITÄT
MÜNCHEN

WALTHER‐MEISSNER‐
INSTITUT FÜR TIEF‐
TEMPERATURFORSCHUNG

BAYERISCHE
AKADEMIE DER
WISSENSCHAFTEN

Magnetization Dynamics and Magnetic Skyrmions in Thin Film Multilayer and Hybrid Systems

Master's Thesis

Misbah Yaqoob

Supervisor: Prof. Dr. Rudolf Gross
Advisor: Prof. Dr. Mathias Weiler
Garching, April 13, 2021

Fakultät für Physik
TECHNISCHE UNIVERSITÄT MÜNCHEN

Contents

Chapter 1

Introduction

Today, we are living in the era of information technology (IT) and our daily lives have been strongly influenced by the digital revolution during the last decades. Since the discovery of the transistor [1], it is possible to process electrical information and the ability to process, store or transport information has been growing rapidly ever since. The miniaturization of the feature size led to the development of integrated circuits with lower costs and higher processing speeds. The miniaturization, nevertheless, is approaching the fundamental physical limits defined by the Heisenberg uncertainty and the atomic nature of matter [2, 3]. Thus, there is immense practical need of new approaches for future information transport, storage and processing.

Lately, the exploitation of the spin degree of freedom of electron has become the focus of diverse research endeavors. In the field of quantum information processing, the behavior and interaction of single spins along with finding ways to use them as a controllable two level systems is investigated [4]. The field of spintronics deals with the investigation of collective spin behavior and spin transport in magnetically ordered materials [5], including chiral spin structures such as magnetic skyrmions [6, 7]. Magnon spintronics exploits the transport of spin angular momentum by collective spin excitations (magnons) and promises potential information processing with low power and without Joule heating [8]. Therefore, spintronics offers prospects for a new generation of devices. One of the examples is the racetrack memory [9] which realizes information storage in the magnetic domains of a ferromagnetic nanowire that can be moved with a spin-polarized current.

Skyrmions are potential candidates for such racetrack type memory applications [10, 11]. Magnetic skyrmions are topologically stabilized swirling spin textures and their appeal for ultra-dense memory and logic devices arises due to their small size, stability and ultra-low current densities needed to move them [12–14]. The dynamics and stabilization of magnetic skyrmions highly depends on their topological properties. In noncentrosymmetric magnetic compounds they can be induced by chiral interactions between atomic spins [15] or in thin films with broken inversion symmetry [16, 17]. Two types of magnetic skyrmions, Bloch-type and Néel-type, correlate with different symmetries of the interaction between spins that give rise to different directions of the rotation of spins. The difference in symmetries can be due to the underlying crystal lattice (Bloch-type) or the presence of an interface (Néel-type). The Néel-type magnetic skyrmions that exist in magnetic thin film multilayers have recently attracted great attention due to their stability at room temperature, low threshold for current-driven motion and the compatibility with existing spintronic technologies [18, 19].

This thesis aims at investigating and tuning magnetization dynamics of purely metallic ferromagnetic thin film multilayers and thin film multilayer hybrid systems at room temperature. Magnetization dynamics can be investigated using numerous measurement techniques which cover the frequency range from GHz to THz. The broadband ferromagnetic resonance (FMR) technique is a well established method which operates in the GHz regime. It has been used for our experiments to study the magnetization dynamics of both systems. The coplanar waveguide used in our FMR measurements operates in a large frequency range. This allows us to extract Gilbert damping parameter α and Landé factor g as well as other spectroscopic parameters. The microfocused frequency-resolved magneto-optic Kerr effect (µFR-MOKE) [20] has also been used to study the magnetization dynamics of patterned devices made from a thin film multilayer hybrid system.

The thesis is organized as follows. In Chapter 2, the theoretical background including Landau-Lifshitz-Gilbert equation, Polder susceptibility and ferromagnetic resonance condition given by the Kittel equation is explained. A brief introduction to skyrmions and spinwaves along with their dynamics is also given. Furthermore, the vector-network-analyzer FMR (VNA-FMR) technique, DC sputter deposition process, electron beam lithography and µFR-MOKE technique (and experimental setup) are presented in this chapter.

In Chapter 3, we first discuss the fabrication of thin film multilayers via DC sputter deposition, the magnetization dynamics of the thin film multilayer system studied by VNA-FMR are then explained. Moreover, a qualitative analysis of the multilayer system with superconducting quantum interference device (SQUID) measurements is also included.

In Chapter 4, the magnetization dynamics of the thin film multilayer hybrid system are investigated using VNA-FMR and µFR-MOKE. The µFR-MOKE technique allows us to investigate the magnetization dynamics in a spatially resolved manner. Furthermore, to understand the static magnetic properties of the hybrid system, we also discuss our corresponding SQUID measurements.

Finally, we summarize the main experimental results in Chapter 5 and give an outlook on future experiments that can now be conducted based on our findings.

Chapter 2

Experimental Techniques and Theoretical Background

This chapter introduces experimental techniques and essential theoretical concepts to explain the obtained results for this thesis. Magnetic ordering arises below a critical temperature even in the absence of an external magnetic field. When the exchange interaction energy overcomes the thermal energy, and depending on the type of interaction, it causes the magnetic moments to arrange in an ordered state [21]. The Heisenberg exchange interaction [22] is responsible for the ordering of ferromagnet and antiferromagnet, where all the magnetic moments are aligned either parallel or anti parallel. In such a magnetically ordered material, the magnetization dynamics can be described as a collective precession of the magnetic moments around the direction of the effective field in the material. The magnetic moments oscillate uniformly in phase with each other and their dynamics are modelled according to a classical, macroscopic approach. This is referred as ferromagnetic resonance (FMR), which will be discussed in more detail in Sec. 2.4. However, there also exist more complicated spin ordering like in a chiral magnet, where along with the Heisenberg exchange interaction the Dzyaloshinskii-Moriya interaction [23] also plays a role, this will be treated in Sec. 2.2. In Sec. 2.5 and Sec. 2.6 we will introduce the fabrication processes sputter-deposition and lithography, which have been used for the fabrication of the thin films/heterostructures and the structuring of our hybrid device. Lastly, in Sec. 2.7 we introduce micro-focused frequency-resolved magneto-optic Kerr effect (FR-MOKE), a novel optical measurement technique [20], to investigate the magnetization dynamics of our hybrid system.

2.1 Spin Dynamics

The collective magnetization of a solid state is the sum over all the magnetic moments $\boldsymbol{\mu}_i$ normalized to the volume V and is thus defined as.

$$\boldsymbol{M} = \frac{1}{V} \sum_{\boldsymbol{\mu}_i \in V} \boldsymbol{\mu}_i.$$

(2.1)

The externally applied magnetic field $\boldsymbol{H}_0$ applies a torque $\boldsymbol{T}$ on the total magnetic moment, $\boldsymbol{\mu} = \boldsymbol{M}V$ which results in a precession of the magnetization around the direction of the

effective magnetic field. The torque is given by

$$\boldsymbol{T} = \boldsymbol{\mu} \times \mu_0 \boldsymbol{H}_{\text{eff}}, \tag{2.2}$$

where $\mu_0 = 4\pi \times 10^{-7}\,\text{V}\,\text{s}/(\text{A}\,\text{m})$ is the vacuum permeability.
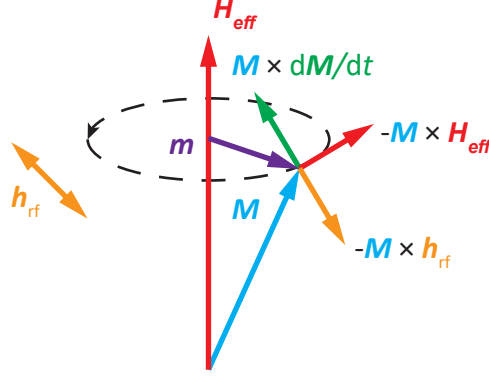
Figure 2.1: Precessional motion of the magnetization $\boldsymbol{M}$ around the effective magnetic field $\boldsymbol{H}_{\text{eff}}$ described by the LLG-equation (2.12). The torque originates from the externally applied magnetic field is indicated in red. The torque created by an additionally applied oscillating field $\boldsymbol{h}_{\text{rf}}$ (yellow), which is perpendicular to $\boldsymbol{H}_{\text{eff}}$, opposes the damping term $\boldsymbol{M} \times \frac{\mathrm{d}\boldsymbol{M}}{\mathrm{d}t}$. This drives the magnetization away from its equilibrium position. Figure adapted from [24].

Since the demagnetization field $\boldsymbol{H}_{\text{de}}$ also takes a non-negligible macroscopic value, the magnetization vector $\boldsymbol{M}$ aligns in equilibrium to the effective magnetic field $\boldsymbol{H}_{\text{eff}}$ rather than the external magnetic field $\boldsymbol{H}_0$. The effective field is defined as

$$\boldsymbol{H}_{\text{eff}} = \boldsymbol{H}_0 + \boldsymbol{H}_{\text{de}}, \tag{2.3}$$

where $\boldsymbol{H}_{\text{de}}$ is the demagnetization field. It is given by

$$\boldsymbol{H}_{\text{de}} = -\boldsymbol{M}\boldsymbol{N}, \tag{2.4}$$

with the demagnetization tensor $\boldsymbol{N}$

$$\boldsymbol{N} = \begin{pmatrix} N_{xx} & N_{xy} & N_{xz} \\ N_{yx} & N_{yy} & N_{yz} \\ N_{zx} & N_{zy} & N_{zz} \end{pmatrix}. \tag{2.5}$$

For an arbitrary sample shape, the demagnetizing fields are spatially non-uniform. However, for ellipsoidal samples uniform demagnetization fields arise and we additionally neglect off-diagonal elements of $\boldsymbol{N}$ and impose the constraint

$$N_{xx} + N_{yy} + N_{zz} = 1 \tag{2.6}$$

Besides the externally applied magnetic field, the effective magnetic field contains any

anisotropy contributions, e.g., interfacial anisotropies, crystalline magnetic anisotropies and magneto-elastic anisotropy [25]. Nevertheless, in our computation we do not consider any anisotropy contribution for simplicity. From classical mechanics it is known that the torque equals the time derivative of the angular momentum

$$\boldsymbol{T} = \frac{d\boldsymbol{J}}{dt},$$
(2.7)

where

$$\boldsymbol{J} = -\frac{\boldsymbol{\mu}}{\gamma}$$
(2.8)

and

$$\gamma = \frac{g\,\mu_{\mathrm{B}}}{\hbar}.$$
(2.9)

Here γ is the gyromagnetic ratio with the Landé-factor g, μ_{B} is the Bohr magneton and $\hbar = h/2\pi$ is the reduced Planck constant. Combining Eq.(2.7) and Eq.(2.1) we get the Landau-Lifshitz equation [26]

$$\frac{\mathrm{d}\boldsymbol{M}}{\mathrm{d}t} = -\gamma\,\boldsymbol{M} \times \mu_0\boldsymbol{H}_{\mathrm{eff}},$$
(2.10)

which describes a sustained precession $\boldsymbol{M}$ around $\boldsymbol{H}_{\mathrm{eff}}$ with a precession frequency ω_L, where

$$\omega_L = \gamma\mu_0|\boldsymbol{H}_{\mathrm{eff}}|.$$
(2.11)

So far, none of the losses have been taken into account therefore, the cone angle of the precession remains unchanged. The LL-equation thus also contains a damping term. Here we adopt the notation by T. Gilbert by adding a dimensionless damping parameter α [27], which then results in the so called the Landau-Lifshitz-Gilbert equation
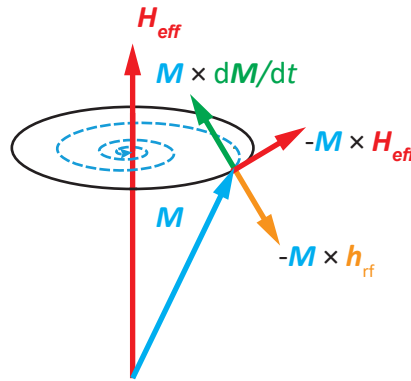
Figure 2.2: Damped precessional motion of the magnetization $\boldsymbol{M}$ around the effective magnetic field $\boldsymbol{H}_{\mathrm{eff}}$. The vector $\boldsymbol{M} \times \frac{\mathrm{d}\boldsymbol{M}}{\mathrm{d}t}$ (green) points towards the center thus, the magnetization relaxes back towards the state of equilibrium over time (blue dashed path).

$$\frac{\mathrm{d}\boldsymbol{M}}{\mathrm{d}t} = -\gamma\,\boldsymbol{M} \times \mu_0\boldsymbol{H}_{\mathrm{eff}} + \frac{\alpha}{M_{\mathrm{s}}}\boldsymbol{M} \times \frac{\mathrm{d}\boldsymbol{M}}{\mathrm{d}t},$$
(2.12)

where $M_{\mathrm{s}} = |\boldsymbol{M}|$ is the the saturation magnetization. The magnetization precesses around

the effective magnetic field $\boldsymbol{H}_{\text{eff}}$ and relaxes back to the state of equilibrium in a spiral trajectory in a finite time, as illustrated in the Fig. 2.2.

2.1.1 Polder-Susceptibility and Kittel-Equation

When we apply an oscillatory field $\boldsymbol{h}_{\text{rf}}$ perpendicular to the static dc magnetic field $\boldsymbol{H}_0$ on a sample with a magnetization $\boldsymbol{M}$, an additional torque $\boldsymbol{M} \times \boldsymbol{h}_{\text{rf}}$ on the magnetization is exerted which consequently counteracts the damping term as depicted in Fig. 2.2. In this case the effective magnetic field can be given by,

$$\boldsymbol{H}_{\text{eff}} = \boldsymbol{H}_0 + \boldsymbol{H}_{\text{de}} + \boldsymbol{h}_{\text{rf}}. \tag{2.13}$$

When the resonance condition is met, the system absorbs the maximum power. In Fig. 2.3 (a) the typical Lorentzian lineshape of the absorption of the system χ'' has been shown. The minimum indicates where the most power is absorbed. Here the applied magnetic
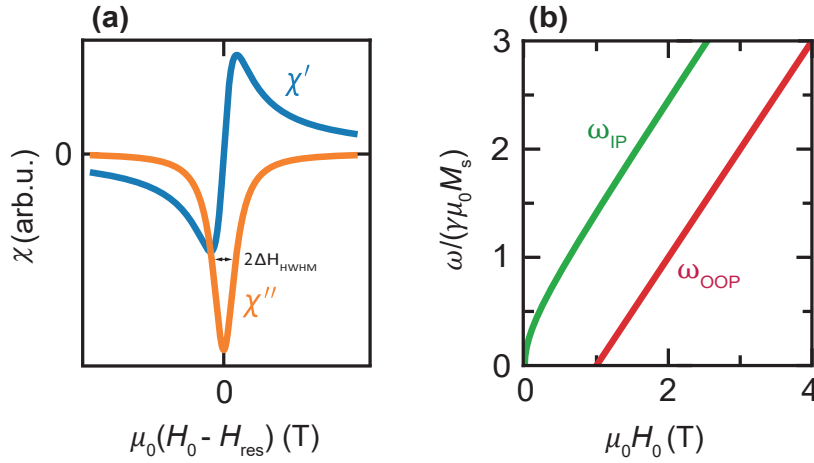
Figure 2.3: (a) The real χ' and imaginary χ'' part of the Polder susceptibility as a function of the externally applied magnetic field $\mu_0 H_0$. The χ' and χ'' describes the dissipation and absorption respectively of the system. The χ'' has a linewidth $2\Delta H_{\text{HWHM}}$ as shown in the figure. (b) Resonance frequencies calculated from Kittel equation as a function of the external magnetic field $\mu_0 H_0$ for the out-of-plane ($N_z = 1$) and in-plane ($N_x = 1$) configuration. Figure adapted from [28].

field is along the z-axis i.e., $\boldsymbol{H}_0 = H_0 \hat{\boldsymbol{e}}_z$. We have a finite size sample and an oscillating magnetic field $\boldsymbol{h}_{\text{rf}}(t) = (h_{\text{rf,x}}(t), h_{\text{rf,y}}(t), 0)$ perpendicular to it. The effective field and the magnetization can be written as,

$$\begin{aligned}
\boldsymbol{H}_{\text{eff}} &= \boldsymbol{H}_0 - N_z M_{\text{s}} \, \hat{\boldsymbol{e}}_z + \boldsymbol{h}_{\text{rf}}(t) \\
\boldsymbol{M} &= M_{\text{s}} \hat{\boldsymbol{e}}_z + M_{\text{s}} \boldsymbol{m}(t),
\end{aligned} \tag{2.14}$$

where $\boldsymbol{m}$ is the dynamic magnetization. We consider $\boldsymbol{H}_{\text{eff}} \parallel \boldsymbol{z}$ and take the dynamic magnetization as $\boldsymbol{m} = \boldsymbol{M}/M_{\text{s}} = \{m_x(t), m_y(t), 1\}$. We furthermore assume that deviations

from the equilibrium orientation are small so that, $m_x, m_y \ll m_z$. Since the alternating parts are assumed to be harmonic, we can write them as,

$$\boldsymbol{h}_{\mathrm{rf}}(t) = \boldsymbol{h}_{\mathrm{rf}} \cdot e^{i\omega t}$$
$$\boldsymbol{m}(t) = \boldsymbol{m} \cdot e^{i\omega t}. \tag{2.15}$$

We describe only the time independent phase and amplitude relations of $\boldsymbol{m}$ and $\boldsymbol{h}_{\mathrm{rf}}$ because they oscillate at the same frequency. Now inserting Eq. (2.13) and Eq. (2.15) into Eq. (2.12) and dealing with dynamics only in the x, y-plane results in

$$\begin{pmatrix} h_{\mathrm{x}} \\ h_{\mathrm{y}} \end{pmatrix} = \chi^{-1} \begin{pmatrix} m_{\mathrm{x}} \\ m_{\mathrm{y}} \end{pmatrix}, \tag{2.16}$$

with

$$\chi = \frac{M_{\mathrm{s}}}{\det(\chi^{-1})} \begin{pmatrix} H_0 + M_{\mathrm{s}} \cdot (N_{yy} - N_{zz}) + \frac{i\alpha\omega}{\mu_0\gamma} & \frac{i\omega}{\mu_0\gamma} \\ -\frac{i\omega}{\mu_0\gamma} & H_0 + M_{\mathrm{s}} \cdot (N_{xx} - N_{zz}) + \frac{i\alpha\omega}{\mu_0\gamma} \end{pmatrix}, \tag{2.17}$$

where χ is the the unitless Polder susceptibility [29]. It gives the response of the magnetization to a small driving field $\boldsymbol{m}M_{\mathrm{s}} = \chi\boldsymbol{h}_{\mathrm{rf}}$, perpendicular to its equilibrium position. We now need to find the resonance condition in a given static magnetic field and we consider that χ attains its maximized absolute value on resonance. In reality, if there is no damping, then χ has to diverge for FMR conditions. Therefore, we solve $\det(\chi^{-1}) = 0$ for the frequency $\omega = 2\pi f$ and take the real part of the solution. We then get the renowned Kittel equation [30],

$$\omega_{\mathrm{res}} = \gamma\mu_0 \sqrt{(H_0 + M_{\mathrm{s}} \cdot (N_{xx} - N_{zz})) \cdot (H_0 + M_{\mathrm{s}} \cdot (N_{yy} - N_{zz}))}. \tag{2.18}$$

We can deduce two special cases of Eq. (2.18) for thin film samples (thickness $\sim$nm). The in-plane (IP) and out-of-plane (OOP) configurations are discussed in detail in Sec. 3.3.1. For a thin film which is magnetized out-of-plane (OOP) the demagnetization terms are $N_x = N_y = 0$ and $N_z = 1$ and Eq. (2.18) becomes

$$\omega_{\mathrm{OOP}} = \gamma\mu_0(H_0 - M_{\mathrm{s}}). \tag{2.19}$$

For the in-plane (IP) configuration, the demagnetization factors are $N_x = 1$ and $N_y = N_z = 0$, thus the in-plane Kittel-equation takes the form

$$\omega_{\mathrm{IP}} = \gamma\mu_0 \sqrt{H_0 \cdot (H_0 + M_{\mathrm{s}})}. \tag{2.20}$$

In Eq.(2.17), the imaginary part in the diagonal elements contain the Gilbert damping parameter α. By solving the equation $\det(\chi^{-1}) = 0$ for the magnetic field H_0 and taking the

imaginary part of the solution, we get the half-width-at-half-maximum (HWHM) linewidth

$$\Delta H_{\text{HWHM}} = \frac{\alpha\omega}{\mu_0\gamma}. \tag{2.21}$$

This equation phenomenologically accounts for all viscous and thus linear-in-frequency contributions to the linewidth. In our experiments we extract the full-width-at-half-maximum (FWHM) linewidth by fitting our FMR curve. Therefore, we need to amend the Eq. (2.21) by multiplying with a factor of 2. Moreover, Eq.(2.21) is often not sufficient to model the experimental data because of frequency-independent contributions to the linewidth due to inhomogeneities. Consequently, an offset is added to Eq. (2.21). Finally, the linewidth can thus be described by

$$\Delta H_{\text{FWHM}} = \Delta H_{\text{inh}} + 2 \cdot \frac{\alpha\omega}{\gamma\mu_0}, \tag{2.22}$$

where ΔH_{inh} is called inhomogeneous broadening. Different factors like inhomogeneities of the external magnetic field, inhomogeneities in the sample or two-magnon scattering processes can contribute to the ΔH_{inh} [31]. ΔH_{inh} can be interpreted as a measure for sample quality.

2.2 Skyrmions and Skyrmion Dynamics

Magnetic skyrmions, named after the nuclear physicist Tony Skyrme, are small swirling topological defects in the magnetization texture [13] as schematically depicted in Fig. 2.4 (a) and (b). In comparison with magnetic vortices or bubbles, skyrmions are relatively stable structures and arise as a result of the interplay of various interactions including exchange, dipolar, Dzyaloshinskii–Moriya interaction (DMI) and anisotropy energy [32].

The DMI interaction can results in a variety of chiral magnetization configurations, including helical, conical, and skyrmionic [33]. These interactions are induced at the interface of magnetic films or because of the lack of inversion symmetry in lattices. The DMI between two atomic spins $\mathbf{S}_1$ and $\mathbf{S}_2$ is expressed as:

$$\boldsymbol{H}_{\text{DMI}} = -\mathbf{D}_{12} \cdot (\mathbf{S}_1 \times \mathbf{S}_2), \tag{2.23}$$

where $\mathbf{D}_{12}$ is the DMI vector between spins $\mathbf{S}_1$ and $\mathbf{S}_2$. Since the magnetic thin films are the main focus of this thesis, we will talk mainly about interfacial Dzyaloshinskii–Moriya interaction (i-DMI). The i-DMI for the thin films come into play from 3-site indirect exchange interaction between two atomic spins $\mathbf{S}_1$ and $\mathbf{S}_2$ and a neighbouring atom with a large spin orbit coupling (SOC) as shown in Fig. 2.4 (c).

Fig. 2.4 shows Néel (a) and Bloch (b) skyrmions. Bloch skyrmions are predominantly found in bulk materials while Néel skyrmions having radial chirality (inward or outward) are typically formed as a result of i-DMI of multilayers. In magnetic thin films having i-DMI, the Dzyaloshinskii–Moriya vector lies in the plane of the film [14]. The i-DMI has a
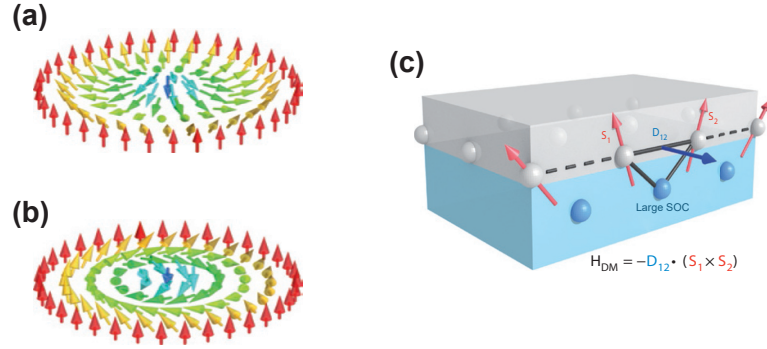
Figure 2.4: (**a**),(**b**) Skyrmions in a 2D ferromagnet. The magnetization is pointing down in the centre and pointing up on the corners. (**a**) The Néel skyrmion where the magnetization rotates by 360° around an axis perpendicular to the diameter. (**b**) The Bloch skyrmion where the magnetization rotates by 360° around the diameter. (**c**) The DMI at the interface between a metal (bottom layer) with a strong SOC and a ferromagnetic metal (top layer). The DMI vector $\mathbf{D}_{12}$ is perpendicular to the plane of the triangle formed between two magnetic sites and an atom with a large SOC. Figure adapted from [13].

global effect on the local magnetization $\boldsymbol{m}$, assuming $\partial\boldsymbol{m}/\partial_z = 0$, it can be expressed by the energy density as

$$\varepsilon_{i-\text{DMI}} = D[m_z \nabla \cdot \boldsymbol{m} - (\boldsymbol{m} \cdot \nabla)m_z], \tag{2.24}$$

where $D = |\mathbf{D}_{12}|$ is the DMI constant. It is negative for clockwise rotations and solely for the i-DMI, it is inversely proportional to the thickness of the film. The expression of the dimensionless DMI field is given by [12]

$$\mathbf{h}_{i-\text{DMI}} = -\frac{1}{\mu_0 M_s{}^2}\frac{\delta\varepsilon_{i-\text{DMI}}}{\partial\boldsymbol{m}} = -\frac{2D}{\mu_0 M_s{}^2}[(\nabla \cdot \boldsymbol{m})\hat{z} - \nabla m_z]. \tag{2.25}$$

The smaller skyrmion size in skyrmion lattices of thin films demonstrates larger values of D/J at interfaces, where J is the exchange constant. From the energy arguments it is clear that, for the existence of skyrmions, the critical value of DMI constant (D_{cr}) depends on both J and the uniaxial anisotropy constant K_{u} i.e., $D_{\text{cr}} \propto (K_{\text{u}}J)^{1/2}$. Therefore, small values of K_{u}/J favors the existence of skyrmions.

2.3 Spinwaves

The LLG Eq. (2.12) shows the precession of the magnetization $\boldsymbol{M}$ with small oscillations around the effective magnetic field $\boldsymbol{M}_{\text{eff}}$. The condition of uniform precession of spins with a spatially constant phase, which we have discussed earlier, is called ferromagnetic resonance. Flipping one of the magnetic moments such that it is anti-parallel to the other magnetic moments results in an energetically unfavorable state with an additional energy. This

leads to distribution of this energy to all magnetic moments and results in a nonuniform precession. These excitations with a finite phase shift between the magnetic moments are called spinwaves [34]. These spinwaves are illustrated in Fig. 2.5. The spinwaves can be considered as a stable wave-like solutions of the LLG equation.
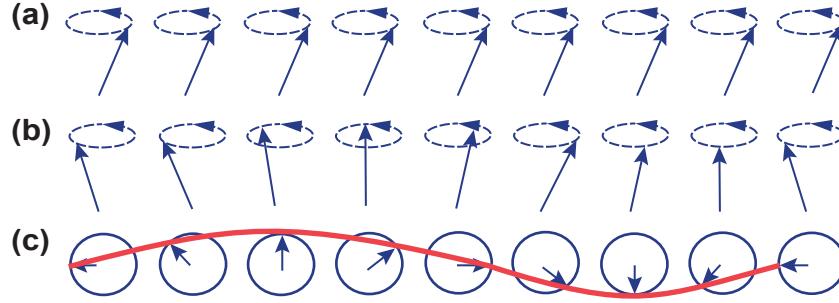
Figure 2.5: (**a**) Uniform precession also known as ferromagnetic resonance (FMR) where all magnetic moments are precessing in-phase. (**b**) A spinwave in a spin chain having wavelength λ and wavevector $\boldsymbol{k}$. The spins viewed in standpoint (**c**) Top view of spins having one wavelength.

For spinwaves, we can define the wavelength λ and corresponding wavevector $|\boldsymbol{k}| = k = 2\pi/\lambda$. The FMR is considered to have a non-propagating spinwave with infinite wavelength $\lambda = \infty$ with $|\boldsymbol{k}| = 0$. Now we want to focus on propagating spinwaves in thin films, where the film thickness d is much smaller than the lateral dimensions of the magnonic waveguide. In this case both, the Heisenberg exchange interaction and the dipolar interaction between the magnetic moments need to be considered. These spinwaves are termed as dipolar-exchange spinwaves. For dipolar or magnetostatic (MSWs) spinwaves, there exist three distinct modes namely, forward volume magnetostatic spinwaves (FVMSWs), backward volume magnetostatic spinwaves (BVMSWs) and magnetostatic surface spinwaves (MSSWs) also known as Damon–Eshbach mode [35]. Depending on the orientation of the applied magnetic field relative to the direction of spinwave propagation, different modes can be excited in thin magnonic waveguides as shown in Fig. 2.6.
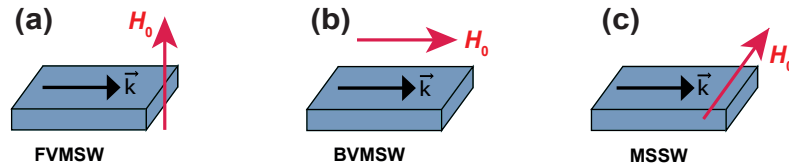
Figure 2.6: (**a**) Forward volume magnetostatic spinwaves (FVMSW), associated with a magnonic waveguide which is magnetized normally to the propagation direction. (**b**) Backward volume magnetostatic spinwaves (BVMSW), associated with propagation direction parallel to the applied magnetic field. (**c**) Magnetostatic surface spinwaves (MSSW) which occur when the applied field is perpendicular to the propagation direction.

We can obtain the resonance frequency for dipolar-exchange spinwaves in the limit $kd \ll 1$, for in-plane magnetized thin films in analogy to the FMR in Sec. 2.1. However, now for the effective magnetic field $\boldsymbol{H}_{\text{eff}}$, in addition to $\boldsymbol{H}_0$, the exchange field $\boldsymbol{H}_{\text{ex}}$ and the dipoler field $\boldsymbol{H}_{\text{d}}$ have to be considered. The following calculations are adapted from Ref. [36].

We can modify Eq. (2.14) using a plane wave ansatz $\exp(i(\omega t - \boldsymbol{k}\boldsymbol{r}))$ for the dynamic components of the magnetization $\boldsymbol{m}(t)$ [37]. Therefore,

$$\boldsymbol{m}(t) = \begin{bmatrix} m_x & m_y & 0 \end{bmatrix}^{\text{T}} \cdot e^{i(\omega t - \boldsymbol{k}\boldsymbol{r})} \tag{2.26}$$

Here an arbitrary space vector $\boldsymbol{r} = x\hat{\boldsymbol{e}}_x + z\hat{\boldsymbol{e}}_z$ and the wavevector $\boldsymbol{k} = k_x\hat{\boldsymbol{e}}_x + k_z\hat{\boldsymbol{e}}_z$ both are restricted to the disk plane. The effective magnetic field $\boldsymbol{H}_{\text{eff}}$ including exchange and dipolar fields takes the form

$$\boldsymbol{H}_{\text{eff}} = \boldsymbol{H}_0 + \boldsymbol{H}_{\text{ex}} + (-H_{\text{dx}}\hat{\boldsymbol{e}}_x - H_{\text{dy}}\hat{\boldsymbol{e}}_y) + \boldsymbol{h}_{\text{rf}}(t), \tag{2.27}$$

where the exchange field $H_{\text{ex}} = \frac{2A}{\mu_0 M_{\text{s}}}k^2$ with the exchange constant A [38]. The dipolar fields H_{dx} and H_{dy} [39] take the form

$$H_{\text{dx}} = M_{\text{s}}\left(1 - \frac{1 - e^{-kd}}{kd}\right)\sin^2\phi,$$

$$H_{\text{dy}} = M_{\text{s}}\frac{1 - e^{-kd}}{kd}. \tag{2.28}$$

Here ϕ is the angle between $\boldsymbol{k}$ and $\boldsymbol{H}_0$. Now using Eq. (2.27) and Eq. (2.12) one could modify the susceptibility which takes the form

$$\chi = \frac{M_{\text{s}}}{\det(\chi^{-1})}\begin{pmatrix} H_0 + H_{\text{ex}} + H_{\text{dx}} + \frac{i\alpha\omega}{\mu_0\gamma} & \frac{i\omega}{\mu_0\gamma} \\ -\frac{i\omega}{\mu_0\gamma} & H_0 + H_{\text{ex}} + H_{\text{dy}} + \frac{i\alpha\omega}{\mu_0\gamma} \end{pmatrix}. \tag{2.29}$$

The corresponding resonance frequency for dipolar-exchange spinwaves can be found by solving $\det(\chi^{-1}) = 0$ for $\omega = 2\pi f$ and taking the real part of the solution. We end up with the Kalinikos-Slavin equation.

$$\omega = \gamma\mu_0\sqrt{(H_0 + H_{\text{ex}} + H_{\text{dx}}) \cdot (H_0 + H_{\text{ex}} + H_{\text{dy}})}. \tag{2.30}$$

There exist two specific limits of Eq. (2.30) :

(**i**) When $k \to 0$ with infinite wavelength: For this case the dipolar fields takes the form $H_{\text{dx}} = M_{\text{s}}$ and $H_{\text{dy}} = 0$ and the exchange field $H_{\text{ex}} = 0$. For this condition, we recover the Kittel equation Eq. (2.20) for the IP configuration.

(**ii**) When k becomes large and spinwaves have short wavelength: In this case $k \gg d$

and the dipolar fields can be neglected i.e., $\frac{1-e^{-kd}}{kd} = 0$. Therefore, the dispersion relation becomes $\omega(k) = \gamma\mu_0(H_0 + H_{ex}) \propto k^2$.

Another important characteristic of spinwaves, which we would like to discuss is their group velocity v_g. The group velocity is given by

$$v_{\mathrm{g}} = \frac{\partial\omega(k)}{\partial k}. \tag{2.31}$$

The Damon-Eshbach mode holds a larger group velocity than the backward volume modes for small k. The lifetime τ and propagation length ξ_{sw} of spinwaves can be calculated with the Kalinikos-Slavin Eq. (2.30). For this calculation, we have to solve $\det(\chi^{-1}) = 0$ for ω and take the imaginary part. We get the spinwave linewidth

$$\Delta\omega = \gamma\mu_0\left(H_0 + H_{\mathrm{ex}} + \frac{H_{\mathrm{dx}}}{2} + \frac{H_{\mathrm{dy}}}{2}\right). \tag{2.32}$$

The inverse of the spinwave linewidth gives the lifetime of spinwave, $\tau = \frac{1}{\Delta\omega}$. When the external excitation field is removed, the amplitude of the spinwave exponentially decays and τ gives the typical timescale of this decay. The propagation length of a spinwave is given by

$$\xi_{\mathrm{sw}} = v_{\mathrm{g}} \cdot \tau. \tag{2.33}$$

The ξ_{sw} defines the characteristic distance of a spinwave propagation before its amplitude decreased to $1/e$ due to the damping.

2.4 Experimental Setup VNA-FMR

The ferromagnetic resonance is used to find the intrinsic parameters of a magnetic material including damping characteristics [40], magnetic anisotropies [41] and the interlayer exchange coupling of a magnetic multilayer [42].

The FMR measurements of this thesis have been done via a vector network analyzer ferromagnetic resonance (VNA-FMR) setup as illustrated in Fig. 2.7. The setup is consist of an electromagnet that can generate a static magnetic field up to 3 T, a vector network analyzer (VNA) and a coplanar waveguide (CPW). The electromagnet consists of an iron yoke and can be rotated by 220°, if needed. The CPW has two ground planes on a dielectric substrate and a metallic thin film patterned into center conductor. The VNA fully characterizes an electrical rf circuit. It produces a wave with frequency f at port 1 and after travelling through the rf circuit, it measures the transmitted wave with the same frequency at port 2. Using microwave cables and two endlaunch connectors, which couple the wave into the center line of the CPW, the port 1 and port 2 are connected to the CPW.

As the ac current passes through the center conductor of the CPW, it induces an elliptical rf magnetic field, $\boldsymbol{h}_{\mathrm{rf}}$, perpendicular to the external static field $\boldsymbol{H}_0$. A sample is placed in a flip-chip style on the CPW and is inductively coupled to it. The CPW is installed according to the required measurements i.e., IP or OOP with respect to the static external
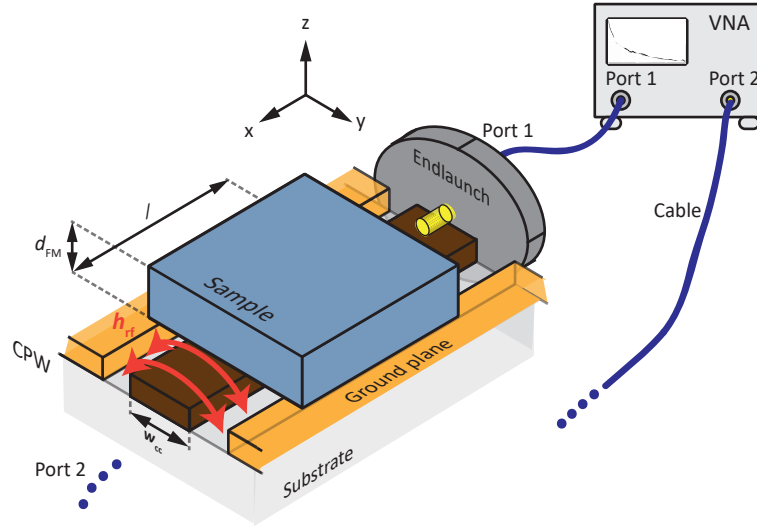
Figure 2.7: Schematic experimental setup of a vector network analyzer for ferromagnetic resonance (VNA-FMR). The VNA is connected to a coplanar waveguide (CPW) via the endlaunch connectors. The sample which is placed faced-down on the CPW is inductively coupled to it. The CPW consists of a center conductor (brown) and two ground planes. The oscillating magnetic field $\boldsymbol{h}_{\mathrm{rf}}$ in the range of microwave frequencies is produced by the VNA at port 1 and received at port 2. Figure taken from [24].

field. On application of the static external magnetic field, the magnetic moments in the sample start precessing around the direction of the external field. The CPW drives the excitation torque on the precessing magnetization with an oscillating magnetic field $\boldsymbol{h}_{\mathrm{rf}}$. It also detects the additional current, which is induced by the precessing magnetization in the sample (due to Faraday's law) into the CPW. In other words, it acts as an excitation as well as a detection transducer. When the applied microwave frequency matches the resonance frequency of the precessing magnetization, the induced current opposes the excitation current and the microwave power is absorbed. When the sample absorbs energy, the FMR resonance condition is fulfilled. Therefore, we are interested in the change of transmission. This change is parameterized by the complex transmission parameter S_{21}, which is defined as the ratio between the incident wave at port 2 and the outgoing wave at port 1

$$S_{21} = \frac{V_2}{V_1} = \frac{|V_2|}{|V_1|}\, e^{i(\phi_2 - \phi_1)}, \tag{2.34}$$

where V_1 and V_2 are the measured voltages, which are complex quantities. These complex voltages have magnitudes $|V_{1,2}|$ and phases $\phi_{1,2}$ at port 1 and 2, respectively. The transmission parameter S_{21} contains the background S_{21}^0, which originates from the frequency-dependent transmission of the setup and change in transmission ΔS_{21} coming from the sample. The ΔS_{21} is given by

$$\Delta S_{21} = \frac{S_{21} - S_{21}^0}{S_{21}^0}. \tag{2.35}$$

2.5 DC Sputter-Deposition

We have used a dc-magnetron-sputtering method using the ultra-high vacuum (UHV) sputtering machine to fabricate the ferromagnet thin film multilayer system. In the sput-
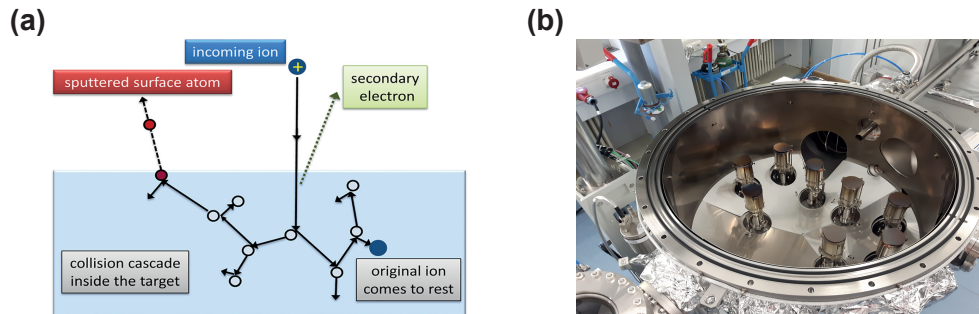
Figure 2.8: (**a**) Schematic illustration of the sputtering process: An energetic ion triggers a collision cascade inside the target and knock off one or more surface atoms. The secondary electrons may also be emitted and play an important role in sustaining the discharge. Figure taken from [43]. (**b**) Inner view of the sputtering chamber. The magnetrons are placed for complex multilayer deposition. Both, face-to-face and confocal sputtering is possible with this setup. Credit: Matthias Althammer.

tering process, the positively charged ions are accelerated by an electric field between a high purity target material cathode, and anode, towards the target material which then cause a collision cascade in the target. After the collisions, the secondary electrons and surface atoms or sometimes small clusters of atoms leave the target. These atoms are then deposited onto a substrate which is positioned above the target [44]. This process has been illustrated in Fig. 2.8 (a).

In the process of magnetron sputtering, magnetic field traps the electrons in a helical motion, which significantly increases their path to the anode. The magnetrons inside a sputtering chamber are shown in Fig. 2.8 (b). In the absence of magnetic field, the secondary electrons are accelerated directly by the electric field towards the positively charged anode. On their way, they collide with gas atoms and create a plasma of ions and further electrons. Whereas, with a magnetic trap, electrons drift in a circular motion and hence undergo more collisions [45]. A low gas pressure during the sputter deposition is needed to prevent the ejected target atoms to scatter with inert gas ions before reaching the sample. In our experiment, we have used Argon gas with a pressure (P) of a few 10^{-3} mbar.

2.6 Micropatterning by Electron Beam Lithography

Lithography is a well established method for structuring in microelectronics [46]. There are countless applications for such patterning in the research and manufacture of electronic, photonic and optical devices. In order to fabricate our hybrid device for FR-MOKE measurements, we have used electron beam lithography method using NanoBeam nB5 setup. In this section, we will briefly discuss the overall electron beam lithography process. The

employed process has been illustrated in Fig. 2.9.
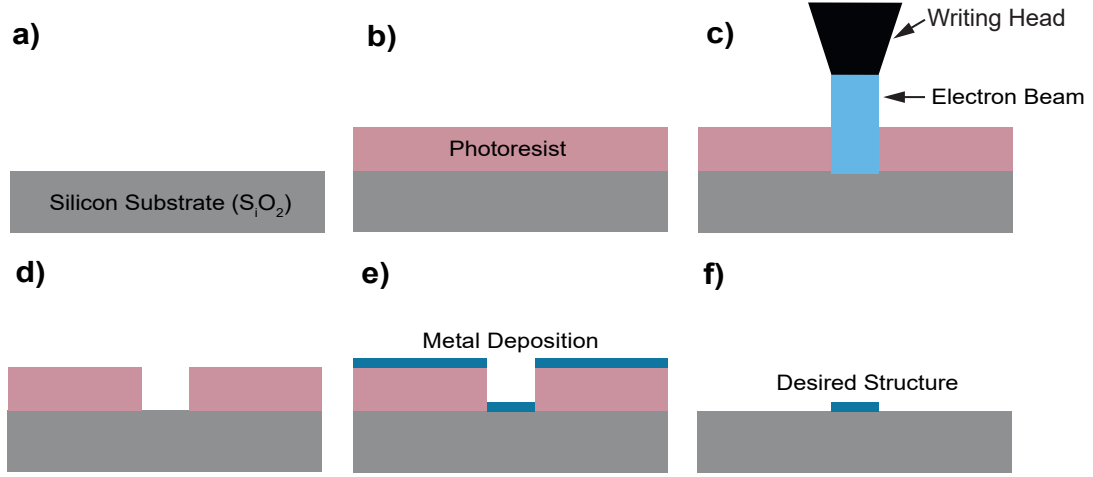
Figure 2.9: The typical production process for structured samples using electron beam lithography. (**a**) Substrate cleaning and pretreatment. (**b**) Application of a photoresist to the cleaned silicon substrate by spin coater and soft baking afterwards (**c**). The resist is exposed to an electron beam for writing the desired pattern. (**d**) Development of the sample. (**e**) Deposition of material. (**f**) lift-off process by dissolving the resist.

The sample was structured on a silicon substrate with a 1 μm thick oxide layer on top. The substrate was cleansed by Acetone followed by Isopropanol in an ultra-sonic bath. The whole pattern of our device was then written step by step (first markers, then magnonic waveguide, then contact pads and at last antenna), using the NanoBeam nB5 setup at WMI and a positive resist (Allresist AR-P617.08). After finishing the writing process, the sample was put into an appropriate developer to dissolve the exposed resist. In our case, we used the developer AR600-56 for 2 minutes and then immersed the sample in Isopropanol for 30 seconds. After development, the desired deposition for different fragments e.g, markers, multilayer thin film, contact pads or antenna is done using dc sputtering technique as discussed earlier in Sec. 2.5. Afterwards, lift-off is performed in warm Acetone ($\sim 70°C$), which dissolves the resist and thus lifts off the metal coating on top. In the end, only material, which is deposited directly onto the substrate is left on the sample.

2.7 Frequency-Resolved Magneto-Optic Kerr Effect

In this section we will introduce the excitation and detection technique of magnetization dynamics of propagating spinwaves. Our detection of spinwaves is based on the magneto-optic Kerr effect (MOKE) [47] which we will discuss in detail in the following section.

2.7.1 Magneto-Optic Kerr Effect

When linearly polarized light interacts with magnetization, it induces a rotation of the polarization plane with a Kerr angle θ_K and ellipticity η_K. The complex rotation of the polarization plane is given by

$$\Phi = \theta_K + i\eta_K, \tag{2.36}$$

where θ_K specifies the rotation of the major axis of the reflected light, and η_K is the ellipticity [36, 48]. There are different configurations of MOKE depending on the orientation of the magnetization $\boldsymbol{M}$ with respect to the plane of the sample e.g., polar MOKE, longitudinal MOKE and transverse MOKE [49]. In our experiment, due to symmetry reasons the longitudinal and transverse MOKE have not been observed so, we had only the polar MOKE.

Now we will move forward towards the detection of magnetization dynamics of the spinwave utilizing the MOKE. When the incident laser light having linear polarization is directed to the ferromagnetic material, the light does not reflect at the interface, instead travels through a certain depth of the material, where the intensity of the laser is attenuated and the phase is delayed. The magnetization $\boldsymbol{M}$ oscillates parallel to the sample plane and the dynamic component of the magnetization $\boldsymbol{m}(t)$ oscillates as a function of time with frequency $\omega_{sw} = 2\pi f_{sw}$. In other words, the dynamic component $\boldsymbol{m}(t)$ oscillates between the out-of-plane and the in-plane direction. The polar MOKE perceives it as either zero, minimal or maximal. The oscillating magnetization ultimately causes the Kerr angle θ_K to be time-dependent therefore, it oscillates at the frequency of the magnetization dynamics and the Kerr angle θ_K takes the form [36, 50]

$$\theta_K(t) = \theta_K \sin(\omega_{sw} t + \phi), \tag{2.37}$$

where ϕ is the phase shift of the incident light .

2.7.2 Excitation and Detection of Spinwaves

In this section, we will discuss how to excite and detect magnetization dynamics of propagating spinwaves. For this purpose, we have used a coplanar waveguide (CPW) antenna on top of the magnonic waveguide which was patterned via lithography technique as discussed in Sec. 2.6. A schematic view of the spin wave excitation and detection is shown in Fig. 2.10. A static magnetic field $\boldsymbol{H}_0$ is applied in plane (IP) with respect to the sample orientation. This static field fixes the direction of the magnetization $\boldsymbol{M}$ within the sample. A microwave source using vector network analyzer generates a microwave having a certain power P_{MW} and frequency f_{MW}. Due to the coupling of this microwave to the patterned antenna, an oscillating magnetic field $\boldsymbol{h}_{rf}$ (by Amperè's law) is generated.

In Fig. 2.10 (b), we can see that the microwave currents I_{rf} have different direction in neighbouring microstrips. In the outer microstrips it is flowing in the same direction whereas, the current in the central stripe is opposing them. Therefore, the oscillating fields generated by each micro-strip add up. The distance of the two outer microstrips defines the periodicity in the rf currents and hence, determines the most efficiently excited wavelength
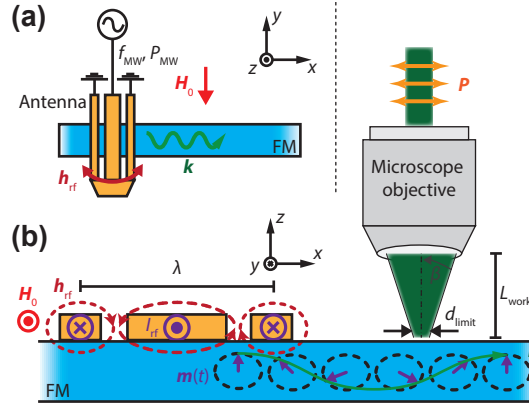
Figure 2.10: Excitation principle of coherent spinwaves. (**a**) Top view of the sample (**b**) Side view of the sample. On application of static magnetic field $\boldsymbol{H}_0$ to the ferromagnet (FM), the direction of the magnetization is fixed. An oscillating magnetic field $\boldsymbol{h}_{\mathrm{rf}}$ is generated by a microwave current I_{rf}, when applied to an on-chip patterned antenna which couples to the the dynamic magnetization $\boldsymbol{m}(t)$. Spinwaves with a certain wavevector $\boldsymbol{k}$ and wavelength λ can be excited depending on the periodicity of the antenna. To spatially resolve the magnetization dynamics, the microscope objective (MO) focuses the polarized laser light at its working distance L_{work} to a diffraction limited spot size with diameter d_{limit}. Figure taken from [36].

$\lambda = 2\pi/k$ of the spinwave. The spinwave is coherently excited at the antenna. For a given static magnetic field $\boldsymbol{H}_0$, the dynamic magnetization $\boldsymbol{m}(t)$ couples to the oscillating driving field $\boldsymbol{h}_{\mathrm{rf}}$ if the microwave frequency f_{MW} matches the spinwave dispersion as discussed in Eq. (2.30). The coherently excited spinwave start propagating away from the antenna. Due to the dipolar and exchange interaction, the phase between the local dynamic magnetization $\boldsymbol{m}(t)$, the excitation field $\boldsymbol{h}_{\mathrm{rf}}$ and consequently the microwave source is retained.

A linearly polarized laser which is focused onto the magnonic waveguide using a microscope objective is used to measure the dynamics of the magnetization. The microscope objective collimates and collects the laser light with a certain angle β. Thus, because of the symmetry, the ellipticity and the Kerr rotation induced by the transverse and longitudinal Kerr effect become zero and we observe only the polar MOKE. After reflection, due to the MOKE, the polarization of the laser light gets rotated and elliptical with the Kerr angle θ_{K}, which oscillates now as a function of time. The backreflected light containing the phase information is collected by the microscope objective and then returned to the optical setup.

2.7.3 Experimental Setup and Working Principle

In our experiment, we have adopted a relatively new technique namely, microfocused frequency-resolved magneto-optic Kerr effect (µFR-MOKE) [20], which is based on the FR-MOKE [20, 51]. It detects the magnetization dynamics in a spatially-resolved manner. The full optical setup is shown in Fig. 2.11.
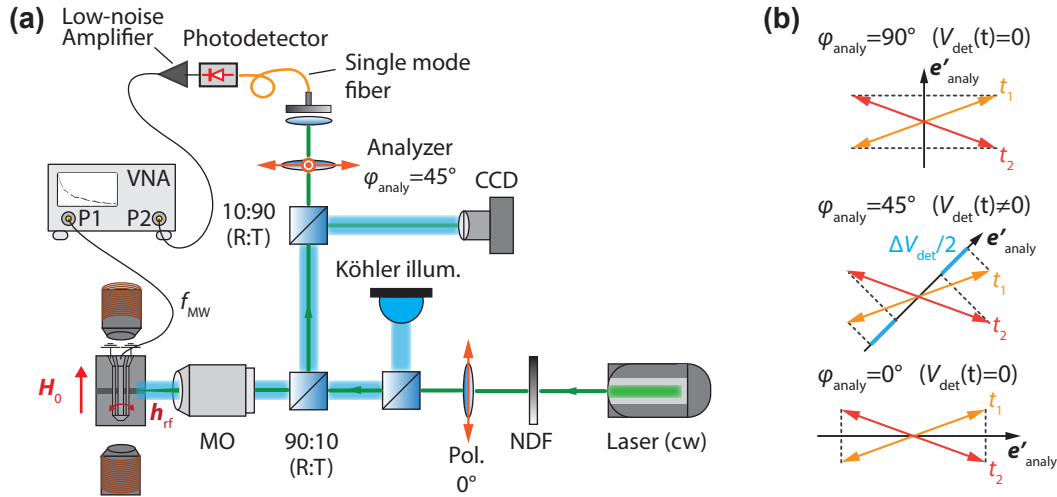
Figure 2.11: (**a**) Schematic representation of the microfocused frequency-resolved magneto-optic Kerr effect (µFR-MOKE) setup. (**b**) Analyzer at different angle positions φ_{analy} to visualize that the detected voltage at the photodetector $V_{\text{det}}(t)$ depends on the direction of the polarization axis $\acute{e}_{\text{analy}}$. The arrows (orange and red) represent the two extreme values of polarization at times t_1 and t_2. Figure taken from [36].

In this experiment, we have used a continuous wave (cw) laser (Laser Quantum Torus 532, $\lambda = 532.2$ nm, $P_{\text{max}} = 180$ mW) which passes through a neutral density filter (NDF) to adjust the laser power to the desired value. Then, the laser light is passed through a Glan-Thompson polarizer to get a clearly defined linear polarization before focusing it onto the sample. The laser beam is focused onto the sample through the microscope objective (MO). We illuminated the sample homogenously by a Köhler- illumination so that we can see the sample and do the measurements in a spatially-resolved manner [36]. With the piezo-based nano-positioners, the movement of the sample in all three dimensions (spatial scan and focus) is possible. Therefore, we can precisely determine the position of the laser spot on the sample. For this, the backreflected blue LED light of the Köhler illumination is measured using a CCD camera.

The backreflected laser light, containing the oscillating polarization angle at the frequency of the magnetization dynamics ω_{sw}, is reflected by a non-polarizing beamsplitter. The 90% of the light reflected at a beamsplitter is then transmitted through another beamsplitter cube which is used for the image acquisition of the sample. Using a zero-order half-wave plate and a polarizing beam splitter cube (the combination of both serves as an analyzer), the oscillation of the polarization is converted to a change in light intensity. We set the angle of the analyzer to $\varphi_{\text{analy}} = 45°$ with respect to the first polarizer, which is the optimal angle for FR-MOKE detection as depicted in Fig. 2.11. After converting the oscillating polarization of the laser beam to an oscillating laser intensity, we couple the laser light into a single-mode FC/APC optical fiber. This optical fiber possesses a fiber coupling efficiency of 50% of the laser intensity. The light impinges through the anti-reflection coated FC/PC end of the fiber on a fast broadband photodetector with a bandwidth of 25 GHz. The signal is then split into its dc and ac component inside the fast photodetector.

The coupling of the total laser power into the optical fiber defines the dc-signal of the photodetector. If the laser light is perfectly parallel before focusing into the fiber, it can be coupled into the optical fiber with highest efficiency. Furthermore, the infinity-corrected microscope objective collects the reflected light from the sample. In order to get parallel reflected light entering the microscope objective, the laser spot must be in focus onto the sample otherwise the laser light diverges and this is crucial for fiber coupling of the backreflected laser light from the sample. The dc voltage of the photodetector is measured by a multimeter and used to actively stabilize the focusing of the laser onto the sample. If we move the nanopositioners in small steps, towards or away form the microscope objective, a change in the dc voltage is observed. To obtain critical focus, the dc signal is maximized by moving the sample stage away from or towards the microscope objective.

A low-noise amplifier is used to amplify the ac-signal of the photodetector and the amplified signal is then sent to port 2 of the VNA. In order to minimize the noise, the VNA is set to an intermediate frequency filter bandwidth of 1 Hz. The complex transmission parameter $S_{21} = \frac{V_2}{V_1}$ along with the phase is then calculated by the VNA. The VNA is also used to excite the magnetization dynamics by applying a microwave frequency f_{MW} at port 1 which is coupled into the microstrip antenna. Here, V_1 is the applied voltage to the microstrip antenna and V_2 is the measured voltage of the photodetector.

Chapter 3

Multilayer Growth and Characterization

Magnetic skyrmions are topologically protected spin textures [52]. They demonstrate potential for ultralow-energy and ultrahigh-density magnetic data storage and computing applications [17]. So far, skyrmions have been observed in materials with OOP magnetization which is achieved either with a perpendicular magnetic anisotropy (PMA) in case of thin films, or an external magnetic field [12]. In thin films, the skyrmions are stabilized by means of a trade-off between the magnetostatic and exchange energy and i-DMI [53]. In a multilayer system, a thin ferromagnetic material is coupled to a large spin–orbit coupling material, such as Ir or Pt as discussed in Sec. 2.2.

The stability of skyrmions highly depends on the applied magnetic field and temperature. This limited region of the parameter space is narrow in bulk materials but larger in magnetic thin films. Thin films, hosting magnetic skyrmions are potential candidates for the applications in information technologies but it is challenging to unite all properties required for applications in a single material system. In order to cope with this challenge, in this thesis, we have investigated the formation of skyrmions at room temperature in a magnetic thin film multilayer (ML) system, which exhibits the easy-plane anisotropy with i-DMI. The stabilization of skyrmions at room-temperature in an entirely metallic thin-film may perhaps be an important step towards real world applications [54].

In order to gain a deeper understanding of such systems, we have fabricated a series of multilayers with different number of repetitions of the trilayer [Pt(0.75)-$Co_{25}Fe_{75}$(1.1)-Ir(0.45)]. For all multilayers we have used the same seed and cap layers. The purpose of changing the number of repeats of the trilayer is to get an insight about the i-DMI strength, anisotropy and damping of the system. Furthermore, we investigated the system with different measurement techniques including ferromagnetic resonance (FMR), superconducting quantum interference device (SQUID) magnetometry and frequency resolved magneto-optic Kerr effect (FR-MOKE). In this chapter we will focus on the findings obtained by FMR and SQUID magnetometry and the results of FR-MOKE will be discussed in chapter 4.

In magnetic materials, the exchange coupling can be quite significant. In a magnetic material, the exchange coupling is strong enough to align magnetic moment even in the absence of external magnetic fields. In a condensed matter system, the magnetic anisotropy energy E_a is the energy which is minimized to describe the orientation of the magnetic moments. The uniaxial anisotropy energy, which describes a single preferred orientation of the magnetic moments is given by

$$E_a = K_u \sin^2 \theta, \tag{3.1}$$

where θ is the polar angle with respect to the surface normal and K_u is the uniaxial anosotropy constant. For the stabilization of skyrmions, a uniaxial anisotropy K_u has so far been assumed to be an important requirement which translates to perpendicular magnetic anisotropy (PMA) in thin film magnetic heterostructures [55]. In a sytem with PMA, the magnetic moments are aligned perpendicular to the film plane. However, there are two main challenges associated with the PMA multilayer skyrmion systems, one is field stability and the other is high magnetic damping.

The effective anisotropy for the multilayers having PMA is given by, $K_{\text{eff}} = K_u - \mu_0 M_s^2/2 > 0$. The $K_u > 0$ represents the easy-axis anisotropy with easy-axis along the film normal (OOP). The second term defines the shape anisotropy where μ_0 is the vacuum permeability and M_s is the saturation magnetization. It has recently been theoretically argued that, when $K_{\text{eff}} < 0$ (easy-plane regime), the formation of skyrmions is still possible [56, 57]. If the i-DMI is sufficiently large to enable skyrmion formation, one could potentially even achieve high field stability that surpasses that of skymrion phases in PMA systems [56, 57]. In easy plane sykrmion systems, thicker ferromagnetic (FM) layers can be used which reduces the spin pumping and ultimately the damping contributions. On that account, we explored the two-dimensional (2D) easy-plane anisotropy in magnetic multilayers for the stabilization of skyrmions.
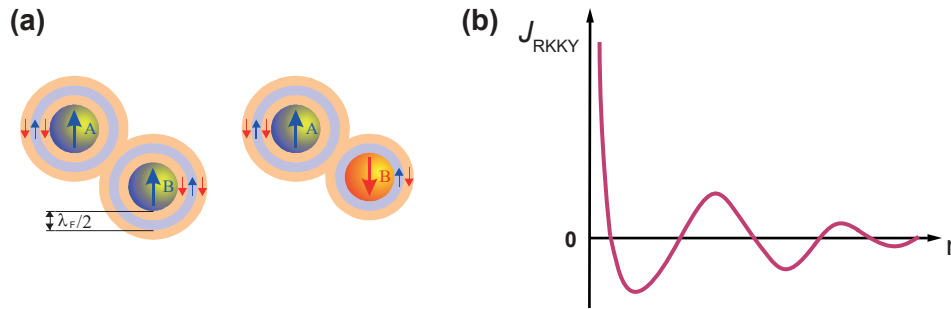
Figure 3.1: (a) The RKKY interaction. Depending on the distance of the localized magnetic moments A and B ferromagnetic (left) or antiferromagnetic order (right) arises. Figure taken from [58]. (b) Oscillatory dependence of J_{RKKY} on the distance between the localized magnetic moments.

The interlayer exchange strength is another important factor which quantifies the interlayer coupling of the metallic thin films. The Ruderman–Kittel–Kasuya–Yosida (RKKY) exchange interaction is the major contribution in such systems. The mechanism of RKKY coupling is illustrated in Fig. 3.1. In RKKY, the exchange interaction between magnetic ions is mediated by conduction electrons. The conduction electrons are spin polarized by a localized magnetic moment which in turn couple to a neighbouring localized magnetic moment a distance r away. The interaction does not involve direct coupling between magnetic moments thus, the exchange interaction is indirect. The distance dependent exchange interaction is defined by the relation

$$J_{\mathrm{RKKY}}(r) \propto \frac{\cos(2k_{\mathrm{F}}r)}{r^3}, \tag{3.2}$$

where k_{F} is the fermi wave number and r is the distance between the localized magnetic moments. The interaction is long range and shows an oscillatory dependence on the distance between the magnetic moments. Therefore, the RKKY coupling may be either ferromagnetic or antiferromagnetic depending on the distance between the localized magnetic moments. The osillatory coupling has a wavelength $\lambda_{\mathrm{F}} = 2\pi/k_{\mathrm{F}}$ [22].
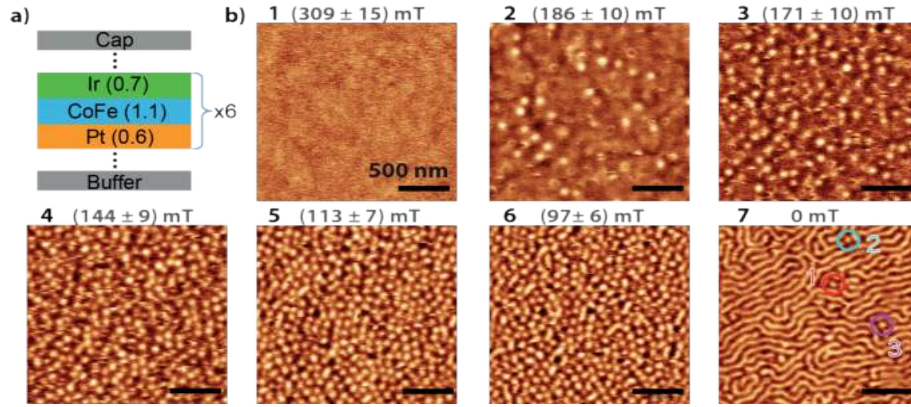
Figure 3.2: (**a**) Multilayer system with N = 6 of the Pt − CoFe − Ir trilayer. (**b**) Recorded MFM images with OOP magnetic field configuration. The field vales are indicated at the top of each frame. On decreasing field to minimum, the magnetic texture shows transitions from a saturated ferromagnetic state 1, to isolated skyrmions (2, 3), a dense skyrmion arrangement (4 − 6) and eventually forms a maze state at zero field (7). Figure taken from [59] .

We now move to an overview of our multilayer sytem. In our multilayer sytem, the formation of skyrmions has been confirmed via magnetic force microscopy (MFM), which has been done for a similar kind of sample with N = 6 by Luis Flacke in collaboration with the group of Markus Becherer (TUM). Though MFM is beyond the scope of this thesis, the results are shared here for completeness. The MFM images of multilayer system are shown in Fig. 3.2. In this figure, the MFM contrast images are presented which are recorded with external magnetic field $0 \ \mathrm{mT} \leqslant \mu_0 H_0 \leqslant 309 \ \mathrm{mT}$ applied in the OOP direction.

Image **1** shows a smooth texture without any contrast as the sample is magnetically saturated with all magnetic moments aligned parallel to the applied magnetic field. Image **2** features small individual dots which start to emerge when the field is reduced below the saturation magnetic field and we attribute this to skyrmion formation. The density of skyrmions increases if we decrease the field until we get a dense and unordered skyrmion arrangement which as depicted in images (**3** − **6**). Eventually, at remanence, the formation of a maze-state is observed as shown in image **7**. Interestingly, we can observe that, even at $H_0 = 0$, individual skyrmions (as highlighted with the three circles) can maintain their stabilization. Thus, our multilayer system hosts skyrmions for $0 \ \mathrm{mT} \leqslant \mu_0 H_0 \leqslant 190 \ \mathrm{mT}$.

This is approximately twice the field range reported for PMA systems [60, 61]. After a brief introduction of our multilayer system, now in the next section we will discuss the adopted fabrication method and the measurement techniques.

3.1 Sample Fabrication

For our experiments we have grown the multilayers on thermally oxidized Si (001) substrates. The samples have been fabricated by magnetron dc-sputter deposition as discussed in Sec. 2.5 and the sputtering parameters are listed in the table A.1 in the Appendix. The multilayer stacking is depicted in Fig. 3.3.
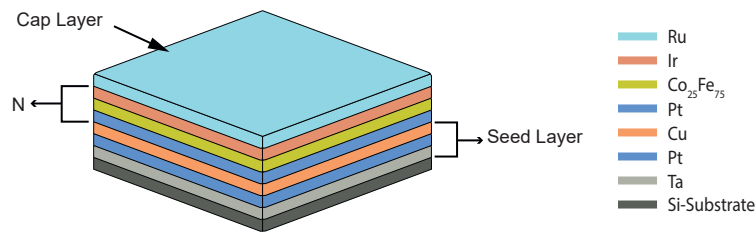
Figure 3.3: Multilayer heterostructue consisting of a substrate, a seed layer, trilayer containing Pt,$Co_{25}Fe_{75}$ and Ir and a cap layer. N is the number of repeats of the trilayer [Pt(0.75)-$Co_{25}Fe_{75}$(1.1)-Ir(0.45)] responsible for the i-DMI and anisotropy and ultimately for the formation of skyrmions. The cap layer protects the multilayer from oxidation and the seed layer ensures optimized growth condition.

We have fabricated a multilayer system consisting of Platinum (Pt) and Iridium (Ir) (known to have large spin–orbit coupling) that enclose a ferromagnetic thin film, which is $Co_{25}Fe_{75}$ in our case. The multilayer hetrostructure is composed of Ta(1.5)-Pt(4)-Cu(2)-[Pt(0.75)-$Co_{25}Fe75$(1.1)-Ir(0.45)]$_N$-Ru(1.5), where the numbers represents the layer thickness in nanometers. The seed layer contains three materials namely Tantalum(1.5), Platinum(4), and Copper(2). Ta is used to improve the adhesion and crystallographic texture of the multilayer [62] whereas, Pt layer is used to introduce the interface anisotropy into the multilayer system [63]. A Cu layer is used to reduce the damping of the system, which otherwise would be higher due to the direct spin pumping into Pt [64]. Here Ruthenium has been used as a cap layer to prevent oxidation. We have fabricated different multilayers containing different number of repeats of the trilayer [Pt(0.75)-$Co_{25}Fe_{75}$(1.1)-Ir(0.45)]$_N$ where N is the number of repetitions from 2 to 7.

3.2 SQUID Magnetometry

There are many ways to determine the magnetic properties of the magnetic materials. The superconducting quantum interference device (SQUID) is the most sensitive magnetic flux detector. This device operates at cryogenic temperatures with quantum-limited sensitivity.

Occasionally, SQUID offers the ability to measure where no other methodology is possible. For this thesis, we determined the magnetic properties of the multilayer samples using an MPMS XL − 7 magnetometer SQUID from Quantum Design. In this setup a superconducting magnet can set a magnetic field $\mu_0 H_0$ from −7 T to 7 T. For the SQUID measurements, we first need to set the temperature $T = 300$ K and put the sample in a helium gas flow. The main part of the measurement setup is the second-order gradiometer which is shown in Fig. 3.4 (a). The gradiometer comprises four turns of a superconducting wire. Two clockwise loops are in the center of the structure and two individual counter clockwise loops are attached 1.5 cm apart on either side. If any field gradients appear, then they are averaged out because of this arrangement. The sample is inserted and fixed inside a plastic straw. The sample, which is now inside the straw is moved through all four turns. Thereby it induces a current into the turns due to its magnetic moment. The measurement curve resulting from different winding directions is also depicted in Fig. 3.4 (b). This curve is a direct measure of the sample's magnetic moment which can be evaluated. There are various modes of operation which can be chosen for the measurements.

With a DC measurement, the sample is moved step by step through the gradiometer and the measurement curve is recorded. This method is used to center the sample inside the gradiometer. In RSO (reciprocating sample oscillation) mode, the sample is passed through the structure several times in a sinusoidal movement. The change in the induced current, i.e. the first derivative, is measured using lock-in technology. The RSO method is used for magnetization measurements as a function of magnetic field and temperature [65].
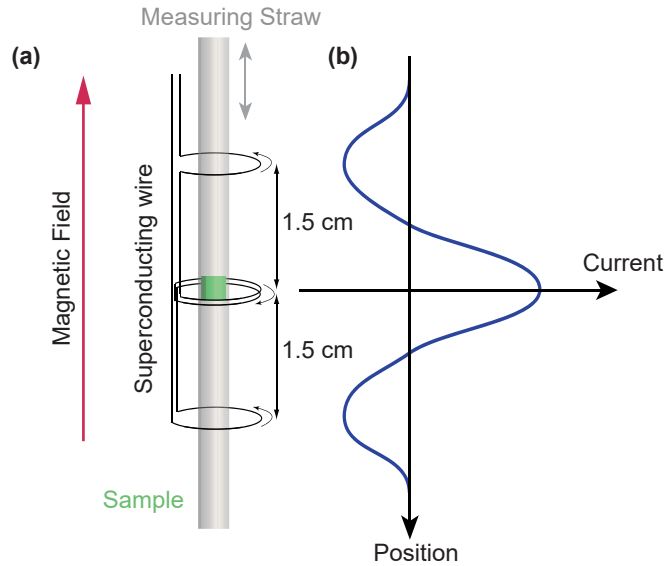
Figure 3.4: (**a**) Construction of a second order gradiometer of SQUID magnetometer.(**b**) The measured current as a function of the sample location. Figure adopted from [65].

Now we want to discuss the results obtained by superconducting quantum interference device (SQUID) magnetometry for our multilayer system. The IP and OOP hysteresis curves are displayed in Fig. 3.5 (a) and (b). The IP hysteresis curve confirms the easy
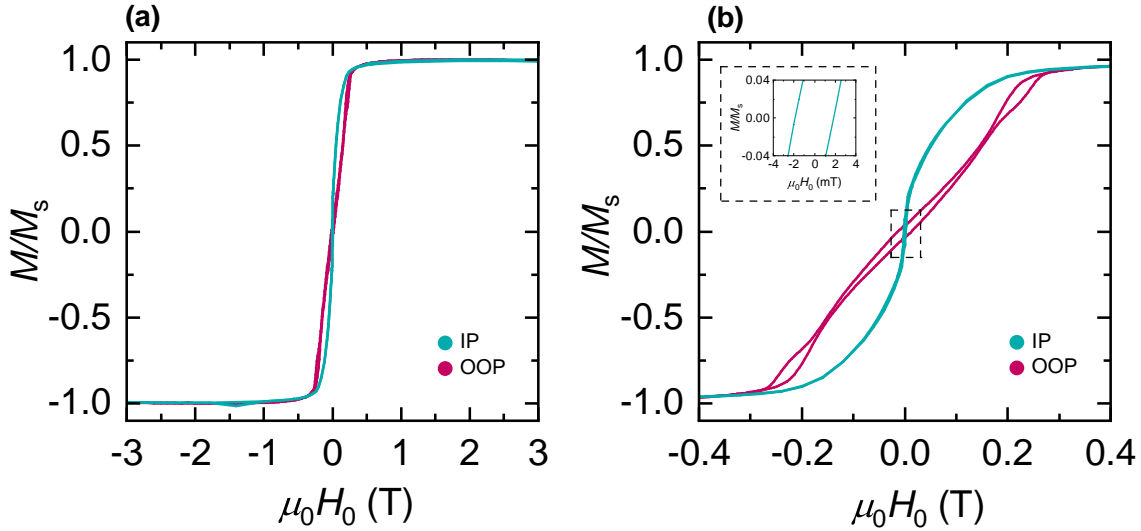
Figure 3.5: (**a**) The hysteresis curves from the multilayer sample with N = 6 are obtained by SQUID magnetometry in IP and OOP direction. The IP curve demonstrate an easy-plane switching loop. (**b**) Enlarged view of the same measurement. The OOP configuration behaves like a hard axis. When $\mu_0 H_0 < 200$ mT, the decrease of magnetic moment is attributed to domain formation due to i-DMI. Two small loops on both sides of the OOP curve, indicates the interlayer coupling as a ferromagnetic RKKY coupling. Inset: IP configuration, showing coercivity of about 2 mT.

plane anisotropy in our multilayer system. Qualitatively, the IP hysteresis curve behaves differently than the OOP curve and also from PMA systems, where the IP curve behaves like a hard-axis. Moreover, the IP curve is an easy-plane switching loop with coercivity about 2 mT which can be seen in the inset. Now if we look at the OOP hysteresis curve, it shows that the OOP direction behaves like a hard axis of the system with coercivity of about 20 mT. Furthermore, it is a characteristic curve for the systems where skyrmions and maze-state are often formed. The $K_{\text{eff}} > 0$ systems, having maze-state can also exhibit a similar hysteresis curve due to domain formation [16]. In our multilayer system, if we gradually decrease the field below 200 mT in OOP configuration, domain formation takes place. Despite the easy-plane anisotropy, the formation of a labyrinthine state at remanence is accredited to the strong i-DMI. In the OOP curve, the small loops on both sides of the curve indicates ferromagnetic RKKY interlayer coupling.[59].

3.3 Magnetization Dynamics in Multilayer

In this section we investigate the magnetization dynamics of our multilayer system. Our experiments are performed using a broadband ferromagnetic resonance setup with a coplanar waveguide (CPW) and a vector network analyzer (VNA) as discussed in Sec. 2.4.

3.3.1 Sample Orientation

For our FMR measurements, we first need to attach our sample to a CPW which could be done with a tape as in our case. A sample is placed in a flip-chip style on the CPW. In
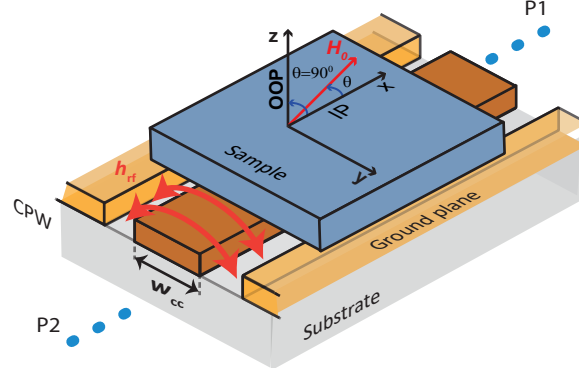
Figure 3.6: The orientation of sample in in-plane (IP) and out-of-plane (OOP) configuration. The sample is placed with respect to the direction of applied static magnetic field (red arrow). The sample is placed in a flip-chip style.

order to achieve a homogeneous excitation field over the whole sample, the longer side of the sample is placed parallel to the center conductor of the CPW. If the sample is placed horizontally (with $\theta = 0$) with respect to the applied static magnetic field, then this is called an in-plane (IP) configuration, as shown in Fig. 3.6. On the other hand, if the sample is placed vertically (with $\theta = 90°$) with respect to the the applied static magnetic field, then we refer to this configuration as the out-of-plane (OOP) configuration. We also have performed some other FMR measurements for our multilayer with oblique magnetic field angles where $0 \leqslant \theta \leqslant 90°$ which we will discuss in the next section.

3.3.2 FMR Spectroscopy

In this section, we will discuss the results obtained from the FMR spectroscopy for our multilayer system. The dynamic characteristics of a ferromagnetic material define the important properties such as damping, anisotropies and the dispersion relation of a ferromagnetic material. Therefore, the FMR spectroscopy plays a vital role in the field of spintronics and magnonics. With the VNA-FMR setup one can measure in a broad range of frequencies and both the amplitude and phase of the signal can be extracted. In order to scan the resonance using VNA, two different methods can be employed. In first method, we fix the microwave frequency and sweep the magnetic field (field-swept FMR), where the VNA is set into the continuous wave (cw) mode. The IF-bandwidth is set to a few Hz to improve the signal to noise ratio but one should keep in mind that, the measurement time scales inverse to the IF-bandwidth. Therefore, its is not practically feasible to always measure at lowest possible IF-bandwidth. In the second method, we fix the magnetic field at a certain value and sweep the VNA frequency (frequency-swept FMR), where the VNA operates in the linear frequency sweep mode.

In FMR measurements, we deal with different microwave losses in the whole setup. The potential sources for these losses could be endlaunches, cables and the impedance mismatch due to the sample on the CPW. These losses are generally frequency and temperate dependent. The frequency-dependent background transmission parameter $S_{21}^0(\omega)$ contains all losses. The total transmission parameter then takes the form [24]

$$S_{21}(\omega, H_0) = S_{21}^0(\omega) - i\,A e^{i\phi}\chi_{yy}(\omega, H_0), \tag{3.3}$$

where A and ϕ are amplitude and phase scaling parameters. The main reason for the phase is the finite electrical length of the system. The frequency-dependent background which comes from the setup, always superimposes the signal of the ferromagnetic resonance. The most simple method to overcome this problem is to take a field cut far away from the ferromagnetic resonance at a fixed magnetic field. The slice has to be taken from a magnetic field value where we only measure the transmission of the system and there must not be any contribution from the investigated sample. The complex transmission parameter S_{21} is then divided by this slice. With this division, now we can remove S_{21}^0 from Eq. (3.3) and it can be written as

$$S_{21}^{ds}(\omega)|_{H_0} = 1 - i\,A'e^{i\phi}\chi(\omega, H_0), \tag{3.4}$$

where a new amplitude factor $A' = A/S_{21}^0$ has been introduced.

For all of our measurements we have used only linear frequency mode and the IF bandwidth (responsible for the signal to noise ratio) was fixed at 1 kHz. For a series of measurements, the magnetic field is measured twice for each point, once before the VNA readout and once after the VNA readout and then the average of both values is taken. For our measurements, we have measured the complex transmission parameter S_{21} for a series of fixed magnetic fields with step size of 1 mT. In order to remove the frequency-dependent background, we have utilized the background correction method called derivative divid (d_D) (developed at the Walther-Meißner-Institut) [66].

In derivative divide the central difference quotient of the transmission parameter S_{21} with respect to the magnetic field H_0 is calculated and the result is divided by the central value of S_{21}:

$$d_D S_{21} = \frac{S_{21}(\omega, H_0 + \Delta H_{\mathrm{mod}}) - S_{21}(\omega, H_0 - \Delta H_{\mathrm{mod}})}{S_{21}(\omega, H_0)\Delta H_{\mathrm{mod}}}$$

$$\approx -i\omega A\,\frac{\chi(\omega, H_0 + \Delta H_{\mathrm{mod}}) - \chi(\omega, H_0 - \Delta H_{\mathrm{mod}})}{\Delta H_{\mathrm{mod}}}. \tag{3.5}$$

The central difference quotient gives us the freedom to set the finite step size ΔH_{mod}. The division of Eq. (3.5) by S_{21} cancels the transmission and phase of the background $S_{21}^0(\omega)$. If we choose small field steps H_{mod}, the central difference quotient is approximated by the derivative with respect to the external magnetic field H_0 as χ varies smoothly with field

and frequency and the partial derevitive $(\mathrm{d}\omega/\mathrm{d}H_0)$ can be merged in $A \longrightarrow A'$. Therefore,

$$\mathrm{d_D}S_{21} = -i\omega A \frac{\mathrm{d}\chi}{\mathrm{d}H_0} = -i\omega A' \frac{\mathrm{d}\chi}{\mathrm{d}\omega}. \tag{3.6}$$

The distortion of the line needs to be taken into account when $\Delta\omega_{\mathrm{mod}}$ is of the order of $\Delta\omega$ for a quantitative analysis of $\mathrm{d_D}S_{21}$. Therefore, the central difference quotient is numerically calculated and fitted instead of $\frac{\mathrm{d}\chi}{\mathrm{d}\omega}$ in Eq. (3.6) and we obtain

$$\mathrm{d_D}S_{21} = -i\omega A' \frac{\chi(\omega + \Delta\omega_{\mathrm{mod}}) - \chi(\omega - \Delta\omega_{\mathrm{mod}})}{2\Delta\omega_{\mathrm{mod}}}, \tag{3.7}$$

with modulation amplitude $\Delta\omega_{\mathrm{mod}} \approx \gamma\mu_0\Delta H_{\mathrm{mod}}$. If the background and features in the data vary way faster or slower than the expected FMR linewidth then the derivative divide suppresses the variations.

The background-corrected FMR plots for a multilayer with N = 7, as a function of external magnetic field H_0 and frequency f are shown in Fig. 3.7. The FMR plots are taken for different configurations ($0 \leqslant \theta \leqslant 90°$) including IP and OOP. As we see in Fig. 3.7 (a), which is an OOP configuration, there is a ferromagnetic resonance (FMR) of the fully aligned $\mathrm{Co}_{25}\mathrm{Fe}_{75}$ magnetization with $\mu_0H_0 > 200$ mT. This ferromagnetic resonance follows the OOP Kittel equation which was discussed before in Sec. 2.19. In this equation the saturation magnetization M_s is given by [67]
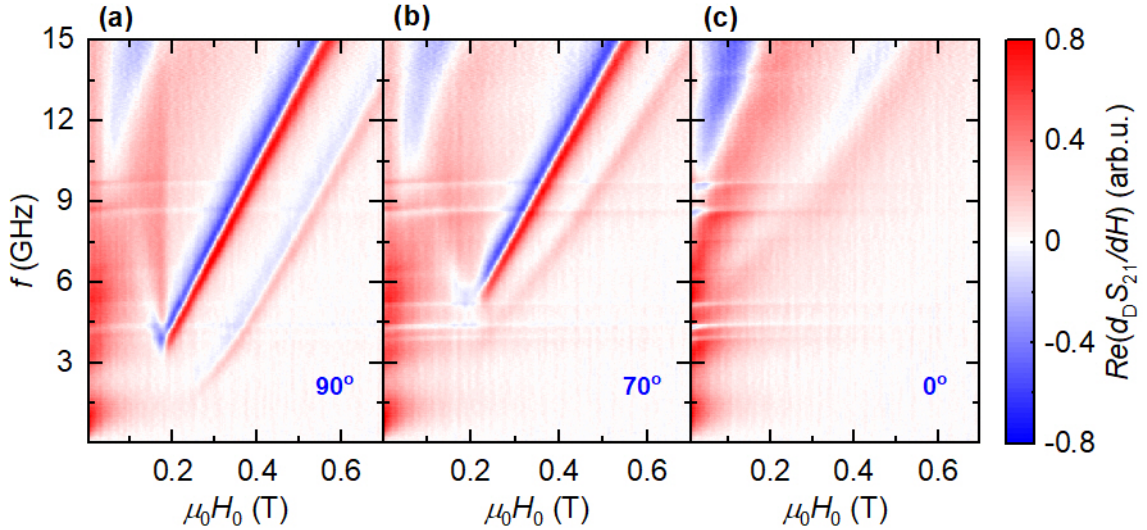
Figure 3.7: The color plots show the real part of the FMR signals with corrected background. (**a**) For $\mu_0H_0 > 200$ mT applied along the OOP direction we see the characteristic ferromagnetic resonance of the multilayer. Below the critical field we see an additional dynamic response, which we attribute to the skyrmion background. (**b**) The same measurement is repeated with a different orientation of the sample where $\theta = 70°$ showing a weaker FMR signal for $\mu_0H_0 < 200$ mT. (**c**) Measurement with IP ($\theta = 0$) configuration where one could barely see any signal.

$$M_\mathrm{s} = M_\mathrm{eff} + H_\mathrm{K}, \tag{3.8}$$

where, $H_\mathrm{K} = 2K_\mathrm{u}/\mu_0 M_\mathrm{s}$, is the perpendicular anisotropy field. Interestingly, we can see that, when $\mu_0 H_0 < 200$ mT, the f_res starts increasing with decreasing magnetic field and the response of f_res vs. H_0 is qualitatively different than $\mu_0 H_0 > 200$ mT. This is ascribed to the rotation of M towards the film plane. Thus, the formation of a nonuniform magnetic texture takes place, which is in agreement with our MFM and SQUID magnetometry results. Here we consider that the resonance observed below 200 mT is the dynamic precession of the magnetic moments in the quasi-uniform background (it can be seen in Fig. 3.2) and not the spin dynamics within the skyrmions. This behavior is aligned with the vanishing amplitude of the resonance towards $H_0 = 0$ as there is no uniform background left. One more observation we have made here is an additional FMR signal though it is not as strong as the one at higher frequency. We assume that this additional or weaker signal appears if all layers of the multilayer are not fully coupled instead, they are coupled in a form of sets of layers.

We repeated the same set of our measurement for a different configuration with $\theta = 70°$ and $\theta = 0$ (IP) and observed the angle dependence on the spin dynamics, as shown in Fig. 3.7 (b) and (c). In Fig. 3.7 (b) we observe that, by changing the direction of the applied static magnetic field onto the sample, the FMR signals below 200 mT are not as strong as in the OOP configuration. If we further decrease the angle and reach the IP ($\theta = 0$) configuration then FMR signals almost disappear. Therefore, one could deduce that the formation of skyrmion highly depends on the direction of applied field and the most dense state exists in OOP configuration only.

3.3.3 Data Processing and Fitting for S_{21}

The raw data obtained from VNA resembles a complex Lorentzian function and can be fitted. Here we have used a home-built labview-routine [68]. The fitting function for the FMR signal is given by

$$S_{21}|_f = A + B \cdot H_0 + Z \cdot e^{i\Phi} \underbrace{\frac{\left(H_0 + M_\mathrm{eff} - i\frac{\Delta H_\mathrm{FWHM}}{2}\right)}{\left(H_0 + M_\mathrm{eff} - i\frac{\Delta H_\mathrm{FWHM}}{2}\right)\left(H_0 - i\frac{\Delta H_\mathrm{FWHM}}{2}\right) - \left(\frac{\omega}{\mu_0\gamma}\right)^2}}_{\chi_{yy}(H)/M}, \tag{3.9}$$

here $S_{21}^0 = A + B \cdot H_0$. The parameters $A, B \in \mathbb{C}$ describes the linearly field dependent transmission and Z, Φ, M_eff, ΔH_FWHM, $g \in \mathbb{R}$ describes the resonance peak. As the resonance field H_res depends on both M_eff and Landé-factor g, we can not determine these parameters from a transmission measurement at a single frequency therefore, a fit is not possible. A solution to this problem is given by Nembach *et al.* [69], who proved that we can extract the M_eff via resonance field H_res by setting the Landé-factor g with an arbitrary fixed value i.e., 2 in Eq. (3.10) and it does not influence any of the final results for H_res and ΔH_FWHM.

$$S_{21}|_f = A + B \cdot H_0 + Z \cdot e^{i\Phi} \frac{\left(H_0 + \frac{\left(\frac{\omega}{\mu_0\gamma}\right)^2 - H_{\text{res}}{}^2}{H_{\text{res}}} - i\frac{\Delta H_{\text{FWHM}}}{2} \right)}{\left(H_0 + \frac{\left(\frac{\omega}{\mu_0\gamma}\right)^2 - H_{\text{res}}{}^2}{H_{\text{res}}} - i\frac{\Delta H_{\text{FWHM}}}{2} \right)\left(H_0 - i\frac{\Delta H_{\text{FWHM}}}{2} \right) - \left(\frac{\omega}{\mu_0\gamma}\right)^2}$$

(3.10)

Now with Eq. (3.10) we can fit the transmission measurements at constant frequency and extract the fit parameters A, B, Z, Φ, H_{res} and ΔH_{FWHM}. For IP condition, the H_{eff} lies in the the film plane whereas, for OOP case the H_{eff} points out of the film plane. We can find the resonance field from Eq. (2.17) but this time we will set $\det\chi^{-1} = 0$ and solve it for the field H_0. Thus we get the H_{res} for IP and OOP configurations. The H_{res} for the IP case takes the form

$$H_{\text{res}} = \sqrt{\left(\frac{\omega}{\mu_0\gamma}\right)^2 + \left(\frac{M_{\text{eff}}}{2}\right)^2} - \left(\frac{M_{\text{eff}}}{2}\right), \tag{3.11}$$

where $M_{\text{eff}} = M_{\text{s}} - H_{\text{K}}$. We note that it is not possible to differentiate between H_{K} and M_{s} when the external field is applied in a single direction. Similarly, for OOP case the H_{res} is given by

$$H_{\text{res}} = \frac{\omega}{\mu_0\gamma} + M_{\text{eff}}. \tag{3.12}$$

After finding the H_{res} and ΔH_{FWHM} for every single frequency of the VNA, now we can fit the data. By fitting H_{res} data with their respective frequencies f into Eq. (3.11) and Eq. (3.12), the values of $\mu_0 M_{\text{eff}}$ and g can be extracted for IP and OOP configuration receptively. Similarly, we fit the ΔH_{FWHM} data with their respective frequencies f using Eq. (2.22) and put the calculated value of g which we take from the first calculation and find the Gilbert-damping parameter α and inhomogeneous broadening ΔH_{inh}.

During this work, a series of samples was produced, each sample has the same seed layer and cap layer but only the repetitions N of the trilayer was changed. We wanted to study the effects of repetitions on our multilayer system and to optimize it for example for low-damping. In order to get a better understanding of our multilayer system, we have calculated all of the aforementioned parameters for our multilayer system having trilayers [Pt(0.75)-Co$_{25}$Fe$_{75}$(1.1)-Ir(0.45)] with N = 2 to 7. All values are fitted in the OOP configuration only. Fig. 3.8 display the fitted parameters.

The Gilbert damping constant α is described as a viscous relaxation of the ferromagnetic resonance. It plays a vital role in spin dynamics of ferromagnetic systems. The switching of magnetization is of importance for application in magneto-electronic devices but magnetic damping can significantly effect the switching of magnetization. The damping constant basically originates from the spin-orbit interaction and leads to a torque exerted on the magnetization as its direction varies with time [70, 71]. By measuring the Gilbert damping parameter, we gain information about the spin precession life time. A multilayer system with low damping is expected to result in a considerable improvement for skyrmion
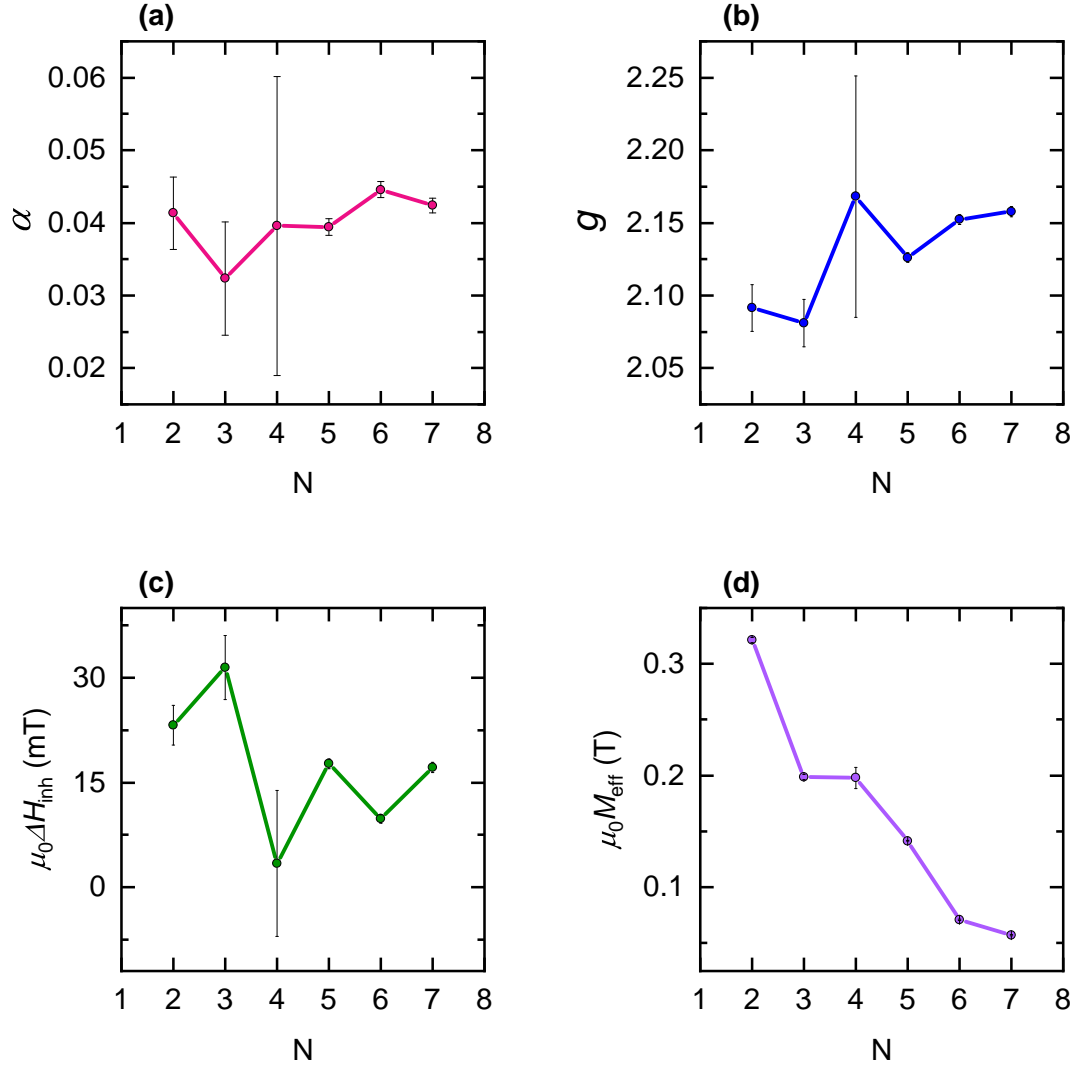
Figure 3.8: (a) Gilber damping α vs. number of repetitions N of the trilayer. The damping parameter is independent of the number of repeats. Though for all multilayer systems the value ranges between $\alpha = 0.03$ and $\alpha = 0.04$ which is comparably low. **(b)** Linearly increasing Landé-factor g as a function of N showing asymmetry in the orbital moment. **(c)** The inhomogeneous line broadening $\mu_0 \Delta H_{inh}$ is also independent of the repetitions of trilayer. The $\mu_0 \Delta H_{inh}$ is attributed to an inhomogeneity of the local resonance field and roughness of the interfaces. **(d)** The values of $\mu_0 \Delta M_{eff}$ for all multilayers are positive. The $\mu_0 \Delta M_{eff}$ decreases linearly with N, indicating the increment in uniaxial anisotropy K_u.

motion. Looking at Gilbert damping in Fig. 3.8 (a) one could observe that the damping is independent of the repetition of the trilayer. Importantly, for all multilayer systems the value ranges between $\alpha = 0.03$ and $\alpha = 0.04$ which is still lower than reported for PMA systems in Refs. [16, 72, 73].

The g-factor is related to the gryomagnetic ratio by $g = \gamma\hbar/\mu$ where $\hbar$ is the reduced Planck constant. In case of ferromagnets $g \approx 2$ because the magnetism is dominated by the spin of electrons. If the spin-orbit coupling of a free electron is considered then it takes the value $g = 2.0023$ [22]. In a saturated state, the spin moment in the system is considered to be isotropic and the asymmetry in the g-factor is a reflection of the the orbital moment asymmetry. When we investigate the g-factor as illustrated in Fig. 3.8 (b), we can see that g is greater than 2 for all the data presented. Additionally, an asymmetry in the orbital moment is observed as we see a linear trend where g-factor increases slightly as the thickness of the trilayer increases. This asymmetry in the orbital moment might be because of magnetoelastic effects. Moreover, this behavior advocates a perturbation of the electron orbits at the interface [74].

The inhomogeneous linewidth broadening $\mu_0\Delta H_{\text{inh}}$ in Fig. 3.8 (c) suggests that like α, the inhomogeneous linewidth broadening is also independent of the number of repetitions of the trilayer. Generally the $\mu_0\Delta H_{\text{inh}}$ is attributed to an inhomogeneity of the local resonance field, roughness of the interfaces or two-magnon scattering processes [69, 75].
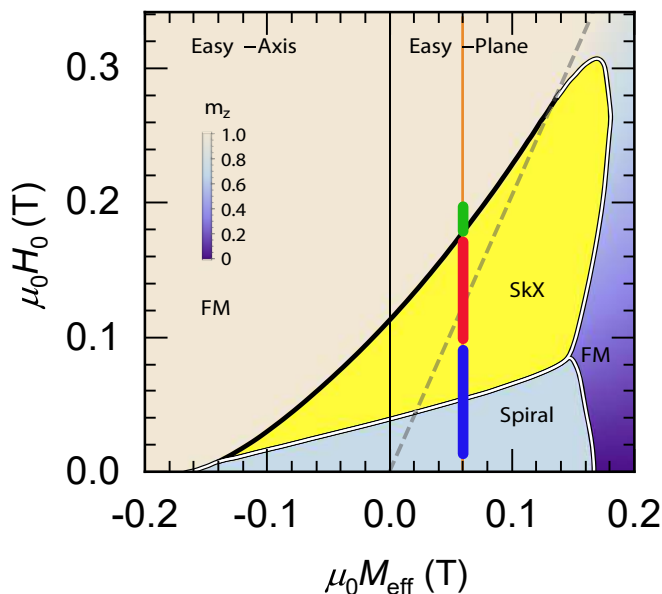
In the Kittel equation, usually the saturation magnetization M_s is considered when only shape anisotropy is relevant as presented in Eq. (2.20) and Eq. (2.19). In case, when other anisotropies have significance then it is customary to replace the absolute magnetization with the so-called effective magnetization M_{eff}. Along the applied magnetic field axis, the M_{eff} is fundamentally identical to the anisotropy field. The M_{eff} is related to the anisotropy field H_{ani} by $M_{\text{eff}} = -H_{\text{ani}} = M_\perp - H_K$ along the $+\hat{z}$ axis as already shown in Eq. (3.8). The H_{ani} is parameterized by the demagnetization field $H_{\text{shape}} = -M_\perp$ along the $-\hat{z}$ axis and the anisotropy field H_K of the additional perpendicular anisotropy along the $+\hat{z}$ axis. If M_{eff} is positive then $M > H_K$ therefore, it indicates that the shape anisotropy dominates and the film plane is a magnetically easy-plane while the OOP direction is a magnetically hard axis. On the other hand, if M_{eff} is negative then it indicates that the OOP direction is a magnetically easy-axis [76].

Now if we look onto Fig. 3.8 (d) we see that the values of $\mu_0\Delta M_{\text{eff}}$ for all multilayers are positive which is a strong indication of having an easy-plane multilayer system. There is a linear trend with M_{eff} decreasing with number of repeats of the trilayer which indicates that the perpendicular anisotropy $H_K = 2K_u/\mu_0 M_s$ or uniaxial anisotropy is increasing with the number of repetitions of the trilayer.

3.4 Comparison of Results

As we have seen, our easy-plane multilayer system is purely metallic and able to stabilize the skyrmions at room temperature over a wide range of external magnetic field. The value of the i-DMI constant has been found by BLS measurements in collaboration with the TU Kaiserslautern and it is $D_{\text{in}} \approx 1.90$ mJ/m^2 thus, a fixed chirality of skyrmions is

expected. It has been reported in Ref. [14] that a multilayer with low magnetic damping could extensively improve the skyrmion motion. A multilayer system with PMA is supposed to have high damping of the magnetization dynamics due to spin pumping to the materials with large spin-orbit coupling. Our multilayer system with $K_{\text{eff}} < 0$, has comparably low damping.

The Gilbert damping parameter for our multilayer is found to be $\alpha = 0.04 \pm 0.001$ which is an order of magnitude lower than that for the multilayer reported in Refs. [16, 72]. Co is also a commonly used ferromagnetic material and has been used for the stabilization of skyrmion but the Gilbert damping is found to be $\alpha \approx 0.3$ for different layer thicknesses [73]. Banerjee *et al.* [56] have recently theoretically proposed that skyrmions can be readily stabilized with 2D easy-plane sytem. Such system demonstrate a large stable skyrmion phase over a large range of magnetic fields and our results are in agreement with their theoretical analysis. We have adopted the phase diagram derived in Ref. [56] to our unit conventions. The phase diagram can be seen in Fig. 3.9.

Figure 3.9: The M_{eff} vs. H_0 phase diagram with ferromagnetic, spiral, and skyrmion crystal phases. The double lines and single line denotes the first-order and unusual first-order transition respectively. The grey dashed line separating the out-of-plane FM from the tilted FM. The orange line represents the value of $\mu_0 M_{\text{eff}}$ of our multilayer system along with three other lines blue, red and green indicating three different stages of the skyrmions stabilization. Blue indicates the less dense state including the maze-like state, red is the most dense state while green shows the region where the nucleation of skyrmions takes place.

For reference, here we have used the data for the N $=$ 7 multilayer with saturation magnetization $M_{\text{s}} = 1200$ kA/m determined from SQUID measurements, the DMI constant $D_{\text{in}} = 1.9$ mJ/m^2 and exchange constant $J =22$ pJ/m found via Brillouin light scattering

(BLS). In order to transform the axes of the phase diagram of Ref. [56] to our unit conventions, we have used Eq. (3.13) and Eq. (3.14) and plunged in the values of D_{in}, J and M_{s} from our measurements data.

$$\frac{AJ}{D_{\text{in}}^2} = \frac{JM_{\text{s}}\mu_0 M_{\text{eff}}}{D_{\text{in}}^2} \tag{3.13}$$

$$\frac{HJ}{D_{\text{in}}^2} = \frac{JM_{\text{s}}\mu_0 H_0}{D_{\text{in}}^2} \tag{3.14}$$

By taking into account, the effective magnetization $\mu_0 M_{\text{eff}} = 0.057 \pm 5.5 \times 10^{-4}$ T which is determined from our FMR measurements, we can observe that our multilayer system is in agreement with this prediction of easy-plane system. However, there are some minor discrepancies which might be because of the uncertainty in our experimentally determined i-DMI strength or exchange constant. In the phase diagram, the orange line represents the value of $\mu_0 M_{\text{eff}}$ of our multilayer system. On top of this orange line, three different phases of skyrmions stabilization have been represented. The blue line shows the less dense and the maze-like state with the field values 0 mT $\leqslant \mu_0 H_0 \leqslant 90$ mT. The red line is associated with the dense skyrmion state with the field range 90 mT $\leqslant \mu_0 H_0 \leqslant 170$ mT. Whereas, the small green line shows the region where skyrmion nucleation start taking place. On comparison with other experimentally realized easy-plane skyrmion systems, bulk or thin films [18, 77], polar magnets and DMI less super-lattices [78, 79] we come to a conclusion that our multilayer system is an exceptional as it can stabilize skyrmions at room temperature over a wide range of external magnetic fields.

3.5 Summary

In this chapter, we have done detailed investigation of 2D easy-plane metallic thin film multilayer heterostructures. We fabricated our multilayers with an ultra-high-vacuum (UHV) sputtering chamber. In order to get an in depth analysis of our multilayer system, we used different measurements techniques in particular a VNA-FMR setup to study spin dynamics at room temperature. We additionally used superconducting quantum interference device (SQUID) to determine the static magnetic properties. From these measurements we evaluated the dynamics of the multilayer and determined the other magnetic properties like Gilbert damping α, g-factor, and effective magnetization M_{eff}. Our multilayer system has comparably low damping parameter which is $\alpha \approx 0.04 \pm 0.001$ with a positive value of M_{eff} which is $\mu_0 M_{\text{eff}} = 0.057 \pm 5.5 \times 10^{-4}$ T, indicating an easy-plane multilayer system. The IP and OOP hysteresis curves from SQUID data also confirmed that our multilayer is an easy-plane system with ferromagnetic interlayer coupling.

For further investigation, we fabricated a series of multilayer with different repetitions of the trilayer [Pt(0.75)-Co$_{25}$Fe$_{75}$(1.1)-Ir(0.45)] from 2 to 7 and observed the difference in their behavior using FMR. We compared their FMR data and came to this conclusion that the perpendicular magnetic anisotropy (PMA) of the multilayer is increased with the number of repetitions of the trilayer while damping parameter α and inhomogeneous line

broadening $\mu_0 \Delta H_{\mathrm{inh}}$ are independent of the number of repeats of the trilayer. Furthermore, we evaluated the dependency of the applied external static magnetic field onto the skyrmion formation. From the FMR data, we realized that, the most dense skyrmion state exist only in OOP configuration and the strength of the FMR signal below 200 mT decreases if we move from OOP to IP configuration.

In conclusion, we have seen that our multilayer system can stabilize the skyrmions at room temperature over a wide range of external magnetic field with a decent value of i-DMI constant and low damping. The substantial reduction of damping can result in faster skyrmion motion. Importantly, the results from our multilayer system are in agreement with the theoretical results of Banerjee *et al.* [56] therefore, our 2D easy-plane multilayer system has opened the doors for further research in this direction which could bring a revolution in the field of spintronics.

Chapter 4

Multilayer/Ferromagnetic Hybrid Devices

In the previous chapter, we discussed the characterization of metallic thin film multilayer systems with easy plane anisotropy which can host magnetic skyrmions at room temperature over a large range of external magnetic field with low damping. In this chapter, we want to extend our discussion to metallic thin film ferromagnet/chiral magnet hybrid layers and devices. The multilayer systems hosting skyrmions have recently attracted great interest from the viewpoint of possible applications in novel spintronic devices for example, for information storage and logic technologies [13, 14, 16]. Some applications like, the racetrack memory and magnetic random-access memories (MRAMs) rely on the dynamics of the magnetization. The realization of these devices and the development of novel approaches highly depends on the understanding and control of the magnetization dynamics. The hybrid devices (where the magnetization dynamics are coupled to an external degree of freedom) can be considered as one of the steps towards the realization of such applications. Furthermore, the precise multitasking capabilities such as transmission of information, long-lived memories etc., can be achieved by hybrid systems, which exploit coupling between two physical systems, with complementary performance. Because of their potential applications in coherent information exchange, communication or sensing, hybrid systems have attracted great attention over the last years [80].

The aforementioned applications require strong coupling in order to coherently transfer the information between the systems and their coupling highly depends on the electromagnetic and exchange interactions. In recent years, the microelectronics industry has made tremendous progress in the research and development of novel approaches by exploiting the spin degree of freedom of the electron. Specific applications like frequency up-conversion and quantum state storage may profit from magnetic systems [81]. A hybrid system consisting of a magnon system which is coupled to a photonic system is considered as a potential candidate for microwave information processing and novel storage applications.

Our hybrid system is also a step towards above mentioned applications, which are in need of reinforcement. The hybrid system that we have fabricated for this thesis comprises the same multilayer i.e., Ta(1.5)-Pt(4)-Cu(2)-[Pt(0.75)-Co$_{25}$Fe75(1.1)-Ir(0.45)]$_N$-Ru(1.5) which we have discussed in last chapter but now in addition to that we have deposited a 5 nm or 20 nm thick layer of Co$_{25}$Fe$_{75}$ on top, resulting in two different kind of samples. In the next section of this chapter we will discuss the fabrication process of our multilayer hybrid system. After that, in Sec. 4.2 we will investigate our hybrid system using SQUID magnetometry. The in-depth investigation of the magnetization dynamics of the hybrid

system is included in Sec. 4.3 where we will investigate our system in both IP and OOP configurations as we have done in the last chapter. Moreover, we will show the coupling mechanism between multilayer system and the $Co_{25}Fe_{75}$ layer using FMR. In Sec. 4.4 we will further investigate the magnetization dynamics of our hybrid system using a novel optical spectroscopy method called micro-focused frequency-resolved Magneto-Optic Kerr Effect (µFR-MOKE) which we have already discussed in Sec. 2.7. In the end, we will conclude this chapter with our findings and a summery of our results.

4.1 Sample Fabrication for Hybrid System

Our samples were fabricated via ultra-high-vacuum dc-sputtering just like the multilayer system. For the hybrid system, in addition to the multilayer, we have used a 0.9 nm and 5 nm thick layer of Ru and 5 nm and 20 nm thick layer of $Co_{25}Fe_{75}$ respectively on top of the multilayer, for two different systems. In this system, the Ru layer has been sputtered in between the multilayer and $Co_{25}Fe_{75}$. The Ru layer thereby serves as a spacer layer. One more Ru layer has been sputtered which acts as a cap layer for this system and protects the system from oxidation.

Figure 4.1: Multilayer hybrid system consisting of a substrate, a seed layer, trilayer containing Pt, $Co_{25}Fe_{75}$ and Ir, a spacer layer, an additional layer of $Co_{25}Fe_{75}$ and a cap layer. The N represents the repeats of the trilayer [Pt(0.75)-$Co_{25}Fe_{75}$(1.1)-Ir(0.45)]. One layer of Ru which is between Ir and $Co_{25}Fe_{75}$, acts as an spacer layer between two systems while the other Ru layer is used to prevent the system from oxidation. Ta is used on the very top of the thin film multilayer hybrid system to provide insulation between the microwave antenna and the system.

In addition to the cap layer of Ru we also have used an additional layer of Ta which is on the very top of the system as you can see in Fig. 4.1. In this thesis we have also investigated the magnetization dynamics of ferromagnetic hybrid system with frequency resolved magneto optics Kerr effect which requires an on-chip antenna for the excitation of the spinwaves in the system. Therefore, insulation is required between the hybrid system and the antenna. We have used a layer of Ta on top of the system as Ta is known to oxidize up to a certain depth ($\approx$ 3 nm) of the material and then it acts as an insulator [82]. In the

next section, we will discuss the behavior and characteristics of our hybrid system using
SQUID magnetrometry results.

4.2 SQUID Magnetometry of the Hybrid System

As already discussed in Sec. 3.2, in order to determine the magnetization M of a sample
with high precision as a function of parameters such as external magnetic field $\mu_0 H_0$ or
temperature T, the SQUID magnetometry is used. For our thesis, the SQUID measurements
have been performed for the qualitative analysis of our multilayer hybrid system.
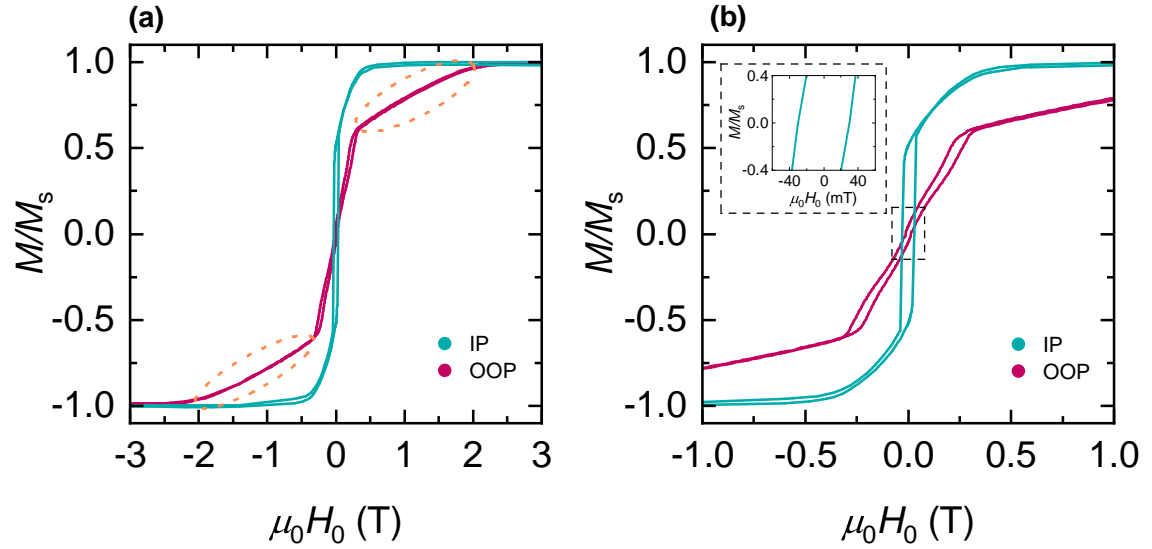
Figure 4.2: (**a**) The hysteresis curves of the ferromagnetic multilayer hybrid system, obtained by
SQUID magnetometry in IP and OOP configuration. The curves are obtained from
the sample Ta(1.5)-Pt(4)-Cu(2)-[Pt(0.75)-$Co_{25}Fe_{75}$(1.1)-Ir(0.45)]$_7$-Ru(0.9)-$Co_{25}Fe_{75}$(5)-
Ru(2). The IP hysteresis curve behaves like an easy axis and demonstrates a sharp
switching of the magnetization of the multilayer with coercive field of about 30 mT.
The curve in OOP configuration behaves like a hard axis with coercivity of about 15
mT. In the OOP curve, there is an additional gentle slope (highlighted with orange
dashed circle on both sides of the curve) which is mainly due the the additional layer of
$Co_{25}Fe_{75}$ on top of the multilayer. (**b**) Enlarged view of the same measurements with
IP and OOP curves. Inset: IP configuration, showing coercivity of about 30 mT.

The magnetic hysteresis curves of the ferromagnetic multilayer haybrid system are shown
in Fig. 4.2 (a) and (b). The measurements are taken from the sample Ta(1.5)-Pt(4)-Cu(2)-
[Pt(0.75)-$Co_{25}Fe_{75}$(1.1)-Ir(0.45)]$_7$-Ru(0.9)-$Co_{25}Fe_{75}$(5)-Ru(2). The loops are recorded by
Superconducting Quantum Interference Device (SQUID) magnetometry as we have done
for our multilayer system. The IP hysteresis curve of the hybrid system which is shown with
a solid green line, exhibits a sharp switching of the magnetization of the multilayer having
coercive field of about 30 mT. However, there is no sharp switching of the magnetization
for the $Co_{25}Fe_{75}$ layer. Instead, there is a smooth increase of the magnetic moment above

40 mT until the magnetization of the system is saturated. The IP hysteresis curve behaves as an easy axis of the system.

The OOP hysteresis curve which is shown with the solid red line does not demonstrates as sharp switching of the magnetization of the multilayer as in the IP configuration. This curve shows coercivity of about 15 mT. Above 0.3 T there is a gentle slope which is indicated by orange circles on both sides of the curve. The slope depicts a comparatively (in comparison with IP configuration) slow increase of the magnetic moment until the magnetization of the thin film is saturated. This slope has appeared as a result of an additional 5 nm thick layer of $Co_{25}Fe_{75}$. The OOP hysteresis curve behaves as a hard axis of the system.

4.3 FMR Spectroscopy of the Hybrid System

The FMR measurements have been performed to understand the magnetization dynamics of our hybrid system. First, we performed the FMR measurements for our sample, Ta(1.5)-Pt(4)-Cu(2)-[Pt(0.75)-$Co_{25}Fe_{75}$(1.1)-Ir(0.45)]$_7$-Ru(0.9)-$Co_{25}Fe_{75}$(5)-Ru(2). Like the multilayer system, for all of our FMR measurements for the hybrid system, we have used only linear frequency mode of the VNA. The IF bandwidth was set to 1 kHz. The field step was again taken as 1 mT and with these settings, a series of measurements was recorded with a fixed external static magnetic field.

Fig. 4.3 shows the background-corrected field-derivative of the VNA transmission spectra $|d_DS_{21}/dH|$ for the multilayer hybrid sample as a function of field μ_0H_0 and frequency f. The color plots show the real part of the FMR signals. Fig. 4.3 (a) display the results of FMR measurements in the OOP configuration. In this figure, there are two FMR signals from two distinct systems i.e., multilayer and 5 nm thick layer of $Co_{25}Fe_{75}$. The FMR signals associated with lower external magnetic field values are from the multilayer only. The FMR signals which are highlighted with the green dashed box come from the additional 5 nm thick layer of $Co_{25}Fe_{75}$.

Now if we observe the FMR signals of the multilayer first, then we can see that, the ferromagnetic resonance of the multilayer is almost the same as we have seen in Sec. 3.3.2 for the multilayer system except an enhanced and more intense signal for $\mu_0H_0 < 400$ mT. The signal below 400 mT, where skyrmion stabilization takes place, gets strengthened, which we attribute to the coupling of the multilayer and $Co_{25}Fe_{75}$. The ferromagnetic resonance for $\mu_0H_0 > 400$ mT follows the OOP Kittel equation, which is given in Sec. 2.19. In Fig. 4.3 (a) we can not see the full signals from $Co_{25}Fe_{75}$ because of the limitations of the applied external static magnetic field from our FMR setup, which is limited to 1.7 T.

The second set of FMR measurements of this hybrid system was taken for $\theta = 80°$. Fig. 4.3 (b) shows the both signals, the signals from multilayer and the signals from $Co_{25}Fe_{75}$ layer. The $Co_{25}Fe_{75}$ resonance forms an avoided crossings with the multilayer FMR signals. This avoided crossing between both signals indicates the presence of coupling between both systems. We have simulated the coupling mechanism of our hybrid system, which we will discuss in the next section. First, we look onto our third set of FMR measurements, shown in Fig. 4.3 (c), which are taken for the IP configuration. Here, one could only see
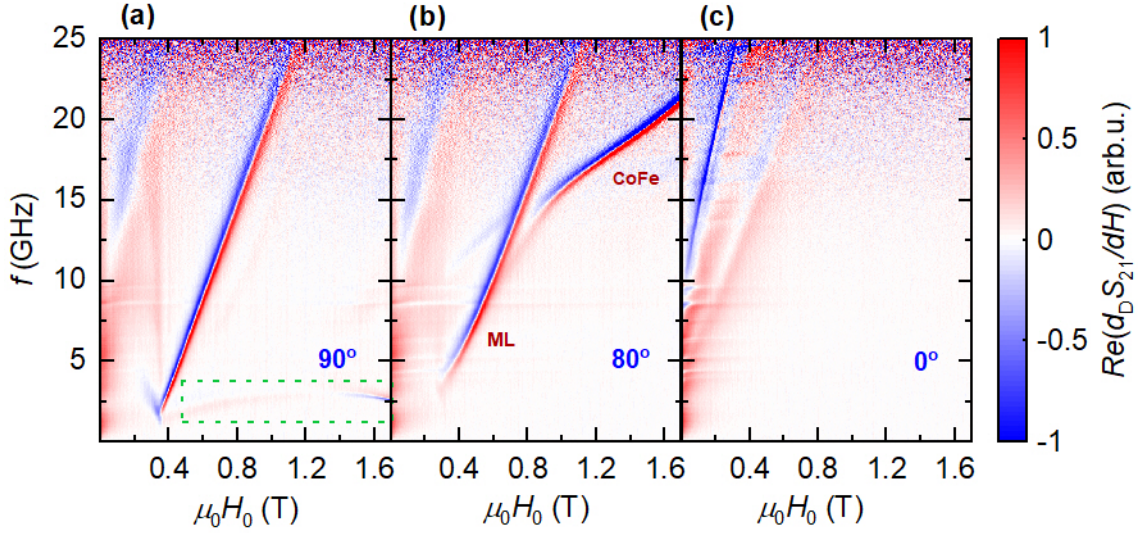
Figure 4.3: The background-corrected field-derivative of the VNA transmission spectra $|\mathrm{d_D}S_{21}/\mathrm{dH}|$ for the multilayer hybrid sample as a function of field μ_0H_0 and frequency f. The color plots show the real part of the FMR signals. (**a**) The FMR signals for OOP configuration where we see the characteristic ferromagnetic resonance of the multilayer for $\mu_0H_0 > 400$ mT. The signals below 400 mT are enhanced because of the additional layer of $Co_{25}Fe_{75}$. (**b**) The FMR measurement for $\theta = 80°$. The anti-crossing can be seen between the $Co_{25}Fe_{75}$ layer and the multilayer which indicates the coupling between both systems. (**c**) Measurement with IP ($\theta = 0$) configuration which shows the signal from $Co_{25}Fe_{75}$ layer only.

the signals from $Co_{25}Fe_{75}$ layer. In this configuration, the signals from the multilayer are weak, such that it is hard to observe them with FMR measurements.

4.3.1 Simulation of Coupling between Multilayer and $Co_{25}Fe_{75}$

In order to show that the multilayer and the $Co_{25}Fe_{75}$ layer are coupled and the avoided crossing between both systems is not just an artifact because of the background correction, we have performed a simulation using a linear function to reproduce our measurement data. In our simulation model, we have used the model of two harmonic oscillators and from our simulation, we will show that both oscillators, the multilayer and the $Co_{25}Fe_{75}$, are coupled. The relation between two oscillators which defines their coupling is given by [83]

$$S_{21}(\omega) = \frac{\kappa_e}{i(\omega - \omega_m) - \kappa_m + \frac{g_c{}^2}{i(\omega-\omega_c)-\kappa_c}}, \tag{4.1}$$

where, g_c is the coupling strength between both oscillators. The κ_e is the external loss rate which defines the coupling of the hybrid system to the CPW and is responsible for the total amplitude of the signal that we measure with the VNA. Here, ω is the excitation frequency and κ_m, κ_c and ω_m, ω_c are the loss rates and resonance frequencies of the multilayer and the $Co_{25}Fe_{75}$ respectively. The results of our simulation are illustrated in
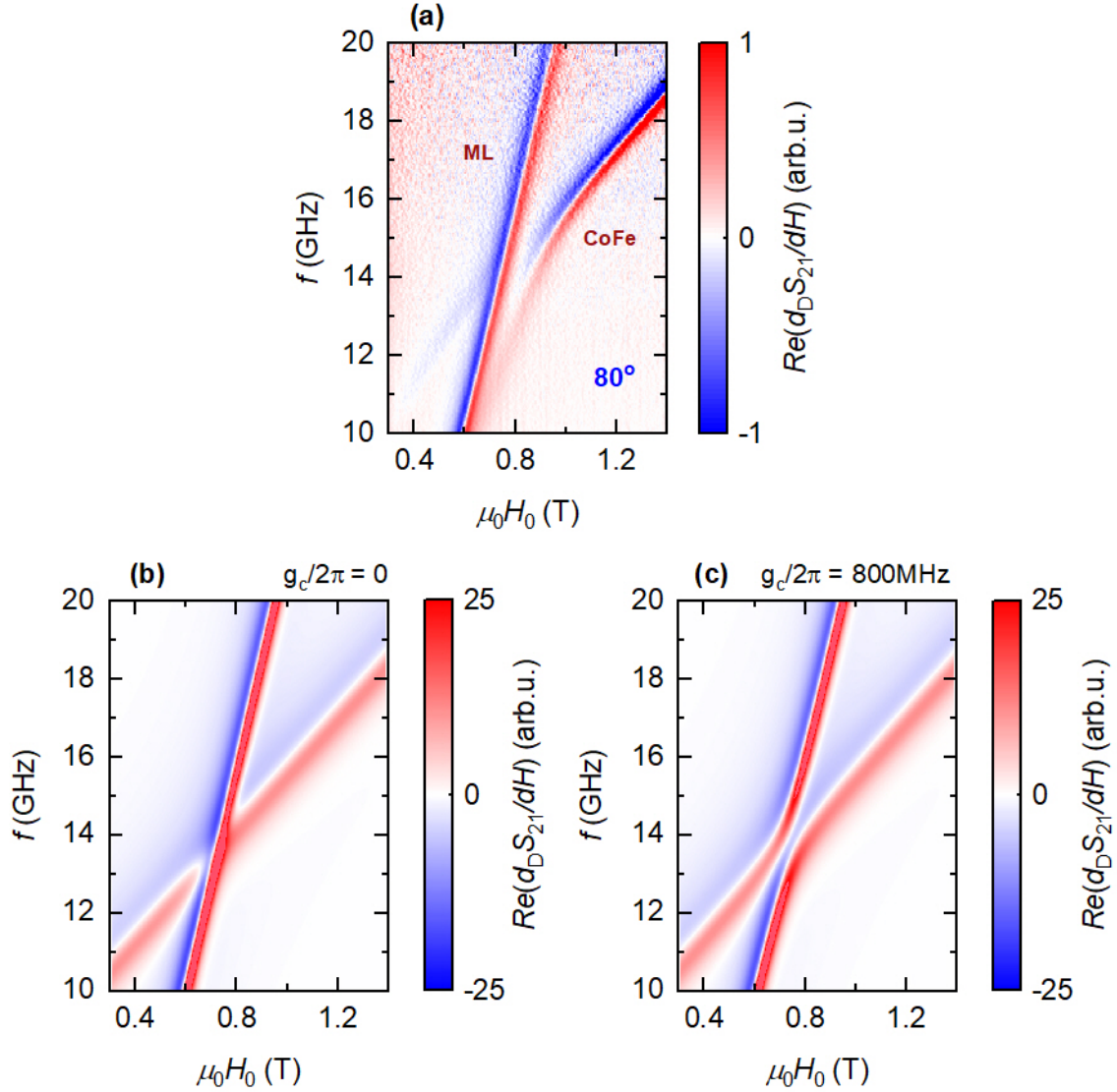
Figure 4.4: (**a**) The FMR measurements of the hybrid system for $\theta = 80°$. The anti-crossing between both FMR signals, the $Co_{25}Fe_{75}$ layer and the multilayer, for frequency about 14 GHz can be seen. The avoided crossing indicates the coupling between the multilayer and the hybrid system. (**b**) (**c**) The plots represents the results of our simulation, with and without coupling. The background correction has been made with the derivative divide (d_D) method. (**b**) Simulation result with $g_c/2\pi = 0$, which represents no coupling between the multilayer and $Co_{25}Fe_{75}$ with no avoided crossing. (**c**) The simulation shows coupling between both systems with $g_c/2\pi = 800$ MHz $> \kappa_m/2\pi$, $\kappa_c/2\pi = 700$ MHz and an avoided crossing similar to our experimental data.

Fig. 4.4. Fig. 4.4 (a) shows the FMR measurements for $\theta = 80°$ while in (b) and (c), we have shown our simulation results. In order to make it clear, the avoided crossing between both oscillators is not just an artifact due to the background correction, we also have performed the background correction to our simulation data using derivative divide (d_D) method. The coupling strength g_c between the multilayer and the $Co_{25}Fe_{75}$ is given in the form of the rate at which the two systems exchange excitation. The loss rate of the multilayer, κ_m and the loss rate of the $Co_{25}Fe_{75}$, κ_c, are decisive parameters of the coupled system. Therefore, together with g_c, we also refer to these as coupling parameters. In this context, one speaks of strong coupling when g_c exceeds both loss rates, κ_m and κ_c.

In our simulation model, we assume that the external loss rate κ_e is constant for all frequencies in the given frequency range. Furthermore, the loss rates for both oscillators are taken as $\kappa_m/2\pi = \kappa_c/2\pi = 700$ MHz which haven been estimated from our experimental data. Now, if we vary the values of coupling strength from $0 \leqslant g_c/2\pi \leqslant 800$ MHz then with $g_c/2\pi = 800$ MHz, we can reproduce our measurement data with very good agreement. Fig. 4.4 (b), with $g_c = 0 < \kappa_m/2\pi = \kappa_c/2\pi = 700$ MHz shows no avoided crossing thus, no coupling exists between both systems. The avoided crossing between both oscillators can be seen in Fig. 4.4 (c). In this case, $g_c/2\pi = 800$ MHz $> \kappa_m/2\pi = \kappa_c/2\pi = 700$ MHz which satisfies the condition of coupling between two oscillators. However, our experimental data shown in Fig. 4.4 (a) does not show any bending of the multilayer signals but the signals from the $Co_{25}Fe_{75}$ does. We attribute this to the coupling of $Co_{25}Fe_{75}$ to the uppermost repeat of the trilayer [Pt(0.75)-$Co_{25}Fe_{75}$(1.1)-Ir(0.45)] or to few repeats of the trilayer. Therefore, it is evident from our simulation results that the avoided crossing in our FMR measurements is not just an artifact rather, it shows the coupling between the multilayer and the $Co_{25}Fe_{75}$.

4.3.2 Variation in Spacer Layer Thickness - RKKY Coupling

In our hybrid system, we have used a nonmagnetic material, Ru, as a spacer layer between multilayer and $Co_{25}Fe_{75}$. Ru is used as a spacer layer because it can support strong short-range interlayer coupling. The thickness of the spacer layer plays a vital role in defining the nature of the coupling between both systems. The interaction is oscillatory which results from the Ruderman-Kittel-Kasuya-Yosida (RKKY) interaction, as already discussed in Ch. 3, that can promote ferromagnetic or antiferromagnetic layer alignment, depending on the thickness of the spacer layer. The period of the RKKY coupling and its strength are extremely sensitive to the Fermi surface of the nonmagnetic spacer layer [84]. The periodicity of the coupling is given by the relation [85]

$$\Lambda = \frac{1}{|(1/\lambda_F) - (n/d)|}, \tag{4.2}$$

where λ_F is the Fermi wavelength and d is half the lattice parameter of the nonmagnetic spacer material i.e., $a = 2d$. Here, the n is a positive integer which satisfies the condition $\Lambda \geq 2d$.

In order to optimize our hybrid system for the strongest signal for the region $\mu_0 H_0 < 400$ mT, as can be seen in the FMR plots in Fig. 4.3, a series of samples was prepared where
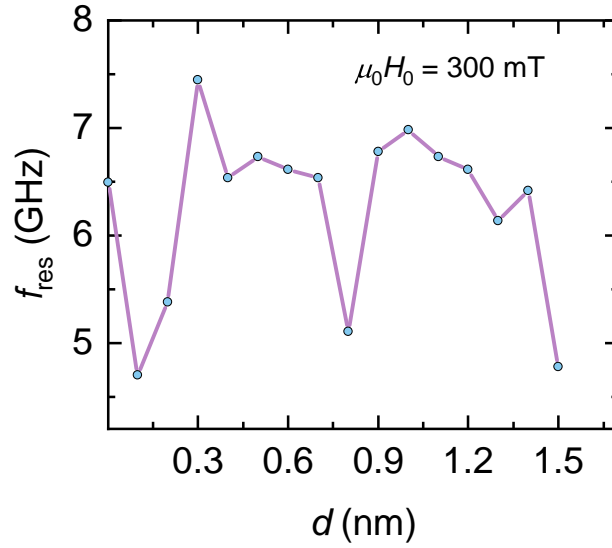
Figure 4.5: Oscillatory behavior of the RKKY interlayer coupling between multilayer and $Co_{25}Fe_{75}$. The period of the RKKY coupling and its strength are extremely sensitive to the Fermi surface of the nonmagnetic spacer layer. The oscillatory interaction promotes ferromagnetic or antiferromagnetic layer alignment, depending on the thickness of the spacer layer. The oscillation period Λ is ≈ 0.7 nm.

the thickness of the nonmagnetic spacer layer (Ru) was varied for 0 nm $\leqslant d \leqslant$ 1.5 nm in steps of 0.1 nm. We observed the strongest signal for $\mu_0 H_0 < 400$ mT when the thickness of spacer is chosen to be 0.9 nm. In addition, for a fixed value of external magnetic field, $\mu_0 H_0 = 300$ mT, we recorded the resonance frequencies for the whole series from our FMR measurements data. The resonance frequency f_{res} vs. thickness (d) plot has been shown in Fig. 4.5. In this plot, we observe the oscillatory behavior of the resonance frequency (f_{res}) with respect to the thickness (d) of the spacer layer. The oscillation period Λ of our hybrid system is found to be ≈ 0.7 nm which is in agreement with Ref. [86]. However, the oscillation period can vary depending on the interfacial roughness as the interfacial roughness can introduce an asymmetry and causes the broadening of the interlayer coupling peak [84].

4.3.3 Measurements with Thicker Spacer and $Co_{25}Fe_{75}$ Layer

Up to this point, we have investigated the sample, Ta(1.5)-Pt(4)-Cu(2)-[Pt(0.75)-$Co_{25}Fe_{75}$(1.1)-Ir(0.45)]$_7$-Ru(0.9)-$Co_{25}Fe_{75}$(5)-Ru(2) which contains a thinner spacer layer of 0.9 nm. In our thesis another type of sample was fabricated with a thicker spacer and $Co_{25}Fe_{75}$ layer which was mainly prepared for a different measurement technique which we will discuss in the next section in detail.

The sample which we now have to investigate is Ta(1.5)-Pt(4)-Cu(2)-[Pt(0.75)-$Co_{25}Fe_{75}$(1.0)-Ir(0.45)]$_7$-Ru(5)-$Co_{25}Fe_{75}$(20)-Ru(2)-Ta(2). As we can see that in this sample, a thick (5 nm) spacer layer of Ru is used, therefore the both systems, multilayer and the $Co_{25}Fe_{75}$ are no longer coupled via short-range RKKY coupling. Rather the coupling is due to the

long-range dipolar interaction or stray-field effect between the both systems. The dipolar interaction, can play an essential role in thin films for stabilization of the long-range magnetic order. The magnetic properties of thin films can be determined by the long-range character of the dipolar interaction which additionally exhibit anisotropy. Moreover, in thin films with ordered state, the symmetry between the out-of-plane orientation and the in-plane orientation is broken due to the dipolar coupling.
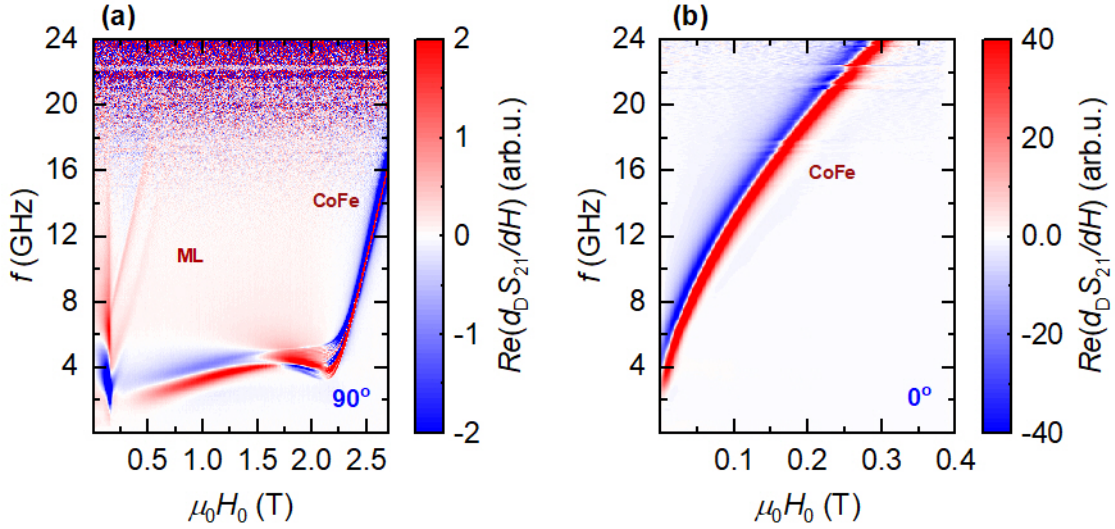
Figure 4.6: (**a**)(**b**) Background corrected FMR plots of the sample, Ta(1.5)-Pt(4)-Cu(2)-[Pt(0.75)-$Co_{25}Fe_{75}$(1.0)-Ir(0.45)]$_7$-Ru(5)-$Co_{25}Fe_{75}$(20)-Ru(2)-Ta(2). (**a**) Plot for OOP configuration. FMR signals from multilayer for $\mu_0 H_0 < 1$ T and from $Co_{25}Fe_{75}$ for $\mu_0 H_0 > 2$ T are shown. (**b**) FMR signals of the same sample in IP configuration, where a very intense signal of $Co_{25}Fe_{75}$ is visible but the signals from the multilayer can not be seen in this configuration.

The background-corrected, using derivative devide d_D method, FMR plots for a hybrid system with composition Ta(1.5)-Pt(4)-Cu(2)-[Pt(0.75)-$Co_{25}Fe_{75}$(1.0)-Ir(0.45)]$_7$-Ru(5)-$Co_{25}Fe_{75}$(20)-Ru(2)-Ta(2) are shown in Fig. 4.6 as a function of external magnetic field H_0 and frequency f.

Fig. 4.6 (a) shows the FMR measurements for the OOP configuration only. In this plot, we can see the signals from both systems i.e., from multilayer and from $Co_{25}Fe_{75}$ as we have seen before for a similar sample with thinner spacer and $Co_{25}Fe_{75}$ layers. If we compare this measurement with the other sample from Fig. 4.3 (a), we can observe that the signals where skyrmions are expected to be present have moved to lower external magnetic field range i.e., $\mu_0 H_0 < 200$ mT. The relocation of these signals is due to the reduction in the thickness of the $Co_{25}Fe_{75}$ in the trilayer, [Pt(0.75)-$Co_{25}Fe_{75}$(1.0)$-$Ir(0.45)]. On the other hand, there are very intense signals from the $Co_{25}Fe_{75}$ layer which can be seen for $\mu_0 H_0 > 2$ T. The Gilbert damping parameter and the effective magnetization for both systems,

multilayer and $Co_{25}Fe_{75}$, for this specific sample are found to be $\alpha_m = 0.122 \pm 0.027$, $\mu_0 M_{\text{eff-m}} = -0.081 \pm 0.011$ T and $\alpha_c = 3.32 \times 10^{-3} \pm 8.86 \times 10^{-4}$, $\mu_0 M_{\text{eff-c}} = 2.12 \pm 0.001$ T respectively. Here the value of effective magnetization for the multilayer system $\mu_0 M_{\text{eff-m}}$ is negative, therefore our multilayer system with trilayer $[Pt(0.75)\text{-}Co_{25}Fe_{75}(1.0)-Ir(0.45)]_7$ is an easy axis system which lies in the easy-axis region of the phase diagram shown in Fig. 3.9.

Now we look onto Fig. 4.6 (b), which display the FMR plot of the same sample but for the IP configuration. Here, just like our previous sample with thinner spacer and $Co_{25}Fe_{75}$ layers shown in Fig. 4.3 (c), one can observe that it displays the signals from the $Co_{25}Fe_{75}$ layer only but now the signals are more intense because of the thicker 20 nm layer of $Co_{25}Fe_{75}$. The measured value of the Gilbert damping parameter and effective magnetization for IP configuration are given as $\alpha_c = 0.028 \pm 1.77 \times 10^{-4}$ and $\mu_0 M_{\text{eff-c}} = 1.48 \pm 0.022$ T.

4.4 FR-MOKE Spinwave Propagation Dynamics

For further investigation of our hybrid system, we used optical spectroscopy and adopted a relatively new technique which is called microfocused frequency-resolved magneto-optic Kerr effect (µFR-MOKE) as already discussed in Sec. 2.7.3. For this optical spectroscopy we designed a device with an on-chip antenna for the excitation of the spinwaves. The fabrication of the whole device is done using the lithography method discussed in Sec. 2.6 and the structuring of the different parts of the sample is done one after the other. First we structure the magnonic waveguide and then the contacts pads, markers (stabilizes the optical drift of the sample stage) and the antennas are done using the same procedure.

For our sample, the magnonic waveguide having dimensions, width $(w) = 2$ µm and length $(l) = 30$ µm is written using the NanoBeam nB5 setup. The multilayer, Ta(1.5)-Pt(4)-Cu(2)-$[Pt(0.75)\text{-}Co_{25}Fe_{75}(1.0)\text{-}Ir(0.45)]_7$-Ru(5)-$Co_{25}Fe_{75}(20)$-Ru(2)-Ta(2) is then deposited via dc sputtering technique following the development procedure. A lift-off in acetone is done afterwards and the whole procedure is repeated step by step for the microwave antenna, contact pads and markers. For the contact pads and antennas we dc sputtered Al(75) and Ta(2) afterwards. After the fabrication of the whole device, the bonding of the antenna and the coplanar waveguide is done via bond wires which are then connected to port 1 of the VNA or the output port of a microwave source by end-launch connectors.

The layout of the fabricated device and the antenna design are shown in Fig. 4.7, which are taken with the KEYENCE digital microscope available at WMI. In Fig. 4.7 (a), the AC1 and AC2 are the center conductors of the two antennas, while DC1 and DC2 are the contact pads for the multilayer/hybrid magnonic waveguide. Fig. 4.7 (b) is the enlarged view of the antenna and the magnonic waveguide. For FR-MOKE measurements only one antenna is needed but we fabricated two antennas over the hybrid system to also perform electrically detected spin wave spectroscopy.

CPW-like antennas having one center strip with two ground lines shorted at the end of the antenna have been designed. The width of the center conductor is 1.4 µm, the width of each ground line is 0.6 µm and the gap between the ground lines and the center conductor is 0.5 µm. The widths of the center conductor and ground lines determine the
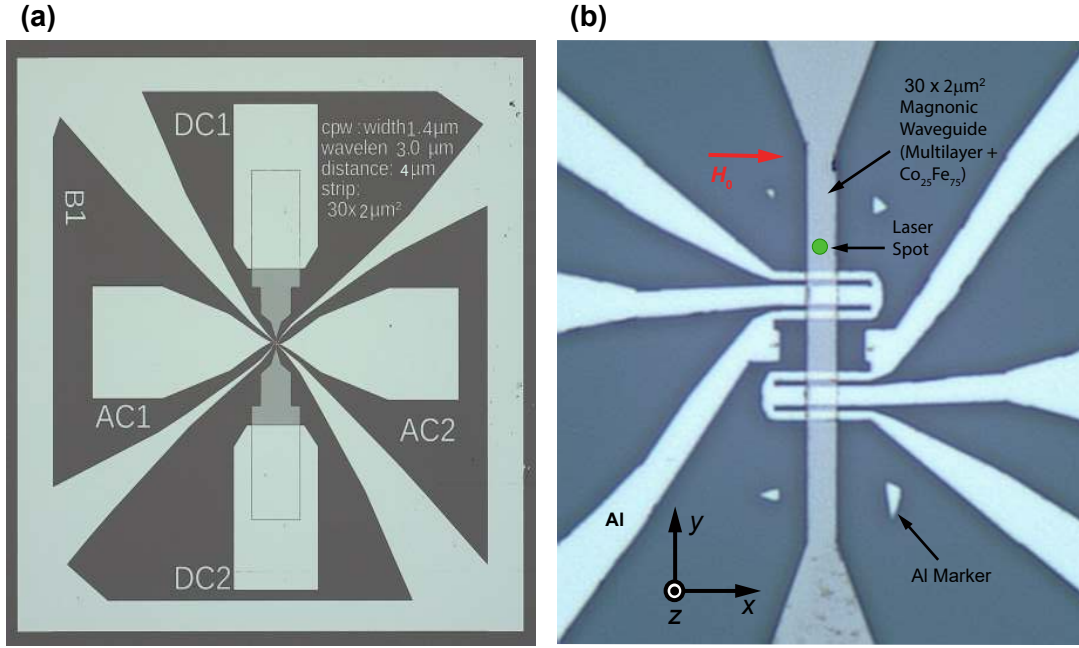
Figure 4.7: (**a**) Camera image of the investigated hybrid device, taken by digital microscope. The AC1 and AC2 are the centre conductors of the two antennas whereas, DC1 and DC2 are the contact pads for the hybrid magnonic waveguide. (**b**) Enlarged view of the magnonic waveguide and the antennas from the same device. Al markers are used for the stabilization of the optical drift of the sample stage. The static magnetic field H_0 is applied perpendicular to the magnonic waveguide.

current densities in respective region. From the given current distribution, we can calculate the excitation efficiency of the antenna for the spinwaves, using Fourier transformation [87]. Our antennas are designed to give maximum efficiency at $|k|_{\max} = 1.57$ µm^{-1}. The non-propagating spinwaves with $k = 0$ can also be excited with roughly 20% less efficiency compared to the most efficiently excited magnons. For this thesis, we used the µFR-MOKE spectroscopy technique to investigate the magnetization dynamics of our hybrid system in the linear regime only, which demonstrates the spinwave propagation.

4.4.1 Spinwave Dynamics in the Linear Regime

In this section, the spinwave propagation characteristics will be explored and for this purpose, we will investigate the magnetization dynamics of spinwaves in the linear regime for IP configuration only. In our experiment, the cw laser power before the microsope objective is set to $P_l = 1.84$ mW and the microwave power of the microwave source or the VNA is set to $P_{MW} = 3$ dBm. The spot size for the cw laser is in the diffraction limit for optimal spatial resolution. µFR-MOKE measurements are sensitive to spurious signals which might stem from free space electromagnetic radiation of the sample, microwave signals in free space or the mobile network. In order to reduce the amplification of such

spurious signals by the amplifier, the low-noise amplifier and the detector are placed into an aluminum box with a copper mesh cladded on the walls along with the lid of the box.

4.4.2 Spatial Propagation Characteristics of Spinwaves

For this experiment, we performed a spatial 2D scan to resolve the wavefronts of the spinwaves in the magnonic waveguide. The laser spot has been scanned in the xy-plane with a step size of 50 nm along both directions. The y-axis is chosen as the "fast scan" axis for this experiment. The magnetic field is fixed to $\mu_0 H_0 = 65$ mT in IP geometry whereas, the microwave frequency is set to a fixed value of $f_{MW} = 11$ GHz. Fig. 4.8 displays the measured exemplary colormaps of the spatial-dependence of the complex S_{21} parameter. Fig. 4.8 (a) shows U_{dc} of the fast photodetector, which is proportional to the reflectivity of the sample. Due to difference in reflectivity, one can easily distinguish between the magnonic waveguide and the substrate where the SiOx-substrate has much smaller reflectivity. From this reflectivity data, the optical width of the magnonic waveguide can be determined which has been indicated with grey dashed lines in Fig. 4.8 (b) and (c), which represent the real and imaginary parts of the S_{21} parameter. The arrow in these plots represents the flow of microwave current I_{MW} through the antenna which has been used for the excitation of the spinwaves and from now on, the arrow will represent the same in all plots.
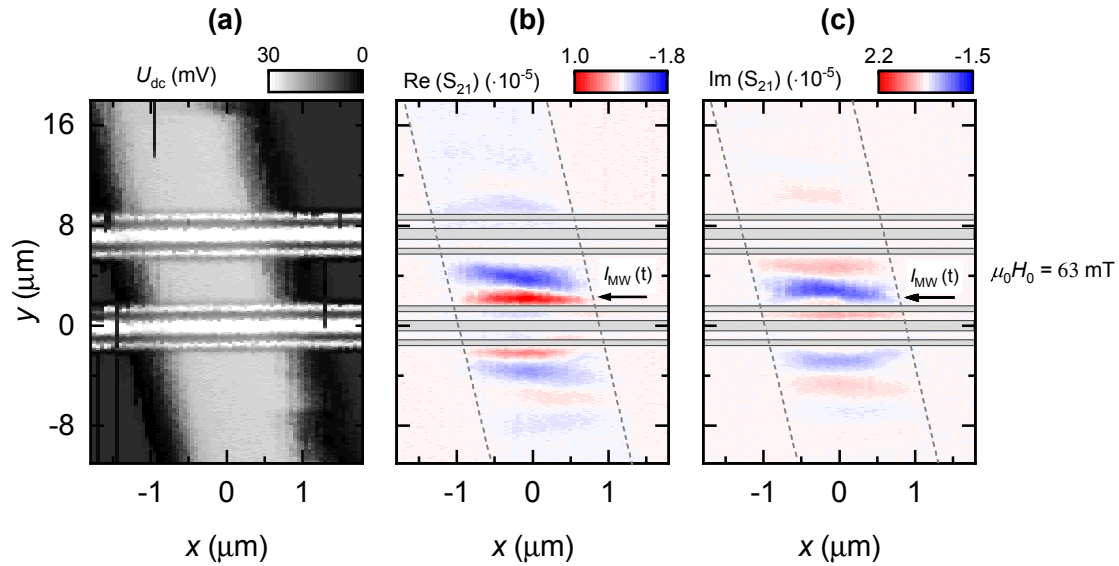
Figure 4.8: The spatial map produced by scanning the laser spot across the magnonic waveguide. Taken at a fixed microwave frequency $f_{MW} = 11$ GHz and fixed magnetic field $\mu_0 H_0 = 65$ mT. (**a**) A measure of the reflectivity at the laser spot position gives the dc-voltage of the photodiode U_{dc}. (**b**) and (**c**) show the real and imaginary parts of the complex S_{21} parameter. The grey dashed lines represent the optical width of the magnonic waveguide which is extracted from the reflectivity measurements shown in (**a**).

We assume that the signal coming from the substrate or next to the magnonic waveguide is from some spurious effects which caused a small deviations in the laser ligth intensity. The wavevector k and propagation length ξ_{sw} can be analyzed if the signal is averaged

over the width of the magnonic waveguide which is shown by the grey dashed lines in Fig. 4.8 (a) and (b) along the x-axis. Moreover, in this set of measurements, the spinwaves are in the Damon-Eshbach regime ($M \perp k$) where the magnetic field H_0 is large enough to overcome the demagnetization field H_d.

Simply measuring the spinwave propagation length ξ_sw and the wavevector k by scanning the laser spot through the center of the magnonic waveguide can lead to misleading results. This is because the spinwaves in patterned waveguides have a multimode character because the k_x component in the stripe waveguide can only take discrete values and results in formation of resonant standing waves perpendicular to the direction of the waveguide axis [88, 89]. The wavevector k_x can take values $k_x^n = n\pi/w$ with n $\in \mathbb{N}$ in the limit $t_\mathrm{w} \ll w$, where t_w is the thickness of the magnonic waveguide [89, 90]. On the other hand, in an extended film, both components k_x and k_y of the wavevector can change continuously. We also want to emphasize that a full 2D map can give different results compared to a single linescan along the magnonic waveguide when extracting the propagation length ξ_sw of the spinwaves.

4.4.3 Mapping the Dispersion Relation of Spinwaves

In this section, we will investigate the spinwave propagation characteristics. For this experiment, sets of measurements are recorded for a series of the magnetic field H_0 ranges from 10 mT to 220 mT with the step size of 15 mT. For each value of the magnetic field H_0 we swept the frequency in the range $f_\mathrm{MW} = 2\ \mathrm{GHz} - 18\ \mathrm{GHz}$ with a step size of 250 MHz. After the stabilization of the magnetic field for each fixed value, the laser spot was scanned through the center of the magnonic waveguide with a step size of 173 nm for each frequency and the complex S_{21} parameter was measured. The measured spectra are shown in Fig. 4.9 for two different magnetic fields.

The left most plot of Fig. 4.9 (a) and (b) gives the information obout the reflectivity, taken from the dc voltage U_dc of the fast photodetector. The plot in the middle of Fig. 4.9 (a) and (b) depicts the real part of the ΔS_{21} parameter, which is measured with VNA. There is always a change in the transmission through the microwave cables because of the change in the microwave frequency f_MW. Furthermore, the optical path and the electrical length of the cables causes variations in the phase. The large microwave background always superimposed the signals which originates from the magnetization dynamics of the system. In order to see the signals only from the magnetization dynamics of the system and exclude the background, we take into account the fact that, when scanning the laser spot, there is no spatial dependence of the microwave background. Thus, we calculate

$$\Delta S_{21}(f,y) = S_{21}(f,y) - S_{21}(f,y_0)|_{y_0=\mathrm{fixed}}, \tag{4.3}$$

where $\Delta S_{21}(f,y)$ is the corrected S_{21} parameter without background signals. For this correction, we subtract a frequency trace of S_{21} parameter, usually at a spot location y_0 where we do not expect any signal from the sample, from each frequency trace of S_{21} parameter at every laser spot position y. In our calculations, we chose the spot location as
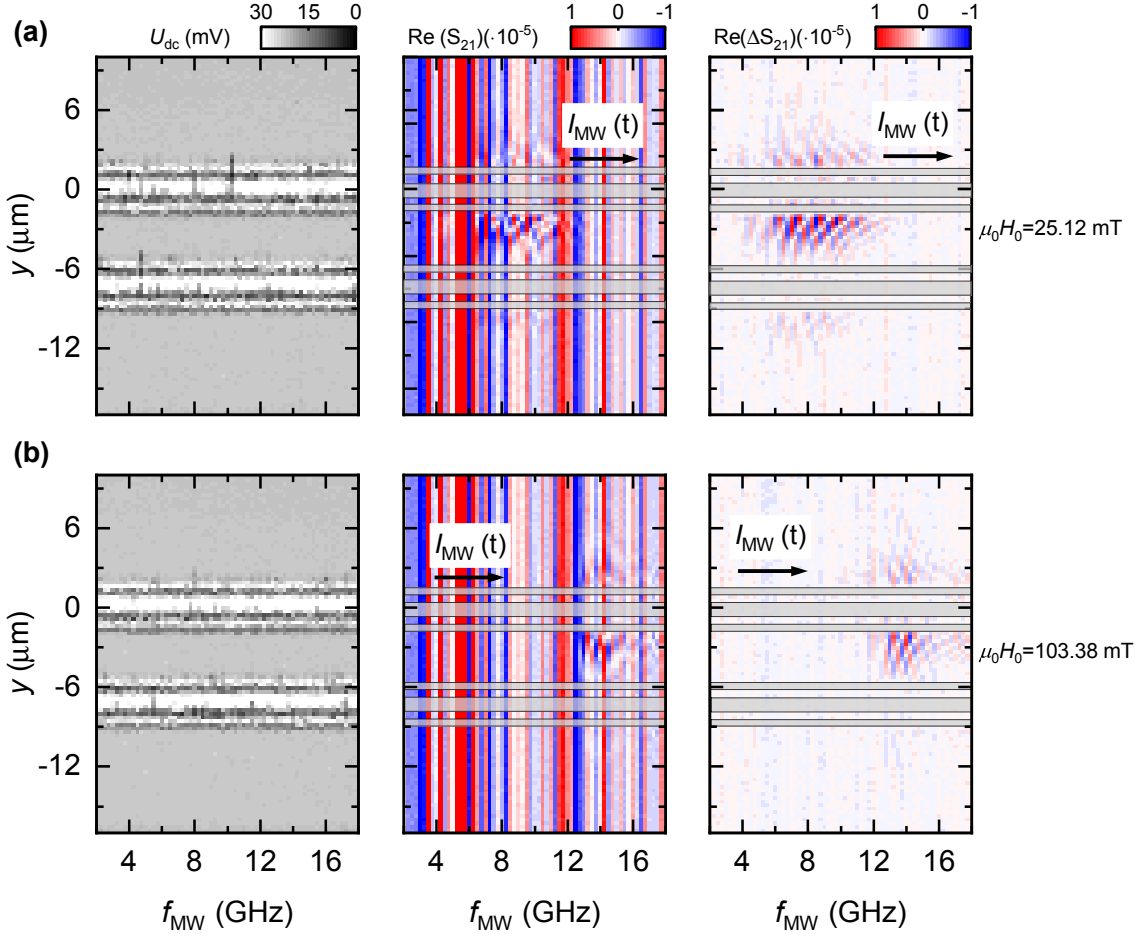
Figure 4.9: Line scan along the center of the magnonic waveguide with a microwave frequency
range $f_{MW} = 2$ GHz-18 GHz at fixed magnetic fields (**a**) $\mu_0 H_0 = 25.12$ mT, (**b**) $\mu_0 H_0$
$= 103.38$ mT. The left most column illustrates the dc-voltage U_{dc} of the photodetector,
which in fact is a measure of the reflectivity. The center column represents the measured
real part of the complex S_{21} transmission parameter. The right most column shows the
real part of the microwave-background corrected ΔS_{21}.

$y_0 = 17.65$ µm. The resulting background corrected, spatial and frequency dependence of
the real part ΔS_{21} is illustrated in the right most plot of Fig. 4.9 (a) and (b).

In these plots, we can observe the different amplitudes of the propagating spinwaves
above and below the antenna. This spinwave non-reciprocity of the spinwave amplitude is
ascribed to the antenna non-reciprocity. Usually, the Damon-Eshbach spinwaves demon-
strate this non-reciprocity of the spinwave amplitude. This non-reciprocity originates from
the relative orientation of the spinwave wavevector and the external magnetic field which
results in different coupling efficiencies of the microwave field of the antenna to the dynamic
magnetization of the spinwave [91, 92].
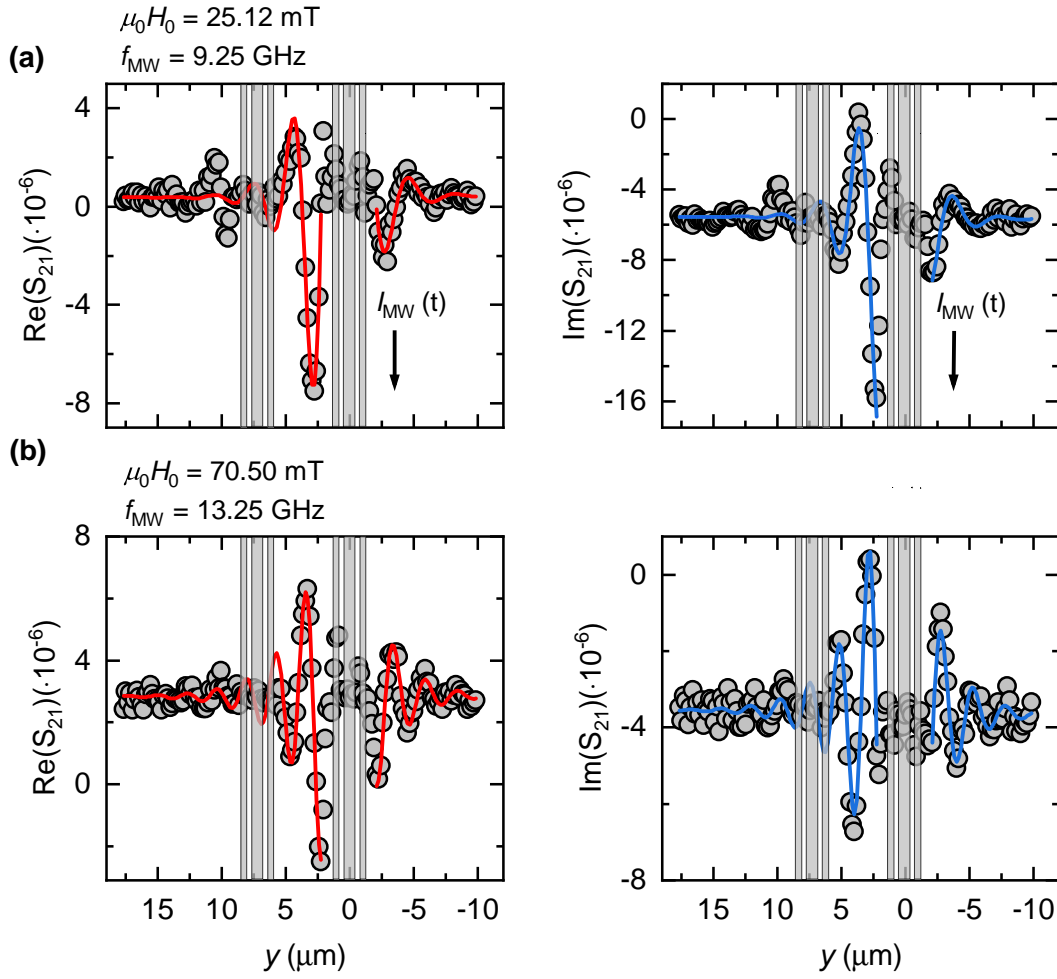
Figure 4.10: Exemplary spatial y-dependence of the measurement data shown in Fig. 4.9. Plotted for fixed magnetic fields $\mu_0 H_0 = 25.12$ mT, $\mu_0 H_0 = 70.50$ mT and microwave frequencies $f_{MW} = 9.25$ GHz, $f_{MW} = 13.25$ GHz respectively. The grey points represent the measured data points and the solid red and blue lines represent the fits to the real and imaginary part respectively.

The phase-sensitivity of µFR-MOKE spectroscopy technique allows us to extract the wavevector k and spinwave propagation length ξ_{sw} by fitting the data to [20]

$$S_{21}(y) = A \cdot \exp\left(-\frac{y}{\xi_{sw}}\right) \cdot e^{iky+\phi} + C_0, \tag{4.4}$$

where A is an amplitude parameter, ϕ is a phase factor and C_0 is a complex offset.

Using Eq. (4.4), we simultaneously fit the real and imaginary part of the S_{21} parameter but it is fitted separately for either side of the antenna. We fit our data for two different microwave frequencies f_{MW} and magnetic fields $\mu_0 H_0$. Exemplary spectra at $\mu_0 H_0 = 25.12$ mT with $f_{MW} = 9.25$ GHz and $\mu_0 H_0 = 70.50$ mT with $f_{MW} = 13.25$ GHz are shown in Fig. 4.10. In Fig. 4.10 (a) and (b), the measured data is represented with grey points, taken from Fig. 4.9. It shows an oscillating behavior which corresponds to the wavefronts of the

spinwave. Due to the finite damping in the system, the spinwaves decay exponentially. From these fits, we can now extract the magnon dispersion.
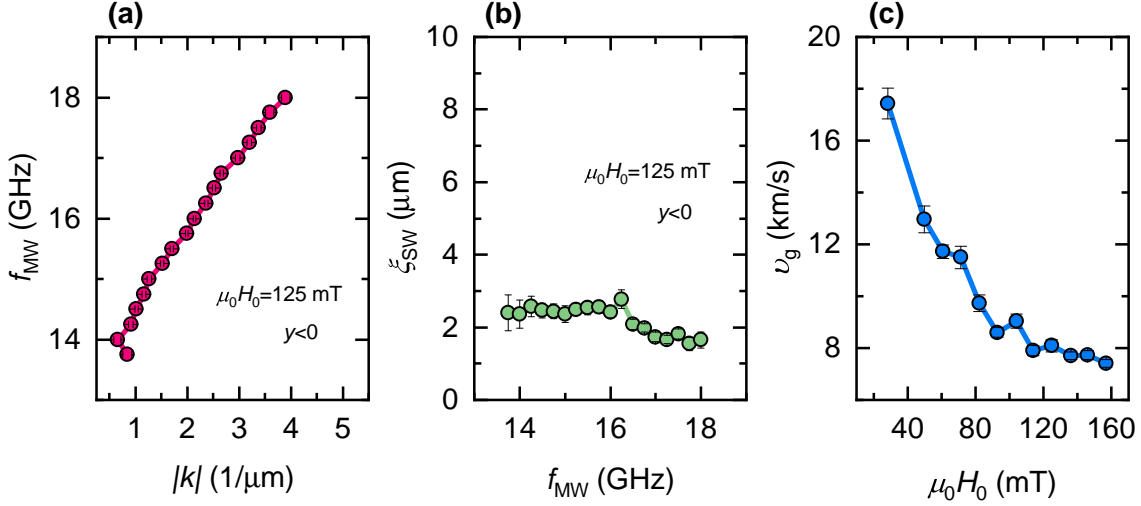
Figure 4.11: (**a**) (**b**) The extracted wave vector k of the spinwave and the spinwave propagation length ξ_{sw} as a function of microwave frequency f_{MW} for magnetic field $\mu_0 H_0 = 125$ mT. The error bars for the wavevector k are smaller than symbol size. (**c**) spinwave group velocity v_{g} as a function of magnetic field $\mu_0 H_0$. For smaller fields, it is increasing and for larger fields it stays constant.

After fitting our data to Eq. (4.4) for different fixed values of magnetic field, we extracted the wavevector k and the propagation length ξ_{sw} of the spinwaves. As we would not expect different results from both sides of the antenna, therefore, here we consider the spinwaves from one side (above antenna) only. The dispersion relation of the spinwaves and corresponding propagation length ξ_{sw} for magnetic field $\mu_0 H_0 = 125$ mT are shown in Fig. 4.11. In Fig. 4.11 (a) we see that the spinwaves show a positive dispersion ($\partial k / \partial f > 0$) which indicates that the spinwaves are in the Damon-Eshbach regime [93]. In general, for the Damon-Eshbach modes ($\phi = \pi/2$ or $M \perp k$), we expect a larger propagation length ξ_{sw} due to their larger group velocity. The propagation length ξ_{sw} in our hybrid system extracted in Fig. 4.11 (b) is much shorter in comparison to those reported in Ref. [94] (up to 20 µm). This might stem from enhanced two magnon scattering due to the multilayer interface, apparently even in the absence of magnetic texture. On the other hand, the group velocities v_{g} for different magnetic field $\mu_0 H_0$, which are shown in Fig. 4.11 (c) demonstrate the maximum group velocity v_{g} at low fields which decreases continuously with the applied field and it is in agreement with literature [93]. The trend of group velocity v_{g} with respect to magnetic field of our hybrid system is in good agreement with the work in Ref. [94], therefore, it reveals that the spinwave dispersion of our system does not show clear indication of magnon-skyrmion interaction in the IP geometry. In this geometry, this is not surprising, as OOP fields are required for the formation of magnetic skyrmions in the multilayers. However, the FR-MOKE technique currently only allows us to apply IP fields.

4.5 Summary

In this chapter, we investigated the ferromagnetic multilayer habrid system in detail. As previously established for the multilayer system, we first fabricated our ferromagnetic hybrid system samples with ultra-high-vacuum (UHV) sputter deposition having sample composition Ta(1.5)-Pt(4)-Cu(2)-[Pt(0.75)-$Co_{25}Fe_{75}$(1.1)-Ir(0.45)]$_7$-Ru(0.9)-$Co_{25}Fe_{75}$(5)-Ru(2)-Ta(2). In order to fully understand the magnetic properties of the hybrid system, first we investigated it with the VNA-FMR technique where, we studied the dynamic properties of the hybrid system in IP and OOP geometry. From our FMR measurements we observed that, with the addition of the $Co_{25}Fe_{75}$ layer on the multilayer stack, the signals below 400 mT are enhanced which might be an indication of strong nucleation of the skyrmions but this needs further confirmation. Furthermore, we have done FMR measurements with angle sweep of the external static magnetic field with respect to the sample orientation and observed the coupling of both systems, i.e., multilayer and $Co_{25}Fe_{75}$ layer. The anti-crossing between signals from multilayer and $Co_{25}Fe_{75}$ layer in FMR measurements is a clear indication of coupling between both systems. We also presented a simulation model which confirms coupling between both systems. The hybrid system has also been investigated with superconducting quantum interference device (SQUID) which gives us insight about the static magnetic properties of the system.

A Ta(1.5)-Pt(4)-Cu(2)-[Pt(0.75)-$Co_{25}Fe_{75}$(1.0)-Ir(0.45)]$_7$-Ru(5)-$Co_{25}Fe_{75}$(20)-Ru(2)-Ta(2) was fabricated, with increased spacer and $Co_{25}Fe_{75}$ layer thickness. This hybrid system is coupled through dipolar interactions. First, the FMR measurements of this system have been done in IP and OOP configuration using a blanket film. Further investigation of the spin dynamics of the same system have been performed via optical spectroscopy technique namely microfocused frequency-resolved magneto-optic Kerr effect (μFR-MOKE). For this optical spectroscopy, we first fabricated a device using electron beam lithography technique. This device has an on-chip antenna for the excitation of the spinwaves in the ferromagnetic multilayer hybrid system. After fabrication of the device, a detailed investigation of the magnetization dynamics of the excited spinwaves in the linear regime for IP configuration of the external magnetic field has been done. In this optical spectroscopy technique, we explored the spatial characteristics of the spinwaves. As evident from the dispersion relation of the spinwaves, our system features spinwaves propagating in Damon-Eshbach regime over a range of external magnetic fields. The spinwaves are found to have large group velocities v_g but rather short spinwave propagation length ξ_{sw}. By analyzing the spinwave dispersion we came to the conclusion that, in the IP configuration, there is no discernible magnon-skyrmion interaction. This is in agreement with expectations, because the multilayer is not expected to form a magnetic skyrmion phase in the IP configuration.

Chapter 5

Summary and Outlook

Summary

In this thesis, magnetic properties including magnetization dynamics of thin film magnetic multilayers and thin film magnetic multilayer hybrid systems hosting skyrmions at room temperature have been investigated. Our easy-plane multilayer system hosts magnetic skyrmions over a broad range of external magnetic fields and thus provides a promising material basis for future skyrmion spintronic devices. In order to investigate the magnetic properties and magnetization dynamics of our thin film ferromagnetic multilayer and ferromagnetic multilayer hybrid system, different measurements approaches have been utilized. To understand the magnetization dynamics of both systems, a vector network analyzer ferromagnetic resonance (VNA-FMR) setup using a coplanar waveguide (CPW) has been used. Apart from VNA-FMR, a novel optical spectroscopy technique called microfocused frequency-resolved magneto-optic Kerr effect (µFR-MOKE) has been used which enabled us to detect and investigate the magnetization dynamics of our ferromagnetic multilayer hybrid system in a spatially-resolved manner. For further understanding of both systems, we also performed superconducting quantum interference device (SQUID) magnetometry. The major finding of our thesis are:

Magnetic Thin Film Multilayer System with Chiral Spin Texture/Skyrmions   In chapter 3 the detailed investigation of metallic thin film multilayer heterostructures has been done. Using VNA-FMR measurements, we investigated the magnetization dynamics of the multilayer and correlated our findings to the magnetic texture revealed by magnetic force microscopy (MFM) to confirm that our multilayer systems host magnetic skyrmions. From our FMR measurements, we deduce magnetic properties like Gilbert damping α, Landé-factor g, and effective magnetization M_{eff}. Our multilayer system is found to have comparably low damping and positive M_{eff}. From the positive value of M_{eff}, it is evident that our system is an easy-plane multilayer system. The IP and OOP hysteresis curves from SQUID data also confirmed that our multilayer is an easy-plane sytem with ferromagnetic interlayer coupling.

We fabricated a series of multilayers with 2 to 7 repetitions of the trilayer [Pt(0.75)-Co$_{25}$Fe$_{75}$(1.1)-Ir(0.45)] and observed the difference in their behavior using FMR. We found that the perpendicular magnetic anisotropy (PMA) of the multilayer is increased with the repetitions of the trilayer whereas the Gilbert damping parameter α and inhomogeneous line broadening $\mu_0 \Delta H_{\text{inh}}$ are independent of the number of repetitions of the trilayer.

Moreover, the FMR measurements reveal that the dense skyrmion state exist in OOP configuration only. In conclusion, our multilayer system can stabilize skyrmions at room temperature over a wide range of external magnetic fields. Magnetic skyrmions are stabilized by interfacial Dzyaloshinskii–Moriya interaction and the multilayers have comparably low damping. The characteristics of our multilayer system are in agreement with the theoretical prediction by Banerjee *et al.* [56]. The significant reduction of damping in our system can result in faster current-driven skyrmion motion. Therefore, our easy-plane multilayer system could attract great attention for further research.

Multilayer/Ferromagnet Hybrid System and Magnonic Device   In chapter 4, we investigated a ferromagnetic-multilayer hybrid systems with VNA-FMR, SQUID magnetometry and microfocused frequency-resolved magneto-optic Kerr effect (µFR-MOKE). Two different hybrid systems were fabricated with different spacer and $Co_{25}Fe_{75}$ thickness. At first, the hybrid system was investigated with VNA-FMR measurements, where the dynamic properties of the hybrid system in IP and OOP geometry have been evaluated. The FMR measurements suggest that with the addition of the $Co_{25}Fe_{75}$ layer on the multilayer stack, the dynamic response at low magnetic fields where skyrmions are expected to stabilize is enhanced. This implies that the nucleation of skyrmions might be impacted by the presence of the $Co_{25}Fe_{75}$ layer. FMR measurements with the external magnetic field at oblique angles indicates coupling between multilayer and $Co_{25}Fe_{75}$ layer spin dynamics. SQUID magnetometry indicates easy-plane anisotropy of the multilayer-ferromagnet hybrids.

A different sample with thicker spacer and $Co_{25}Fe_{75}$ layer was investigated. The multilayer in this system possesses easy-axis anisotropy and multilayer and $Co_{25}Fe_{75}$ dynamics are coupled through dipolar interactions. The FMR measurements of this system shows enhanced dynamic response at low fields $\mu_0 H_0 < 400$ mT. Additionally, we observed a clear magneto-dynamic response from the $Co_{25}Fe_{75}$ layer. To study the spin dynamics by µFR-MOKE, we fabricated a device using electron beam lithography. The device has an on-chip antenna for the excitation of spinwaves. The magnetization dynamics of the hybrid system in IP configuration have been investigated in the linear regime and the spatial characteristics of the spinwaves have been studied. Our system shows spinwaves propagating in the Damon-Eshbach geometry over a range of external magnetic fields. The spinwaves have large group velocities for low magnetic fields but comparably short spinwave propagation lengths. From the spinwave dispersion of our system there is no clear indication of magnon-skyrmion interaction in the IP configuration. This is in agreement with our expectations, because the multilayer is not expected to form a magnetic skyrmion phase in the IP configuration.

Outlook

In the course of this thesis, we fabricated and optimized magnetic metallic thin films which hosts magnetic skyrmions at room temperature. Having in mind that the stabilization of skyrmions at room temperature is a step towards real world applications, all of analysis of magnetization dynamics of the the multilayer thin films have been performed at room tem-

perature. Skyrmions were identified decades ago [95–98] and observed experimentally almost ten years ago in bulk [99], monolayers [100] and thin films [101]. Thin film heterostructures, hosting magnetic skyrmions at room temperature [54, 102] attract increasing attention over the last years because of their potential use in novel devices for information storage and data processing. Such skyrmion-hosting magnetic thin films can be very promising for designing racetrack memories which ultimately can leads to a low cost, low power and extreme compact storage technology [103].

In chapter 4 we investigated the magnetization dynamics of the magnetic multilayer hybrid system using novel optical spectroscopy technique i.e., microfocused frequency-resolved magneto-optic Kerr effect (µFR-MOKE). We investigated our hybrid system in IP geometry only and from these optical measurements, we did not observe magnon-skyrmion interaction. It is evident from the FMR data presented in section 3.3.2 and 4.3 that the stabilization of skyrmions is more dominant in OOP geometry. Hence, the FR-MOKE spectroscopy should be extended to the OOP configuration to study magnon-skyrmion interaction. The coupling of spin dynamics in the ferromagnet and the multilayer should also be studied in samples with thinner spacer layer. The reduction of spacer thickness can result in increased exchange interaction/coupling between multilayer and $Co_{25}Fe_{75}$ layer. This might promote magnon-skyrmion interactions. Moreover, the same optical measurement technique can be used to investigate the bare multilayer system studied in chapter 3. This would allow us to study the magnetization dynamics of the excited spinwaves in the multilayer system in a spatially resolved manner.

As discussed earlier, in our work we investigated the magnetization dynamics of the thin film multilayers and the multilayer hybrid system at room temperature only. In order to reveal the robustness of our systems, we should study the magnetization dynamics as a function of temperature. The skyrmion-based devices should ideally operate at a wide range of temperatures because the velocity of skyrmions highly depends on the temperature as recently realized by Litzius *et al.* [104].

The theoretical predictions and experimental implementations of a skyrmion racetrack memory has already been realized [11, 103, 105]. For skyrmion-based racetrack type memory devices, the driving, controlling and tracking of the skyrmion motion are the most important tasks. One way to control the dynamics of magnetic skyrmions is the spin transfer torque (STT) [106, 107] but this technique has its limitations. For the movement of skyrmions, low current density is required but with this only low speed motion is achieved. One approach to drive skyrmions with increased speeds is using higher current density but in this case the electric current generates significant heat. In most of the skyrmion-hosting materials, the temperature stability is a sensitive parameter. Secondly, only conductive materials can exhibit spin transfer torque based movement. Another approach which can be applied to control skyrmions is using magnetic field gradients which eliminates the necessity of a driving current [10, 108]. The schematic illustration of the concept is presented in Fig. 5.1. Our multilayer system is particularly appealing for this approach, as it demonstrates the stabilization of skyrmions over a large magnetic field range and the skyrmions can retain a constant size i.e., their radii do not depend on external magnetic field like in other PMA systems [59]. The field gradients method requires lower energy than STT and offers

a fine control of the skyrmion motion [10]. Additionally, this approach is equally applicable to all skyrmion-hosting materials in spite of their conductivity. Therefore, this approach should be further investigated.
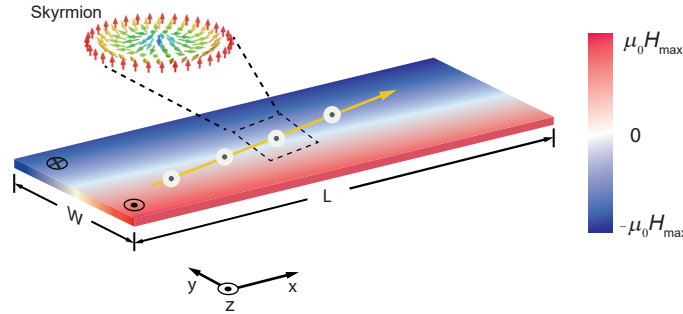
Figure 5.1: Schematic illustration of Néel skyrmion motion along a nanowire thin film. A magnetic field gradient drives the skyrmions. A magnetic field perpendicular to the film plane is applied. The color bar indicates the magnetic field gradient in y-direction.

Furthermore, the exploitation of the temperature gradients might also be favorable for the racetrack-type memory applications [109, 110]. The examination of the effect of temperature on the stabilization and behavior of Néel skyrmions, reported to date in the literature are not very common [19]. Therefore, it might be interesting and potentially constructive to investigate the dependency of temperature and thermal history of our multilayer system on the density and nucleation of skyrmions. Moreover, this approach also presents the possibility to utilize the local heating to enable the nucleation or annihilation of skyrmions which is not just limited to racetrack memories but may also be used in other information technology applications [104]. Novel implementations of skyrmion lattices, in particular those working within a broad range of temperatures, can be realized and possibly provoke future discoveries in caloritronics [111] and spintronics.

Appendix A

Sample Fabrication for the Multilayer System

A.1 Sample Composition and Sputtering Parameters for the Multilayer System

This section contains the used sputter parameters for the fabrication of the thin film multilayer samples, $\text{Ta}(1.5) - \text{Pt}(4) - \text{Cu}(2) - [\text{Pt}(0.75) - \text{Co}_{25}\text{Fe}_{75}(1.1) - \text{Ir}(0.45)]_{\text{N}} - \text{Ru}(1.5)$, as discussed in chapter 3.

Table A.1: N is the number of repetitions of the trilayer $[\text{Pt}(0.75)\text{-}\text{Co}_{25}\text{Fe}_{75}(1.1)\text{-}\text{Ir}(0.45)]$. All samples were grown at $\text{P} = 5 \times 10^{-3}$ mbar, SR4 = 30 rotations/min, MT4 = 70 mm and Argon gas flow= 10 Sccm.

N	Position of magnetrons	Rates $(\text{Å}/s)$
2	Pt, Cu, CoFe, Ru, Ir: Tilted in; Ta: Tilted out	$\text{Ta} = 0.57, \text{Pt} = 0.725,$ $\text{Cu} = 1.12, \text{CoFe} = 1.02,$ $\text{Ir} = 0.43, \text{Ru} = 0.51$
3	————— ” —————	$\text{Ta} = 0.55, \text{Pt} = 0.73,$ $\text{Cu} = 1.07, \text{CoFe} = 1,$ $\text{Ir} = 0.42, \text{Ru} = 0.51$
4	————— ” —————	————— ” —————
5	————— ” —————	$\text{Ta} = 0.57, \text{Pt} = 0.725,$ $\text{Cu} = 1.12, \text{CoFe} = 1.02,$ $\text{Ir} = 0.43, \text{Ru} = 0.51$
6	————— ” —————	————— ” —————
7	————— ” —————	————— ” —————

Appendix B

Sample Fabrication for the Hybrid System

B.1 Sample Composition and Sputtering Parameters for the Multilayer Hybrid System

This section presents the used sputter parameters for the fabrication of the thin film multilayer hybrid system. The parameters for the samples $Ta(1.5) - Pt(4) - Cu(2) - [Pt(0.75)\text{-}Co_{25}Fe_{75}(1.1)\text{-}Ir(0.45)]_7\text{-}Ru(0.9)\text{-}Co_{25}Fe_{75}(5)\text{-}Ru(2)$, $Ta(1.5) - Pt(4) - Cu(2) - [Pt(0.75)\text{-}Co_{25}Fe_{75}(1.0)\text{-}Ir(0.45)]_7\text{-}Ru(5)\text{-}Co_{25}Fe_{75}(20)\text{-}Ru(2)\text{-}Ta(2)$, and antenna which are discussed in Sec. 4.1 of chapter 4 are given in the tables below.

Table B.1: The parameters for the sample $Ta(1.5) - Pt(4) - Cu(2) - [Pt(0.75)\text{-}Co_{25}Fe_{75}(1.1)\text{-}Ir(0.45)]_7\text{-}Ru(0.9)\text{-}Co_{25}Fe_{75}(5)\text{-}Ru(2)$. The sample was grown at $P = 5 \times 10^{-3}$ mbar, $SR4 = 30$ rotations/min, $MT4 = 70$ mm and Argon gas flow= 10 Sccm.

N	Position of magnetrons	Rates $(\text{Å}/s)$
7	Pt, Cu, CoFe, Ru, Ir: Tilted in; Ta: Tilted out	$Ta = 0.57, Pt = 0.725,$ $Cu = 1.13, CoFe = 1.01,$ $Ir = 0.435, Ru = 0.515$

Table B.2: The parameters for the sample $Ta(1.5) - Pt(4) - Cu(2) - [Pt(0.75)\text{-}Co_{25}Fe_{75}(1.0)\text{-}Ir(0.45)]_7\text{-}Ru(5)\text{-}Co_{25}Fe_{75}(20)\text{-}Ru(2)\text{-}Ta(2)$. The sample was grown at $P = 5 \times 10^{-3}$ mbar, $SR4 = 30$ rotations/min, $MT4 = 70$ mm and Argon gas flow= 10 Sccm.

N	Position of magnetrons	Rates $(\text{Å}/s)$
7	Pt, Cu, CoFe, Ru, Ir: Tilted in; Ta: Tilted out	$Ta = 0.58, Pt = 0.72,$ $Cu = 1.13, CoFe = 1.015,$ $Ir = 0.445, Ru = 0.51$

Table B.3: The parameters for the antenna of the sample $Ta(1.5) - Pt(4) - Cu(2) - [Pt(0.75)\text{-}$ $Co_{25}Fe_{75}(1.0)\text{-}Ir(0.45)]_7\text{-}Ru(5)\text{-}Co_{25}Fe_{75}(20)\text{-}Ru(2)\text{-}Ta(2)$. The thicknesses of Al and Ta are 75 nm and 2 nm respectively. The antenna was grown at $P = 5 \times 10^{-3}$ mbar, SR2 = SR4 = 30 rotations/min, MT2 = MT4 = 70 mm and Argon gas flow = 10 Sccm.

Position of magnetrons	**Rates** $(\text{Å}/s)$
Al and Ta: Tilted out	Ta = 0.58, Al: Auto detected

Bibliography

[1] W. Brinkman, D. Haggan, and W. Troutman, *A history of the invention of the transistor and where it will lead us*, IEEE Journal of Solid-State Circuits **32**, 1858–1865 (1997).

[2] S. Lloyd, *Ultimate physical limits to computation*, Nature **406**, 1047–1054 (2000).

[3] J. R. Powell, *The Quantum Limit to Moore's Law*, Proceedings of the IEEE **96**, 1247–1248 (2008).

[4] J. H. Wesenberg, A. Ardavan, G. A. D. Briggs, J. J. L. Morton, R. J. Schoelkopf, D. I. Schuster, and K. Mølmer, *Quantum Computing with an Electron Spin Ensemble*, Physical Review Letters **103**, 070502 (2009), arXiv:0903.3506 .

[5] B. Lenk, H. Ulrichs, F. Garbs, and M. Münzenberg, *The building blocks of magnonics*, Physics Reports **507**, 107–136 (2011), arXiv:1101.0479 .

[6] T. Schwarze, J. Waizner, M. Garst, A. Bauer, I. Stasinopoulos, H. Berger, C. Pfleiderer, and D. Grundler, *Universal helimagnon and skyrmion excitations in metallic, semiconducting and insulating chiral magnets*, Nature Materials **14**, 478–483 (2015).

[7] X. Zhang, M. Ezawa, and Y. Zhou, *Magnetic skyrmion logic gates: conversion, duplication and merging of skyrmions*, Scientific Reports **5**, 9400 (2015), arXiv:1410.3086 .

[8] A. Khitun, M. Bao, and K. L. Wang, *Magnonic logic circuits*, Journal of Physics D: Applied Physics **43**, 264005 (2010).

[9] S. S. P. Parkin, M. Hayashi, and L. Thomas, *Magnetic Domain-Wall Racetrack Memory*, Science **320**, 190–194 (2008), arXiv:1011.1669 .

[10] S. L. Zhang, W. W. Wang, D. M. Burn, H. Peng, H. Berger, A. Bauer, C. Pfleiderer, G. van der Laan, and T. Hesjedal, *Manipulation of skyrmion motion by magnetic field gradients*, Nature Communications **9**, 2115 (2018).

[11] S. Woo, K. Litzius, B. Krüger, M.-Y. Im, L. Caretta, K. Richter, M. Mann, A. Krone, R. M. Reeve, M. Weigand, P. Agrawal, I. Lemesh, M.-A. Mawass, P. Fischer, M. Kläui, and G. S. D. Beach, *Observation of room-temperature magnetic skyrmions and their current-driven dynamics in ultrathin metallic ferromagnets*, Nature Materials **15**, 501–506 (2016).

[12] G. FINOCCHIO, F. BÜTTNER, R. TOMASELLO, M. CARPENTIERI, AND M. KLÄUI, *Magnetic skyrmions: from fundamental to applications*, Journal of Physics D: Applied Physics **49**, 423001 (2016).

[13] A. FERT, V. CROS, AND J. SAMPAIO, *Skyrmions on the track*, Nature Nanotechnology **8**, 152–156 (2013).

[14] A. FERT, N. REYREN, AND V. CROS, *Magnetic skyrmions: advances in physics and potential applications*, Nature Reviews Materials **2**, 17031 (2017).

[15] N. MATHUR, M. J. STOLT, AND S. JIN, *Magnetic skyrmions in nanostructures of non-centrosymmetric materials*, APL Materials **7**, 120703 (2019).

[16] A. SOUMYANARAYANAN, M. RAJU, A. L. GONZALEZ OYARCE, A. K. C. TAN, M.-Y. IM, A. P. PETROVIĆ, P. HO, K. H. KHOO, M. TRAN, C. K. GAN, F. ERNULT, AND C. PANAGOPOULOS, *Tunable room-temperature magnetic skyrmions in Ir/Fe/Co/Pt multilayers*, Nature Materials **16**, 898–904 (2017), arXiv:1606.06034 .

[17] G. YU, P. UPADHYAYA, X. LI, W. LI, S. K. KIM, Y. FAN, K. L. WONG, Y. TSERKOVNYAK, P. K. AMIRI, AND K. L. WANG, *Room-Temperature Creation and Spin–Orbit Torque Manipulation of Skyrmions in Thin Films with Engineered Asymmetry*, Nano Letters **16**, 1981–1988 (2016).

[18] M. HE, G. LI, Z. ZHU, Y. ZHANG, L. PENG, R. LI, J. LI, H. WEI, T. ZHAO, X.-G. ZHANG, S. WANG, S.-Z. LIN, L. GU, G. YU, J. W. CAI, AND B.-G. SHEN, *Evolution of topological skyrmions across the spin reorientation transition in Pt/Co/Ta multilayers*, Physical Review B **97**, 174419 (2018).

[19] S. ZHANG, J. ZHANG, Y. WEN, E. M. CHUDNOVSKY, AND X. ZHANG, *Creation of a thermally assisted skyrmion lattice in Pt/Co/Ta multilayer films*, Applied Physics Letters **113**, 192403 (2018).

[20] L. LIENSBERGER, L. FLACKE, D. ROGERSON, M. ALTHAMMER, R. GROSS, AND M. WEILER, *Spin-Wave Propagation in Metallic CoFe Films Determined by Micro-focused Frequency-Resolved Magneto-Optic Kerr Effect*, IEEE Magnetics Letters **10**, 1–5 (2019).

[21] R. GROSS AND A. MARX, *Festkörperphysik*, 2nd ed. (Walter de GruyterVerlag, 2014) p. 1024.

[22] S. BLUNDELL, *Magnetism in Condensed Matter*, Oxford master series in condensed matter physics (Oxford University Press, 2001) p. 238.

[23] T. MORIYA, *New Mechanism of Anisotropic Superexchange Interaction*, Physical Review Letters **4**, 228–230 (1960).

[24] L. LIENSBERGER, *Spin-Orbit Torques and Magnetization Dynamics in Non-collinear Magnets*, Master Thesis, Technische Universität München , 92 (2017).

[25] J. Johnson, M T, PJH Bloemen, FJAden Broeder, *Magnetic anisotropy in metallic multilayers*, Rep. Prog. Phys. **59**, 1409–1458 (1996).

[26] M. Lakshmanan, *The fascinating world of the Landau–Lifshitz–Gilbert equation: an overview*, Philosophical Transactions of the Royal Society A: Mathematical, Physical and Engineering Sciences **369**, 1280–1300 (2011), arXiv:1101.1005 .

[27] T. Gilbert, *Classics in Magnetics A Phenomenological Theory of Damping in Ferromagnetic Materials*, IEEE Transactions on Magnetics **40**, 3443–3449 (2004).

[28] Carolina Lüthi, *Coupled Magnetization Dynamics in Ferrimagnet/Ferromagnet and Chiral Magnet/Ferromagnet Heterostructures*, Master Thesis, Technische Universität München , 66 (2020).

[29] D. Polder, *VIII. On the theory of ferromagnetic resonance*, The London, Edinburgh, and Dublin Philosophical Magazine and Journal of Science **40**, 99–115 (1949).

[30] C. Kittel, *On the Theory of Ferromagnetic Resonance Absorption*, Physical Review **73**, 155–161 (1948).

[31] J. Bland and B. Heinrich, *Ultrathin magnetic structures III: Fundamentals of nanomagnetism* (Springer, 2005) p. 329.

[32] F. Büttner, C. Moutafis, M. Schneider, B. Krüger, K. B, G. M, G. J, K. S. C, and M. J, *Dynamics and inertia of skyrmionic spin structures*, Nature Physics **11**, 225–228 (2015).

[33] M. Vousden, M. Albert, M. Beg, M.-A. Bisotti, R. Carey, D. Chernyshenko, D. Cortés-Ortuño, W. Wang, O. Hovorka, C. H. Marrows, and H. Fangohr, *Skyrmions in thin films with easy-plane magnetocrystalline anisotropy*, Applied Physics Letters **108**, 132406 (2016), arXiv:1602.02064 .

[34] A. V. Chumak, V. I. Vasyuchka, A. A. Serga, and B. Hillebrands, *Magnon spintronics*, Nature Physics **11**, 453–461 (2015).

[35] A. A. Serga, A. V. Chumak, and B. Hillebrands, *YIG magnonics*, Journal of Physics D: Applied Physics **43**, 264002 (2010).

[36] Lukas Liensberger, *Magnon Hybrid Dynamics*, Ph.D Thesis, Unpublished , Technische Universität München , 168 (2021).

[37] K. Di, V. L. Zhang, H. S. Lim, S. C. Ng, M. H. Kuok, J. Yu, J. Yoon, X. Qiu, and H. Yang, *Direct Observation of the Dzyaloshinskii-Moriya Interaction in a Pt/Co/Ni Film*, Physical Review Letters **114**, 047201 (2015).

[38] A. Mahmoud, F. Ciubotaru, F. Vanderveken, A. V. Chumak, S. Hamdioui, C. Adelmann, and S. Cotofana, *Introduction to spin wave computing*, Journal of Applied Physics **128**, 161101 (2020), arXiv:2006.12905 .

[39] B. A. KALINIKOS, M. P. KOSTYLEV, N. V. KOZHUS, AND A. N. SLAVIN, *The dipole-exchange spin wave spectrum for anisotropic ferromagnetic films with mixed exchange boundary conditions*, Journal of Physics: Condensed Matter **2**, 9861–9877 (1990).

[40] M. A. W. SCHOEN, D. THONIG, M. L. SCHNEIDER, T. J. SILVA, H. T. NEMBACH, O. ERIKSSON, O. KARIS, AND J. M. SHAW, *Ultra-low magnetic damping of a metallic ferromagnet*, Nature Physics **12**, 839–842 (2016).

[41] Y. Y. ZHOU, X. LIU, J. K. FURDYNA, M. A. SCARPULLA, AND O. D. DUBON, *Ferromagnetic resonance investigation of magnetic anisotropy in GaMnAs synthesized by ion implantation and pulsed laser melting*, Physical Review B **80**, 224403 (2009).

[42] S. SIEVERS, J. KURDA, N. LIEBING, F. HOHLS, AND H. W. SCHUMACHER, *Microwave Interferometry for High Sensitivity VNA-FMR Measurements*, IEEE Transactions on Magnetics **53**, 1–4 (2017).

[43] A. ANDERS, *Tutorial: Reactive high power impulse magnetron sputtering (R-HiPIMS)*, Journal of Applied Physics **121**, 171101 (2017).

[44] G. BETZ AND W. HUSINSKY, *Modelling of cluster emission from metal surfaces under ion impact*, Philosophical Transactions of the Royal Society of London. Series A: Mathematical, Physical and Engineering Sciences **362**, 177–194 (2004).

[45] L. FLACKE, *Spin-Pumping and Spin Wave Damping in Co 25 Fe 75 Thin-Film Heterostructures*, Master Thesis, Technische Universität München , 94 (2018).

[46] M. WANG, *Lithography*, edited by M. Wang (IntechOpen, University of Miami, 2010) p. 18.

[47] J. KERR, *XLIII. On rotation of the plane of polarization by reflection from the pole of a magnet*, The London, Edinburgh, and Dublin Philosophical Magazine and Journal of Science **3**, 321–343 (1877).

[48] S. SUGANO AND K. NORIMICHI, *Magneto-Optics*, edited by S. Sugano and N. Kojima, Springer Series in Solid-State Sciences, Vol. 128 (Springer Berlin Heidelberg, 2000) p. 347.

[49] S. YAMAMOTO AND I. MATSUDA, *Measurement of the Resonant Magneto-Optical Kerr Effect Using a Free Electron Laser*, Applied Sciences **7**, 662 (2017).

[50] J. HAMRLE, J. PIŠTORA, B. HILLEBRANDS, B. LENK, AND M. MÜNZENBERG, *Analytical expression of the magneto-optical Kerr effect and Brillouin light scattering intensity arising from dynamic magnetization*, Journal of Physics D: Applied Physics **43**, 325004 (2010), arXiv:1006.1906 .

[51] M. L. SCHNEIDER, J. M. SHAW, A. B. KOS, T. GERRITS, T. J. SILVA, AND R. D. MCMICHAEL, *Spin dynamics and damping in nanomagnets measured directly by*

frequency-resolved magneto-optic Kerr effect, Journal of Applied Physics **102**, 103909 (2007).

[52] K. Everschor-Sitte, J. Masell, R. M. Reeve, and M. Kläui, *Perspective: Magnetic skyrmions—Overview of recent progress in an active research field*, Journal of Applied Physics **124**, 240901 (2018).

[53] V. Dvořák, *A Thermodynamic Theory of Gadolinium Molybdate*, Physica Status Solidi (b) **46**, 763–772 (1971).

[54] C. Moreau-Luchaire, C. Moutafis, N. Reyren, J. Sampaio, C. A. F. Vaz, N. Van Horne, K. Bouzehouane, K. Garcia, C. Deranlot, P. Warnicke, P. Wohlhüter, J.-M. George, M. Weigand, J. Raabe, V. Cros, and A. Fert, *Additive interfacial chiral interaction in multilayers for stabilization of small individual skyrmions at room temperature*, Nature Nanotechnology **11**, 444–448 (2016).

[55] M. N. Wilson, A. B. Butenko, A. N. Bogdanov, and T. L. Monchesky, *Chiral skyrmions in cubic helimagnet films: The role of uniaxial anisotropy*, Physical Review B **89**, 094411 (2014), arXiv:1311.1191 .

[56] S. Banerjee, J. Rowland, O. Erten, and M. Randeria, *Enhanced Stability of Skyrmions in Two-Dimensional Chiral Magnets with Rashba Spin-Orbit Coupling*, Physical Review X **4**, 031045 (2014), arXiv:1402.7082 .

[57] S.-Z. Lin, A. Saxena, and C. D. Batista, *Skyrmion fractionalization and merons in chiral magnets with easy-plane anisotropy*, Physical Review B **91**, 224407 (2015), arXiv:1406.1422 .

[58] M. Opel, *Kapitel 6, Die Austauschwechselwirkung*, Walther-Meißner-Institut (WMI) , 89–112 (2020).

[59] L. Flacke, V. Ahrens, S. Mendisch, L. Körber, T. Böttcher, E. Meidinger, M. Yaqoob, M. Müller, L. Liensberger, A. Kákay, M. Becherer, P. Pirro, M. Althammer, S. Geprägs, H. Huebl, R. Gross, and M. Weiler, *Robust formation of nanoscale magnetic skyrmions in easy-plane thin film multilayers with low damping*, , 6 (2021), arXiv:2102.11117 .

[60] K. Zeissler, M. Mruczkiewicz, S. Finizio, J. Raabe, P. M. Shepley, A. V. Sadovnikov, S. A. Nikitov, K. Fallon, S. McFadzean, S. McVitie, T. A. Moore, G. Burnell, and C. H. Marrows, *Pinning and hysteresis in the field dependent diameter evolution of skyrmions in Pt/Co/Ir superlattice stacks*, Scientific Reports **7**, 15125 (2017).

[61] W. Legrand, D. Maccariello, F. Ajejas, S. Collin, A. Vecchiola, K. Bouzehouane, N. Reyren, V. Cros, and A. Fert, *Room-temperature stabilization of antiferromagnetic skyrmions in synthetic antiferromagnets*, Nature Materials **19**, 34–42 (2020).

[62] A. Svalov, B. González Asensio, A. Chlenova, P. Savin, A. Larrañaga, J. Gonzalez, and G. Kurlyandskaya, *Study of the effect of the deposition rate and seed layers on structure and magnetic properties of magnetron sputtered FeNi films*, Vacuum **119**, 245–249 (2015).

[63] A. J. Lee, A. S. Ahmed, S. Guo, B. D. Esser, D. W. McComb, and F. Yang, *Epitaxial Co 50 Fe 50 (110)/Pt(111) films on MgAlO(001) and its enhancement of perpendicular magnetic anisotropy*, Journal of Applied Physics **125**, 183903 (2019).

[64] A. Ruiz-Calaforra, T. Brächer, V. Lauer, P. Pirro, B. Heinz, M. Geilen, A. V. Chumak, A. Conca, B. Leven, and B. Hillebrands, *The role of the non-magnetic material in spin pumping and magnetization dynamics in NiFe and CoFeB multilayer systems*, Journal of Applied Physics **117**, 163901 (2015).

[65] K.-W. Nielsen, *Ursache der magnetischen Kopplung in Kobalt-dotiertem ZnO*, Doktorarbeit, Technische Universität München , 174 (2007).

[66] H. Maier-Flaig, S. T. B. Goennenwein, R. Ohshima, M. Shiraishi, R. Gross, H. Huebl, and M. Weiler, *Note: Derivative divide, a method for the analysis of broadband ferromagnetic resonance in the frequency domain*, Review of Scientific Instruments **89**, 076101 (2018), arXiv:1705.05694 .

[67] M. Farle, B. Mirwald-Schulz, A. N. Anisimov, W. Platow, and K. Baber-schke, *Higher-order magnetic anisotropies and the nature of the spin-reorientation transition in face-centered-tetragonal Ni(001)/Cu(001)*, Physical Review B **55**, 3708–3715 (1997).

[68] P. D. Louis, *Broadband-Spectroscopy of Magnetic Materials at Low Temperatures*, Master Thesis, Technische Universität München , 84 (2016).

[69] H. T. Nembach, T. J. Silva, J. M. Shaw, M. L. Schneider, M. J. Carey, S. Maat, and J. R. Childress, *Perpendicular ferromagnetic resonance measurements of damping and Lande g factor in sputtered (CoMn)Ge thin film*, Physical Review B **84**, 054424 (2011).

[70] R. D. McMichael, D. J. Twisselmann, and A. Kunz, *Localized Ferromagnetic Resonance in Inhomogeneous Thin Films*, Physical Review Letters **90**, 227601 (2003).

[71] M. C. Hickey and J. S. Moodera, *Origin of Intrinsic Gilbert Damping*, Physical Review Letters **102**, 137601 (2009), arXiv:0812.3184 .

[72] K. Litzius, I. Lemesh, B. Krüger, P. Bassirian, L. Caretta, K. Richter, F. Büttner, K. Sato, O. A. Tretiakov, J. Förster, R. M. Reeve, M. Weigand, I. Bykova, H. Stoll, G. Schütz, G. S. D. Beach, and M. Kläui, *Skyrmion Hall effect revealed by direct time-resolved X-ray microscopy*, Nature Physics **13**, 170–175 (2017), arXiv:1608.07216 .

[73] P. J. Metaxas, J. P. Jamet, A. Mougin, M. Cormier, J. Ferré, V. Baltz, B. Rodmacq, B. Dieny, and R. L. Stamps, *Creep and Flow Regimes of Magnetic Domain-Wall Motion in Ultrathin Pt/Co/Pt Films with Perpendicular Anisotropy*, Physical Review Letters **99**, 217208 (2007).

[74] J. M. Shaw, H. T. Nembach, and T. J. Silva, *Measurement of orbital asymmetry and strain in CoFe/Ni multilayers and alloys: Origins of perpendicular anisotropy*, Physical Review B **87**, 054416 (2013).

[75] J.-M. Beaujour, D. Ravelosona, I. Tudosa, E. E. Fullerton, and A. D. Kent, *Ferromagnetic resonance linewidth in ultrathin films with perpendicular magnetic anisotropy*, Physical Review B **80**, 180415 (2009), arXiv:0905.4779 .

[76] B. Dieny and M. Chshiev, *Perpendicular magnetic anisotropy at transition metal/oxide interfaces and applications*, Reviews of Modern Physics **89**, 025008 (2017).

[77] A. S. Ahmed, J. Rowland, B. D. Esser, S. R. Dunsiger, D. W. McComb, M. Randeria, and R. K. Kawakami, *Chiral bobbers and skyrmions in epitaxial FeGe/Si(111) films*, Physical Review Materials **2**, 041401 (2018), arXiv:1706.08248 .

[78] S. A. Montoya, S. Couture, J. J. Chess, J. C. T. Lee, N. Kent, D. Henze, S. K. Sinha, M.-Y. Im, S. D. Kevan, P. Fischer, B. J. McMorran, V. Lomakin, S. Roy, and E. E. Fullerton, *Tailoring magnetic energies to form dipole skyrmions and skyrmion lattices*, Physical Review B **95**, 024415 (2017).

[79] S. Bordács, A. Butykai, B. G. Szigeti, J. S. White, R. Cubitt, A. O. Leonov, S. Widmann, D. Ehlers, H.-A. K. von Nidda, V. Tsurkan, A. Loidl, and I. Kézsmárki, *Equilibrium Skyrmion Lattice Ground State in a Polar Easy-plane Magnet*, Scientific Reports **7**, 7584 (2017).

[80] G. Kurizki, P. Bertet, Y. Kubo, K. Mølmer, D. Petrosyan, P. Rabl, and J. Schmiedmayer, *Quantum technologies with hybrid systems*, Proceedings of the National Academy of Sciences **112**, 3866–3873 (2015).

[81] R. Hisatomi, A. Osada, Y. Tabuchi, T. Ishikawa, A. Noguchi, R. Yamazaki, K. Usami, and Y. Nakamura, *Bidirectional conversion between microwave and light via ferromagnetic magnons*, Physical Review B **93**, 174427 (2016), arXiv:1601.03908 .

[82] Plansee, *Plansee.com* (2021).

[83] M. A. Greifenstein, *Elektronenspinresonanz mit supraleitenden Mikrowellenresonatoren bei Millikelvin-Temperaturen*, Diplomarbeit, Technische Universität München , 130 (2012).

[84] P. Bruno and C. Chappert, *Oscillatory coupling between ferromagnetic layers separated by a nonmagnetic metal spacer*, Physical Review Letters **67**, 1602–1605 (1991).

[85] R. Coehoorn, *Period of oscillatory exchange interactions in Co/Cu and Fe/Cu multilayer systems*, Physical Review B **44**, 9331–9337 (1991).

[86] H. J. Waring, N. A. B. Johansson, I. J. Vera-Marun, and T. Thomson, *Zero-field Optic Mode Beyond 20 GHz in a Synthetic Antiferromagnet*, Physical Review Applied **13**, 034035 (2020).

[87] V. Vlaminck and M. Bailleul, *Spin-wave transduction at the submicrometer scale: Experiment and modeling*, Physical Review B **81**, 014425 (2010).

[88] V. E. Demidov, S. O. Demokritov, K. Rott, P. Krzysteczko, and G. Reiss, *Self-focusing of spin waves in Permalloy microstripes*, Applied Physics Letters **91**, 252504 (2007).

[89] V. E. Demidov and S. O. Demokritov, *Magnonic Waveguides Studied by Micro-focus Brillouin Light Scattering*, IEEE Transactions on Magnetics **51**, 1–15 (2015).

[90] K. Y. Guslienko, S. O. Demokritov, B. Hillebrands, and A. N. Slavin, *Effective dipolar boundary conditions for dynamic magnetization in thin magnetic stripes*, Physical Review B **66**, 132402 (2002).

[91] M. Nakayama, K. Yamanoi, S. Kasai, S. Mitani, and T. Manago, *Thickness dependence of spin wave nonreciprocity in permalloy film*, Japanese Journal of Applied Physics **54**, 083002 (2015).

[92] M. Bailleul, D. Olligs, and C. Fermon, *Propagating spin wave spectroscopy in a permalloy film: A quantitative analysis*, Applied Physics Letters **83**, 972–974 (2003).

[93] U. K. Bhaskar, G. Talmelli, F. Ciubotaru, C. Adelmann, and T. Devolder, *Backward volume vs Damon–Eshbach: A traveling spin wave spectroscopy comparison*, Journal of Applied Physics **127**, 033902 (2020).

[94] L. Flacke, L. Liensberger, M. Althammer, H. Huebl, S. Geprägs, K. Schultheiss, A. Buzdakov, T. Hula, H. Schultheiss, E. R. J. Edwards, H. T. Nembach, J. M. Shaw, R. Gross, and M. Weiler, *High spin-wave propagation length consistent with low damping in a metallic ferromagnet*, Applied Physics Letters **115**, 122402 (2019), arXiv:1904.11321 .

[95] V. Pokrovsky, *Properties of ordered, continuously degenerate systems*, Advances in Physics **28**, 595–656 (1979).

[96] A. N. Bogdanov and D. A. Yablonskii, *Thermodynamically stable "vortices" in magnetically ordered crystals. The mixed state of magnets*, Journal of Experimental and Theoretical Physics **68**, 101–103 (1989).

[97] A. Bogdanov and A. Hubert, *Thermodynamically stable magnetic vortex states in magnetic crystals*, Journal of Magnetism and Magnetic Materials **138**, 255–269 (1994).

[98] T. Skyrme, *A unified field theory of mesons and baryons*, Nuclear Physics **31**, 556–569 (1962).

[99] S. Muhlbauer, B. Binz, F. Jonietz, C. Pfleiderer, A. Rosch, A. Neubauer, R. Georgii, and P. Boni, *Skyrmion Lattice in a Chiral Magnet*, Science **323**, 915–919 (2009).

[100] S. Heinze, K. von Bergmann, M. Menzel, J. Brede, A. Kubetzka, R. Wiesendanger, G. Bihlmayer, and S. Blügel, *Spontaneous atomic-scale magnetic skyrmion lattice in two dimensions*, Nature Physics **7**, 713–718 (2011).

[101] X. Z. Yu, Y. Onose, N. Kanazawa, J. H. Park, J. H. Han, Y. Matsui, N. Nagaosa, and Y. Tokura, *Real-space observation of a two-dimensional skyrmion crystal*, Nature **465**, 901–904 (2010).

[102] O. Boulle, J. Vogel, H. Yang, S. Pizzini, D. de Souza Chaves, A. Locatelli, T. O. Menteş, A. Sala, L. D. Buda-Prejbeanu, O. Klein, M. Belmeguenai, Y. Roussigné, A. Stashkevich, S. M. Chérif, L. Aballe, M. Foerster, M. Chshiev, S. Auffret, I. M. Miron, and G. Gaudin, *Room-temperature chiral magnetic skyrmions in ultrathin magnetic nanostructures*, Nature Nanotechnology **11**, 449–454 (2016), arXiv:1601.02278 .

[103] R. Tomasello, E. Martinez, R. Zivieri, L. Torres, M. Carpentieri, and G. Finocchio, *A strategy for the design of skyrmion racetrack memories*, Scientific Reports **4**, 6784 (2015), arXiv:1409.6491 .

[104] K. Litzius, J. Leliaert, P. Bassirian, D. Rodrigues, S. Kromin, I. Lemesh, J. Zazvorka, K.-J. Lee, J. Mulkers, N. Kerber, D. Heinze, N. Keil, R. M. Reeve, M. Weigand, B. Van Waeyenberge, G. Schütz, K. Everschor-Sitte, G. S. D. Beach, and M. Kläui, *The role of temperature and drive current in skyrmion dynamics*, Nature Electronics **3**, 30–36 (2020).

[105] W. Kang, Y. Huang, C. Zheng, W. Lv, N. Lei, Y. Zhang, X. Zhang, Y. Zhou, and W. Zhao, *Voltage Controlled Magnetic Skyrmion Motion for Racetrack Memory*, Scientific Reports **6**, 23164 (2016), arXiv:1507.08001 .

[106] J. Masell, D. R. Rodrigues, B. F. McKeever, and K. Everschor-Sitte, *Spin-transfer torque driven motion, deformation, and instabilities of magnetic skyrmions at high currents*, Physical Review B **101**, 214428 (2020), arXiv:2004.00450 .

[107] S. Komineas and N. Papanicolaou, *Skyrmion dynamics in chiral ferromagnets under spin-transfer torque*, Physical Review B **92**, 174405 (2015), arXiv:1508.04821 .

[108] C. Wang, D. Xiao, X. Chen, Y. Zhou, and Y. Liu, *Manipulating and trapping skyrmions by magnetic field gradients*, New Journal of Physics **19**, 083008 (2017).

[109] Q. Shao, *Skyrmions get pushed beyond the limit*, Nature Electronics **3**, 16–17 (2020).

[110] Z. Wang, M. Guo, H. A. Zhou, L. Zhao, T. Xu, R. Tomasello, H. Bai, Y. Dong, S. G. Je, W. Chao, H. S. Han, S. Lee, K. S. Lee, Y. Yao, W. Han, C. Song, H. Wu, M. Carpentieri, G. Finocchio, M. Y. Im, S. Z. Lin, and W. Jiang, *Thermal generation, manipulation and thermoelectric detection of skyrmions*, Nature Electronics **3**, 672–679 (2020).

[111] G. E. Bauer, E. Saitoh, and B. J. Van Wees, *Spin caloritronics*, Nature Materials **11**, 391–399 (2012), arXiv:1107.4395 .

Acknowledgements

During the last year I have learned abundantly and really enjoyed working at the Walther-Meißner-Institut (WMI). Working on this project and its accomplishment would have never been possible without support, cooperation and knowledge of many people. In particular, I would like to thank:

Prof. Dr. Rudolf Gross for giving me the opportunity to carry out my Master's thesis here at WMI and for the pleasant and fruitful mentor talk.

Prof. Dr. Mathias Weiler for offering me this Master's thesis topic and for being a praiseworthy supervisor. I am grateful for your esteemed guidance and your kind attitude which enabled the beginners like me to get motivated and utilize their potential in a better way. Your extensive knowledge encouraged and enabled me to think outside the box and try new methodologies in experiments and data analysis. You have invested your valuable time in extensive proof-reading of this thesis for which I am highly obliged.

Luis Flake for being an excellent advisor. I am grateful for the detailed introductions to the measurement techniques specially the thin film deposition with the Superbowl facility. I am thankful for the valuable discussions and for answering all my questions with patience in an uncomplicated way. I want to thank you for your time that you invested in my learning and for the pleasant atmosphere I ever felt while working with you.

Lukas Liensberger for being an extraordinary advisor. For introducing me to the optical spectroscopy (FR-MOKE) setup and sharing his experiences as an experimentalist. For patiently helping me with all software and technical aspects of this measurement technique and for answering all the questions with long and effective discussions on physics. I am really obliged for your help and guidance for writing of my thesis which would not have been possible without your endless support. Here, I must admit that I can never payback for the time you have invested in my learning and your support during the whole journey of my thesis as it is priceless.

Dr. Matthias Althammer for his valuable discussions on different measurement-related questions. For always being available for resolving all kinds of problems with the Superbowl.

Manuel Müller for helping me with different measurement techniques from time to time with patience. I am grateful for helping me with the FTF fitting and the related software